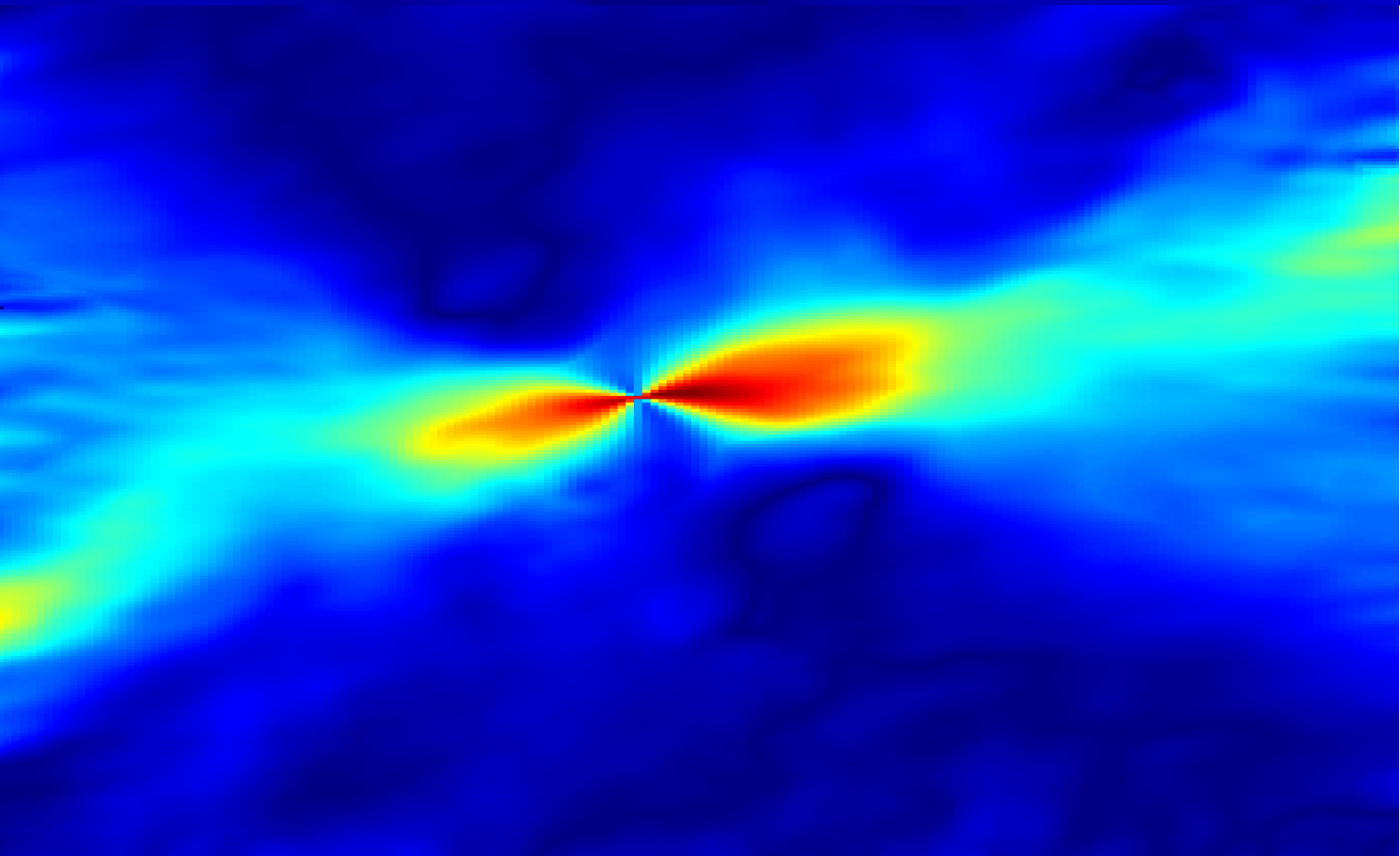


Fingerprinting strain fields to predict tissue rupture

**A conceptual study: DIC in
the diagnosis of
atherosclerosis**

R.M. Hengst



Fingerprinting strain fields to predict tissue rupture

A conceptual study: DIC in the diagnosis of
atherosclerosis

by

R.M. Hengst

to obtain the degree
of Master of Science in Biomedical Engineering
at the Delft University of Technology,
to be defended publicly on Wednesday December 22, 2021 at 15:00.

Student number: 4543572

Thesis committee: Dr. ir. F.J.H. Gijzen, TU Delft and ErasmusMC, chair supervisor
Dr. ir. M. Peirlinck, TU Delft, external supervisor
MSc. ir. H. Crielaard, ErasmusMC, daily supervisor

An electronic version of this thesis is available at
<http://repository.tudelft.nl/>.

Abstract

Atherosclerotic plaque rupture is the underlying cause of 50% of deaths in western society. Although screening methodologies exist, plaques are highly complex, and the parameters used to measure plaque vulnerability are often insufficient for correct medical screening. Since plaque rupture occurs when the vascular forces exceed the plaque strength, the mechanical analysis of plaque stability could offer a new window into predicting rupture. By interpreting the mechanical behaviour of plaques, so-called *mechanical markers* could be derived, which could highlight vulnerable plaques before thrombosis. Unfortunately, the extensively modelled local stresses and energy functions are immeasurable *in vivo*. Therefore we turned to strains, a measure of material deformation that can be obtained clinically. This study investigates the predictive value of strain distributions in the early detection of fibrous caps rupture.

Simplistic plaque cap mimics were engineered to model atherosclerotic plaque rupture. Made from a fibrinous matrix and a soft lipidic inclusion (SI), the constructs were tailored to have mechanical properties similar to *in vivo* plaque caps. Tissue engineered caps offer a wide range of advantages over endarterectomy samples, including unlimited sample availability, robust geometry, high reproducibility and precise control over biological constituents. These constructs were uniaxially strained and subjected to 2D digital image correlation (DIC) to obtain their strain fields. Two-dimensional DIC is an algorithm that derives the material deformation by tracking surface features of its target sample. Therefore, it can very accurately calculate local strains for a material. This report analyses the patterns and maxima of the strain maps of five samples to evaluate unique features distinct at the rupture location that could serve as potential markers of plaque vulnerability. Besides inspecting the individual strain maps, their collective contribution through two strain-based failure criteria was analysed. These failure criteria approximate the strain energy in the samples.

The mechanical failure of the constructs was not instantaneous. All samples underwent failure in phases, starting with a small crack in the SI and concluding with the rupture of the fibrous tissue. Likewise, the strain and failure criteria patterns were consistent within all samples. Even though their strain values differ, the accumulations of low and high strains lie at nearly identical positions. These patterns emerged early in the tensile experiment, as the frames at a physiological (10%) and final (ultimate state before rupture) global strain measured a strong resemblance. In a more localised analysis, the fields were radially divided into 'slices' of data to produce distinct segment-based patterns. The rupture location consistently lies at a unique feature in the pattern, such as a peak or a valley. As was observed before, aside from the difference in their magnitude, the strain patterns showed no change between the frames. Finally, the local maxima of the strain and failure criteria maps were inspected. Their distances to the rupture site were comparable for all maps, indicating they performed similarly at estimating the rupture location. Moreover, the distances measured for the final frame showed no significant difference to those measured for the physiological frame.

The mechanical response of the five samples is similar. Aside from undergoing mechanical rupture in stages, the analysis of the tissue construct shows that a relationship exists between the local strains and rupture location. First, the rupture location always sits at the edge of a high valued region in the SI. Second, the tissue segmentation produces a highly reproducible pattern with a distinct colocalisation between segment patterns and the rupture location. Third, the maxima of the strain and failure criteria maps lie close to the rupture site, although they

do not overlap. Accordingly, there is a clear relationship between the rupture location and the local strain patterns.

Preface

This master thesis is an integral part of my master degree in Biomedical Engineering at the TU Delft. This document summarises my work of the past months at the cardiovascular biomechanics laboratory in the Erasmus Medical Center, under the guidance of my supervisors, Dr. ir. Gijsen and MSc. ir. Crielaard.

I have learned a lot from the past year. With a background in Nanobiology, my understanding of the mechanical engineering field has been limited, to say the least. Yet here I am, completing a thesis based on the mechanical behaviour of biological tissues. Facing this reality makes me realise the incredible development I have made in one year. I must admit that I am a little proud of myself.

*R.M. Hengst
Delft, December 2021*

Contents

Abstract	iii
List of Figures	ix
List of Tables	xii
1 Introduction	1
1.1 Pathophysiology of Atherosclerosis	2
1.2 Project motivation	3
1.3 Thesis aims and outline	5
2 Methods	7
2.1 Tissue engineered constructs	8
2.1.1 Tissue construction	8
2.1.2 Mechanical testing	8
2.1.3 Selection criteria	9
2.2 Image pre-processing	10
2.3 Obtaining strain fields	11
2.3.1 Theory of Digital Image Correlation	11
2.4 Local strain analysis	12
2.4.1 Obtaining tissue coordinates of special features	13
2.4.2 Strain patterns and rupture location	13
2.4.3 Local strain maxima and rupture location	14
2.4.4 Partitioned local strains	14
3 Results	17
3.1 Pattern analysis	17
3.1.1 Displacement fields	17
3.1.2 Strain fields	18
3.1.3 Failure criteria	19
3.2 Rupture mechanics	21
3.2.1 Rupture phases	21
3.2.2 Rupture location	21
3.2.3 Rupture in strain fields	22
3.3 Local analysis	24
3.3.1 Rupture vs. segment patterns	24
3.3.2 Rupture vs. local maxima	26
3.3.3 Physiological frame	27
4 Discussion	31

4.1	Image pre-processing	31
4.2	Pattern analysis	32
4.3	Rupture analysis	34
4.4	Local strain analysis	36
4.4.1	Segmented patterns and rupture	36
4.4.2	Local maxima and rupture	37
4.4.3	Physiological frame	38
4.5	Limitations	39
5	Concluding remarks	41
5.1	Conclusions	41
5.2	Future prospective	42
	Acknowledgements	45
A	Sample database	47
B	Image pre-processing in ImageJ	49
B.1	Summary of the different filters	52
B.1.1	Cropping	52
B.1.2	Improving contrast	52
B.1.3	Greyscale contrast	52
B.1.4	Enhance local contrast function	52
B.1.5	Gaussian filtering (blur)	52
B.1.6	Background subtraction	52
B.1.7	Intensity thresholding	53
B.2	Evaluation of filters	53
C	Selecting tissue features	55
D	Ncorr Algorithm	59
D.1	Working principle	59
D.2	Program execution	61
D.2.1	Uploading relevant files on Ncorr	61
D.2.2	Parameters	62
D.2.3	Obtaining data fields	64
D.3	Optimising DIC	64
E	All strain fields	67
E.1	Cartesian coordinate system	67
E.1.1	Marked local strain fields in final frame	67
E.1.2	Marked local strain fields in the physiological frame	68
E.1.3	Maxima of local strain fields in final frame	70
E.1.4	Maxima of local strain fields in physiological frame	70
E.2	Polar coordinate system	72
E.2.1	Marked local strain fields in the final frame	72
E.2.2	Marked local strain field at a physiological frame	74
E.2.3	Maxima of local strain fields in final frame	76
E.2.4	Maxima of local strain rates in the physiological frame.	78

F	Local strain maxima in the full tissue construct	81
G	Different coordinate systems	85
	G.0.1 Polar coordinates	85
H	Segmentation	87
I	Polar Strains	89
	I.1 Patterns analysis and rupture	89
	I.1.1 Polar strains	89
	I.1.2 Failure criteria	90
	I.2 Local analysis	91
	I.2.1 Segmentation	91
	I.2.2 Local maxima	91
J	Script necessities	93
	J.0.1 Elimination of boundary elements	93
	J.1 Zoomed perspective of the SI	93
	J.2 Structural similarity index	93
	Bibliography	95

List of Figures

1.1	Top 10 causes of death in the world. Data extracted from from WHO website [5]	1
1.2	(a) shows the main vascular layers, the adventitia (A), the media (M) and the intima (I). Atherosclerosis changes their morphology and structure, where the build-up of fatty substances and immune cells in the intima causes it to penetrate into the luminal space. (b) shows a cross-sectional perspective of plaque development in the phases: endothelial injury, intimal thickening, inflammation, fatty streak formation, formation of a fibrous cap, growth to mature atheroma and thrombosis [2, 9].	2
2.1	Summary of the steps described in this chapter.	7
2.2	From left to right, the protocol used to create the tissue engineered caps. <i>Day 0</i> Static culturing of HVSCs in fibrin gel. <i>Day 7</i> Insertion and static culturing of SI. <i>Day 14</i> Dynamic culturing. <i>Day 21</i> Mechanical tests and tissue analysis	8
2.3	Orientation axis of tissues and its relation to the in vivo intima. The circumferential (y) direction lies along the length of the vessel, and is suggested to carry most vascular loads.	9
2.4	Pre-processing of images is defined by the following steps. After manual selection and isolation of the relevant images, they were cropped and processed by a blur. Based on the morphology of the tissue, a region of interest (ROI) is selected, that excludes tissue near the clamps (up and down)	10
2.5	The global stress-strain relation between all preconditioned samples.	11
2.6	Two approaches of calculating strain ($\epsilon = \delta L/L_0$)	11
2.7	The global tissue response obtained during the uniaxial tensile test. The marked frames correspond to the analysed final and physiological frames.	12
2.8	Physiological and ultimate time frames were analysed in a cartesian and polar coordinate system. This analysis includes the inspection of strains and their failure criteria.	13
2.9	The steps taken to identify the relationship between local maxima and rupture in the final and physiological frames. The red dotted boundary indicate the region from where data is included for the evaluation of maxima.	14
2.10	Segmentation of the central tissue area allows up to 16 partitions during segmentation. As is described by appendix H, the segmentation orientation is adaptable.	15
3.1	Displacement fields of the tissue engineered sample	18

3.2	DIC produces ε_{xx} , ε_{xy} and ε_{yy} strains maps of the ROI in the experimental image. The color maps indicate regions of high (dark red) and low (dark blue) local strain. The shear strain is a symmetric entity [52], and is therefore presented in its absolute form. Note that experimental images underwent processing before being fed into Ncorr. The selected strain fields correspond to the final frame before tissue rupture, where the tissue engineered construct experiences a global strain of 0.23 in the y-direction.	19
3.3	Strain-based failure criteria.	20
3.4	Four phases of rupture identified in the tissue engineered samples.	21
3.5	Rupture locations throughout all samples. The white ellipse represents the SI outline, the black box surrounds sites of rupture initiation, and the white boxes distinguish the areas of fibrous tissue rupture.	22
3.6	Marked strain field maps before SI rupture. Rupture of the SI and fibrous tissue initiate at the black and white rectangles respectively. The shape and boundary of the SI is indicated by the white oval at the center of the images.	22
3.7	The local analysis of the cartesian strains and their failure criteria focuses on the SI and its surrounding tissue.	24
3.8	Boxplots of cartesian strains	25
3.9	Boxplots of cartesian failure criteria	26
3.10	Local analysis of cartesian strain maxima	26
3.11	Local analysis of cartesian failure criteria. Note that the magnitudes of both criteria are scaled differently (0 to 1 for the nominal strain, and 0 to 3 for quadratic strain).	27
3.12	Comparison between final and physiological frames.	28
3.13	Distance between maxima of strain and failure criteria maps and the location of SI rupture initiation. Comparison between final and physiological frames.	29
4.1	The predicted behavior of a finite element geometry that resembles the tissue engineered constructs. Note that the SI is modelled as a hole with zero stiffness. Images obtained from the master thesis of Serra (2020) [44].	32
4.2	The predicted behavior of a finite element geometry that resembles the tissue engineered constructs. Images obtain from the master thesis of Serra [44].	34
B.1	The effect of improving the speckle patterns digitally. The image on the left has poor contrast and high noise. Too much noise reduction will produce the second image, where no speckles are anymore visible. This results in the loss of essential data used during tracking. The third image has much better contrast but is tainted by noise which might interfere with speckle identification. Optimization of both noise and contrast results in the right-most image, allowing the reliable DIC.	49
B.3	Metric comparison of all image filters. The legend (on the right) relates each filter to a colour. The sixth filter has eight different versions, where the radius is changed to 0.5, 1, 1.5, 2, 2.5, 3, 3.5 and 4 pixels. The left graph indicates the least square correlation coefficient, while the right graph presents the number of iterations of each filter. To improve image quality, the value of the metric must lie below the baseline, which corresponds to the neutral effect of 'cropping'. The error bars correspond to the data variance.	54
C.1	Identify time of starting frame	56
C.2	Identify time of physiological frame	56

C.4	Select the coordinates and correct their positions by following the speckle patterns.	57
D.1	The Region Of Interest (ROI) is divided into subsets. The relative movements of these subsets are used to obtain the local strains	59
D.2	Setting up a path for the Ncorr GUI	61
D.3	Overview of startup Ncorr GUI	61
D.4	To select the current images, use the Load Lazy approach to call images to the program. This important for large image stacks.	62
D.5	First three steps are completed, and their data is visible in the GUI	62
D.6	The optimal parameters for DIC on the tissue constructs are a subset radius of 35 and a spacing of 3	63
D.7	Selecting seed points. They should be equally spaced, to divide the region up into equal portions. Most importantly, they must not move out of ROI.	63
D.8	Seed preview. Here the user can validate the performance of the program. The seed must not move outside the ROI and must converge, as is indicated by the iterations (max of 50) and correlation coefficient.	63
D.9	The displacements are formatted by scaling the image to 0.0093 mm/pixel with a cutoff of 0.7 for the correlation coefficient.	64
D.10	The Lagrangian strains are calculated with a radius of 5. These points fit the plane in the Least Squares fit.	64
E.1	Exx, Exy and Eyy strains converted into circular polar strains.	73
E.2	Exx, Exy and Eyy strains converted into circular polar strains.	75
E.3	Exx, Exy and Eyy strains converted into circular polar strains.	77
E.4	Exx, Exy and Eyy strains converted into circular polar strains.	79
F.1	Full and zoomed tissue perspectives. The red boundaries highlight from where the local maxima are considered.	81
F.2	Strain field maps before SI rupture, with maximal strain points highlighted by '+' and minimal strain points by 'o'. The black and white rectangles correspond to the SI and fibrous tissue rupture sites, while the white ellipse represents the location and shape of the SI.	82
F.3	Average distance (in mm) between SI rupture box and maxima and minima. The error bars indicate the standard deviation between all samples.	82
I.1	Marked strain field maps before SI rupture. Rupture of the SI and fibrous tissue initiate at the black and white rectangles respectively. The shape and boundary of the SI is indicated by the white oval at the center of the images.	89
I.3	Boxplots based on 16-fold segmentation	91
J.1	Summary of SSIM measurement. Image taken from Wang, et al. [69]	94

List of Tables

3.1	The structural similarity between the final and physiological frame. Note that the SSIM is scaled between 0 and 1.	28
4.1	Relation between strain patterns and rupture	36
4.2	Relationship between boxplot patterns and rupture	37
A.1	Database of all samples	47
E.1	Strain fields before SI rupture.	67
E.1	Strain fields before SI rupture.	68
E.2	Strain fields at physiological frame.	69
E.3	Strain fields before SI rupture.	70
E.4	Strain fields before SI rupture.	71
H.1	The arc lengths corresponding to different amounts of segmentation	87

Introduction

Atherosclerotic patients suffer from a progressive buildup of lipidic substances in the internal layer of the blood vessels, the tunica intima, leading up to luminal occlusion. Smoking, hypertension, hypercholesterolemia and obesity are several aggravators of the disease, increasing its likelihood [1, 2, 3]. The systematic disease typically takes 50 years to express symptoms but can cause an almost instantaneous death [4]. Furthermore, at critical locations, such as the brain or heart, it may cause stroke or ischemic heart disease, which cost around 15 million lives annually [5]. Therefore, it is of clinical importance to better understand this disease and prevent its progression.

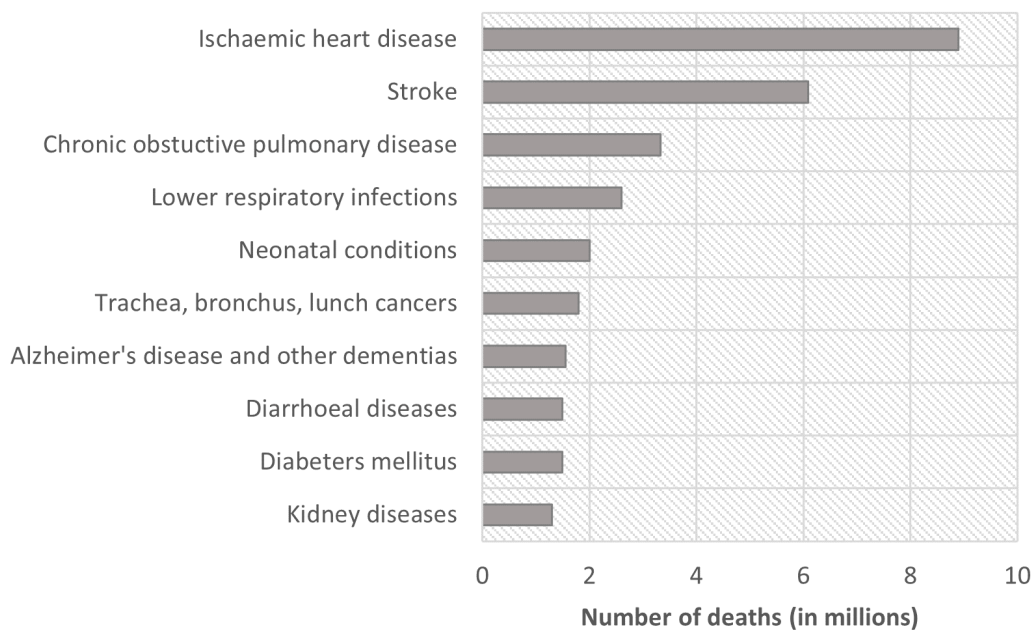


Figure 1.1: Top 10 causes of death in the world. Data extracted from from WHO website [5]

1.1. Pathophysiology of Atherosclerosis

Healthy arteries have three regularly shaped layers, with distinct functionality (see figure 1.2a) [6, 3]. The tunica adventitia is the outermost vessel layer, whose identifying components are collagen fibres. They provide structural support and protection to the blood vessels. Adjacent lies the tunica media, the middle layer, which is rich in neatly ordered sheets of smooth muscle cells and elastin. Its muscular capacity powers vasodilation (increased lumen diameter) and vasoconstriction (decreased lumen diameter). Finally, the tunica intima lies at the innermost surface and is composed of endothelial cells that line the lumen. This innermost layer is in direct contact with the luminal blood. Atherosclerosis changes the arterial physiology, causing intimal thickening and the obstruction of regular blood flow.

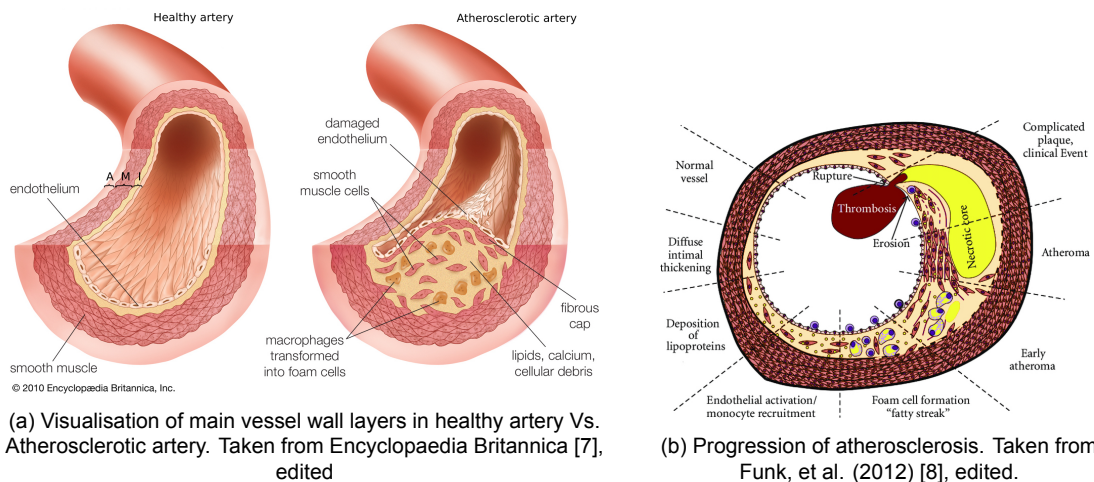


Figure 1.2: **(a)** shows the main vascular layers, the adventitia (A), the media (M) and the intima (I). Atherosclerosis changes their morphology and structure, where the build-up of fatty substances and immune cells in the intima causes it to penetrate into the luminal space. **(b)** shows a cross-sectional perspective of plaque development in the phases: endothelial injury, intimal thickening, inflammation, fatty streak formation, formation of a fibrous cap, growth to mature atheroma and thrombosis [2, 9].

Ignoring the healing mechanisms, the development of atherosclerotic plaques follows a general pattern. This is summarised in figure 1.2b. Endothelial dysfunction is the precursor of the disease, triggered by biomechanical abnormalities, genetic or immunological causes, or low wall shear stress [6]. The consequent buildup of macro-molecules in the subendothelial space causes intimal thickening and inflammatory response. While fatty streaks develop from LDL-saturated macrophages, outward remodelling of the intima preserves the lumen size. Once the plaque grows into an atheroma, this is no longer possible, where the intima progressively enters the lumen. Proliferating smooth muscle cells migrate towards the luminal surface of the plaque to form a fibrous cap. Fibrous caps play an important role in resisting dynamic vascular forces [10, 11]. They are rich in load-bearing collagen fibres, heterogeneously scattered with microcalcifications, macrocalcifications and cells. Fibrous caps form the barrier between luminal blood and the necrotic core. If the cap stresses exceed the ultimate cap strength, the thrombotic material within the growing plaque mass is released into the bloodstream, leading to thrombosis.

1.2. Project motivation

Plaque fragments and pro-thrombotic material are released into the bloodstream during a thrombotic event. Consequent blood coagulation can compromise local and distal blood circulation by inducing complete luminal occlusion at the lesion site or form emboli that travel downstream to block smaller vessels [1, 3, 9]. Cells lying beyond the cloth experience ischemia and may die if the blood supply is not restored. Nearly half of all thrombotic events are associated with rupture of the fibrous cap [12, 13]. Although its mechanism is not completely understood, rupture appears to favour high curvature areas where high circumferential stresses accumulate, like the cap shoulder (the junction between cap and intima). Around 63% of all rupture events occur at cap shoulders, while the remaining events occur at the mid-cap or cap centre [14, 10]. Rupture is initiated when the fibrous cap strength is insufficient against the cap stresses, leading to the formation of a micro-crack [1]. These stresses typically lie between 300 - 545 kPa [14, 15]. The crack propagates through the cap, leading to plaque separation and the release of its pro-thrombotic content.

Timely identification of mechanically weak caps may prevent the cascade of vascular events after rupture. Aside from saving patients' lives, it also lessens the financial and clinical burden on the medical field [16].

The term '*vulnerable*' is allocated to plaques that are prone to rupture and likely to cause acute vascular events. Thin cap fibroatheromas (TCFA) are typically associated with vulnerability. They are eccentric plaques with large necrotic cores, and a high degree of inflammation and calcification [17, 18]. Their cap thickness criteria lie around 65 μm and 200 μm for coronary and carotid plaques, respectively [19, 17]. Vulnerable plaques differ from '*stable*' ones, which can withstand higher stresses and do not require medical intervention. Stable plaques typically have thick caps overlying small lipid pools, making them more resistant to rupture. Current diagnostic approaches employ non-invasive imaging modalities to detect features associated with vulnerability. Hence, it is possible to estimate lipid core sizes, cap thicknesses, inflammation, and the degree of calcification [20, 21, 22]. Unfortunately, it is becoming increasingly evident that these biomarkers are poor and often inaccurate predictors of cap vulnerability [23, 24, 25, 26, 27, 28, 29]. Current biomarkers for vulnerability cannot account for all cap biomechanical behaviour, as TCFA's have been identified in both stable and unstable coronary syndromes. TCFA's were found to account for only two-thirds of acute coronary syndromes in large patient groups [29, 30]. Moreover, the limitations of clinical screening hinder the identification of plaque morphology and constituents *in vivo*.

The need for new markers for plaque vulnerability [31] could be satisfied by taking a biomechanical approach to this problem. Instead of looking for more biological markers, the stability of the plaque can be mechanically estimated. Any unique characteristics identified by such an approach could become mechanical markers.

Several research groups have investigated the relationship between stress and energy field distributions in atherosclerotic caps and the occurrence of a rupture event [32, 33, 34]. Vengrenyuk et al. (2006) presented their computational work on the effect of microcalcifications (particles smaller than 50 μm formed by basic calcium crystals aggregates) on the circumferential stress distribution and location of peak circumferential stresses [35]. The authors found that the rigid nature of these inclusions causes increases in local cap stress. Papers by Maldonado et al. (2012) [32], and Cardoso et al. (2014) [34] agree with these findings and suggest that high stresses may be indicative of rupture sites. Luo et al. (2016) have extended this work, including the consideration of stored energy [36]. The authors found the location of rupture to associate with the highest numerically derived energy through computational modelling. The predictive power of their models appears even greater than a purely stress-based

consideration. Another means of rupture location prediction follows the application of failure criteria to numerical models. Examples include the strain energy criterion [37], continuum damage mechanics [38] and the von mises stress criterion. A critical fracture criterion defines the threshold between intact and fracture-prone tissue sections. Once reached, the tissue should experience mechanical failure. Unfortunately, all the above studies are predominantly based on numerical data and employ computational approaches like finite element analysis to simulate their results. Although the models provide much insight into the arterial mechanics, they lack experimental validation. The use of theoretical material properties indicates that the models remain estimates of *in vivo* environments. Local stresses and material properties are currently immeasurable entities, inhibiting the replication of these models in a clinical setting. Therefore, local stress and energy distributions cannot be employed as biomarkers of plaque rupture yet.

In contrast, local material strain is measurable. *In vivo* strain acquisition is a development that may hold much potential in the field of cardiovascular mechanics. Described in the papers of Schaar et al. (2002) [23] and de Korte et al. (2003) [39], intravascular elastography allows for the acquisition of wall displacement through ultrasound imaging. These can detect intravascular movement at a scale of several hundred micrometres. Non-invasive approaches to identify vascular movement also exist [40, 41], allowing imaging from outside the skin. Local tissue strains are measured by applying digital image correlation (DIC) on video images acquired from moving tissue. DIC is a mathematical algorithm that employs image recognition software to derive the relative local movements of distinct tissue surface features. DIC then translates the local displacement fields into local strain fields. Strains can be linked with the microstructure and stiffness of the plaque, where high positive strains indicate expansion, while negative or low strains may indicate compression or resistance to movement.

The investigation of local strain patterns may be a realizable approach for predicting the biomechanical stability of plaques. Being a measurable entity and applicable for clinical settings, it could serve as a potential tool for classifying patient-specific plaque behaviour. Furthermore, because the approach would be free from models with assumed material properties, it is relatively computationally inexpensive and less likely to be biased by unpredictable variables.

An experimental study to obtain strain patterns would require a simplistic model that can mimic *in vivo* tissue behaviour. The material properties of the model must closely resemble those of human plaque caps and allow for mechanical testing. *Ex vivo* endarterectomy samples are a less favourable model for such an undertaking for several reasons. The most predominant disadvantage of *ex vivo* samples is their uncontrollable nature. Maintaining morphological, biological and genetic uniformity across *ex vivo* tissues is nearly impossible. Both intra-sample micro-composition variation and inter-sample diversity play a significant role in restricting the repeatability of experiments. They may also compromise the reliability of test results because the mechanical effects of these variables are uncertain.

Secondly, endarterectomy specimen have finite sizes, which limit the sample size of testable *ex vivo* caps. Because experiments are unrepeatable and samples show inter-and intra- biological diversity, large-scale studies will suffer from the restricted availability of *ex vivo* caps. A third disadvantage is their susceptibility to damage. The intricate procedures of artery extraction and arterial layer separation can not guarantee the integrity of plaque caps. Samples obtained after careful patient selection can therefore easily be compromised. Finally, the time-consuming classification of their undetermined biological structures poses a fourth disadvantage to using *ex vivo* samples. This step is necessary to unravel the biological complexity found in human samples. Aside from increasing the likelihood of damage, the equipment and computer power needed to unravel the underlying components can significantly extend the

duration of experimentation.

A good candidate for acquiring strain field data is the biomimetic cap tissue, engineered by Wissing et al. (2021) [42]. These are thin fibrous tissues whose tunable nature allows for controlled cap construction with tailored tissue contents and mechanical properties. Examples of such properties are collagen content and orientation. The fibrillar collagenous matrix is the main component and load-bearing element of the engineered construct. Therefore, it serves as the base and structural support of the engineered tissue structures. Variation to its content (e.g. collagen type, fibre distribution, digestive matrix metalloproteinase activity) directly affects cap strength, stiffness, and general mechanical properties. According to Wissing et al. (2021), these constructs show alikeness to *in vivo* plaques, as the mechanical responses of the biomimetic cap lie within the ranges found in *in vivo* human carotid fibrous caps (0.5 - 5 MPa) [42, 43]. Repeated protocols have produced caps with consistent properties, showing their applicability for large scale studies. The constructs also show plasticity to heterogeneity. Wissing et al. (2021) soundly incorporated a soft inclusion into its collagenous matrix that mimics the lipidic core found in plaques. This indicates that the constructs are customizable and could potentially be attributed with different constituents found in *in vivo* plaque caps. This enables systematic investigation of biomechanical cap behaviour without the uncontrolled complexity accompanying uncontrolled plaque heterogeneity. The tissue engineered plaque caps are, therefore, highly suitable for simulating the material behaviour of *in vivo* atherosclerotic caps.

1.3. Thesis aims and outline

This project hypothesizes that strain field fingerprinting may be a potential methodology for assessing plaque vulnerability and identifying rupture locations. To investigate this, this project encompasses the following aims.

1. Identify the strain values and modes at the rupture location, right before rupture occurs and at a global strain of 10%.
2. Find the relationship between rupture location and local strain minima and maxima, right before rupture and at a global strain of 10%.

Before betaking on this journey, this project also identified a basic image pre-processing approach to improve correlation parameters during DIC. The details of this process are described in chapter 2 and appendix B.

The study analyses five tissue constructs undergoing tensile tests and translates their movement into a local strain map using DIC. Consequently, with a multitude of analysis techniques, the author attempts to answer the above aims.

2

Methods

This chapter discusses the methodology of the study, assembling a work pipeline for future research. This is summarised in figure 2.1.

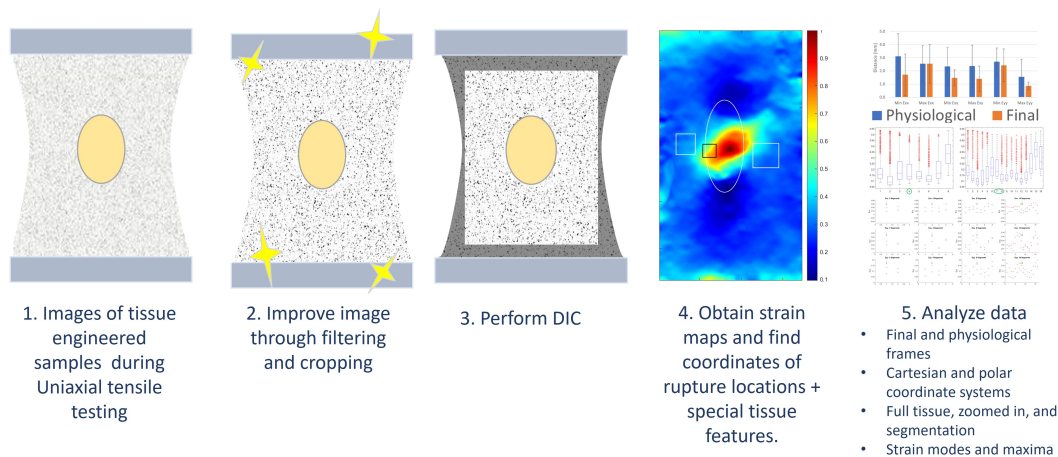


Figure 2.1: Summary of the steps described in this chapter.

The first step in the trajectory of the project comprised the creation and mechanical testing of tissue engineered constructs, following the protocol described by Wissing et al. (2021) and the master thesis of Sheila Serra (2020) [44, 42]. Section 2.1 provides a brief outline of tissue creation and mechanical testing.

The next step encompassed the improvement of image quality for further processing. From a group of different image processing approaches, an optimal and simplistic filter was selected to improve the output of digital image correlation (DIC). This was only applied to images that captured tissue movement from the start of the experiment until rupture. The details of this step are described in section 2.3.

Finally, the DIC output was analyzed to investigate the different relationships between rupture and the local strain fields.

2.1. Tissue engineered constructs

Previous experiments by Serra [44] and Tamar et al., [42] have created tissue engineered samples, whose data was made accessible for this report. An overview of all samples is provided in appendix A. This section summarises the steps taken to create these tissue constructs, the mechanical test they were subjected to, and this study's selection criteria.

2.1.1. Tissue construction

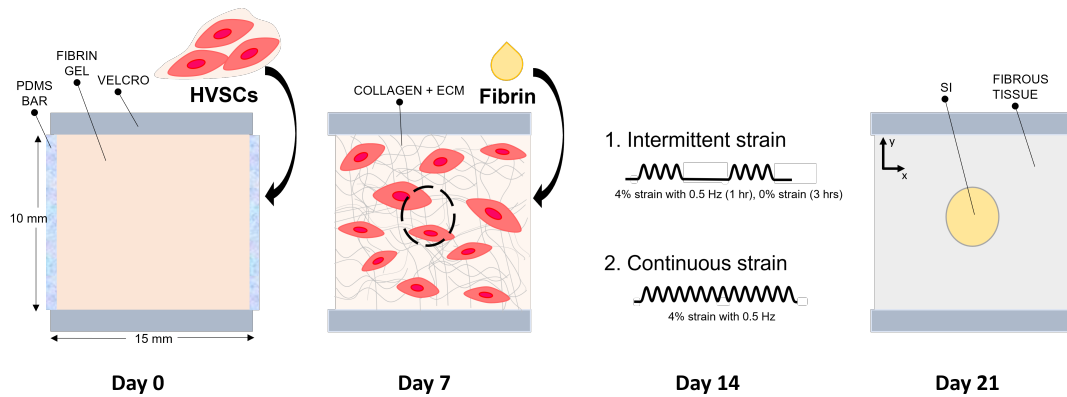


Figure 2.2: From left to right, the protocol used to create the tissue engineered caps. *Day 0* Static culturing of HVSCs in fibrin gel. *Day 7* Insertion and static culturing of SI. *Day 14* Dynamic culturing. *Day 21* Mechanical tests and tissue analysis

The creation of the tissue construct followed a 21-day protocol, starting with the seeding of myofibroblasts (human vena saphena cells, HVSCs) suspension in a fibrin-based gel between two Velcro strips. Over the course of 7 days, the HVSCs produced an extracellular matrix, creating a fibrin-cell matrix. Next, a 2 mm diameter core was punctured at the centre of the matrix and filled with a fibrin suspension. This is termed soft inclusion (SI) and functionally mimics the lipid core found in atherosclerotic plaques. The SI was cultured for another week, allowing it to integrate with the fibrin-cell matrix. Once day 14 arrived, the tissues were grouped in two different dynamic (cyclic) loading protocols. The first group experienced intermittent strain, where the tissue was alternatively strained (4% strain for 1 hour) and allowed to rest (0% strain for 3 hours). This straining protocol stimulates collagen synthesis and remodelling, which leads to fibre anisotropy [45, 42]. The second group experienced continuous 4% strain for the entire seven day period. These constructs were expected to have improved mechanical properties because of the balance between collagen and cross-link production [46, 42]. Both protocols were performed in a Flexcell system (Flexcell Int, McKeesport, Pa) by attaching the velcro strips to its flexible membrane with medical adhesive silicone (Silastic, MDX4-4210, Dow Corning, Midland, MI). The tension was induced by vacuum suction along the vertical (y) direction—dynamic loading results in the alignment of collagen fibres with the loading direction. Once 21 days had passed, SI integration and cell infiltration were assumed to be sufficient. Hence, it was possible to conduct mechanical tests on the biomimetic cap. This whole process is summarised in figure 2.2.

2.1.2. Mechanical testing

After two weeks of static culturing and one week of dynamic loading, the samples were subjected to uniaxial tensile tests in PBS at 37°C. Before mounting the samples to the commercial set up of CellScale Biomaterial Testing, Waterloo, Canada, black graphite speckles were ap-

plied to the tissue surface with a cotton swab. These serve as visual markings for DIC analysis, conducted later in the experiment. Mechanical testing was performed along the vertical direction by applying forces on both clamps, as is depicted in figure 2.3. In this setup, the vertical axis corresponds to the circumferential direction *in vivo* [44, 42, 47, 48]. After clamping the velcros between the clamps of the setup, the samples were preconditioned with ten cycles of 10% strain. Finally, the samples were uniaxially strained until rupture with a strain rate of $100\% \text{ min}^{-1}$. This movement was captured by a 15 Hz camera, whose lens was located directly above the tissue.

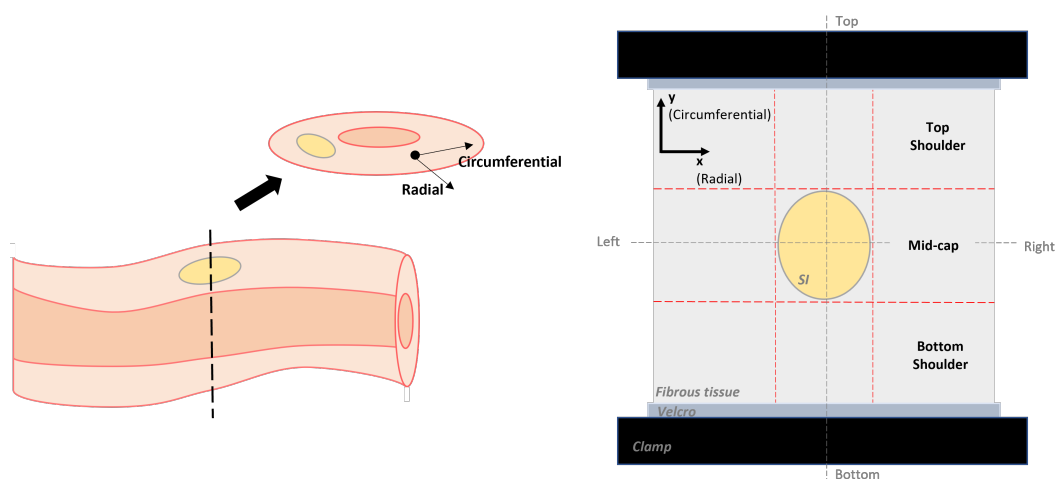


Figure 2.3: Orientation axis of tissues and its relation to the *in vivo* intima. The circumferential (y) direction lies along the length of the vessel, and is suggested to carry most vascular loads.

2.1.3. Selection criteria

Not all samples reported in appendix A were suitable for this report. A set of criteria were necessary to define suitable features for this study. The sample must:

- *Have a SI at the centre of the tissue* to ensure uniformity between tissues. This reflects on the consistency in mechanical responses amongst samples.
- *Have a SI diameter of 2 mm* to ensure that the size of the inclusion is constant throughout the samples.
- *Rupture at the mid-cap of the tissue* so the rupture event occurs within the region of interest for DIC. This criterion helps to exclude tissues that rupture at the clamp interface.
- *Undergo dynamic loading during the final culture week* (i.e. intermittent and continuous loading protocols). Control tissues, which were not loaded during culturing, are excluded as a result of this.
- *Be fixed to the commercial clamp system* to ensure the same setup was employed during mechanical experiments. This excludes samples that used a re-designed clamp system.

This project has identified five samples to fulfil the above requirements. The relevant constructs are highlighted in appendix A. The included samples are products from continuous ($n=3$) and intermittent ($n=2$) loading protocols. The global mechanical properties between these two groups were similar [42]. Inspection of all tissues showed that two of the five samples

were already damaged before the start of the experiment. Fortunately, the small cuts in the SI centre did not negatively affect their mechanical behaviour or DIC performance. However, one of those samples also experienced slippage, which is tissue movement at the uniaxial ledger due to insufficient friction. Tissue slippage resulted in the distortion of its strain map. These consequences are discussed in chapter 4.

2.2. Image pre-processing

The pre-processing of images adhered to the scheme presented in figure 2.4. The first step in this flow chart entails the selection of images that capture the uniaxially strained tissue until rupture. The relevant images were then subjected to the next step: image cropping. Here, the boundary of the cropped region was manually selected for each sample to ensure that the entire tissue was visible throughout each image stack. Next, a Gaussian blur (radius of 2.5) was applied to the cropped images. This low pass filter attenuates high-frequency signals, thereby reducing noise. After going through both steps, the images were fully processed for DIC. The last step in figure 2.4 shows the manual selection of the region of interest (ROI). The ROI is a binary image used by DIC to identify the tissue region for which strain fields are calculated. The ROI does not include tissue near the clamps to evade mechanical artefacts from their interaction. Appendix C proves a detailed overview of the mentioned steps.

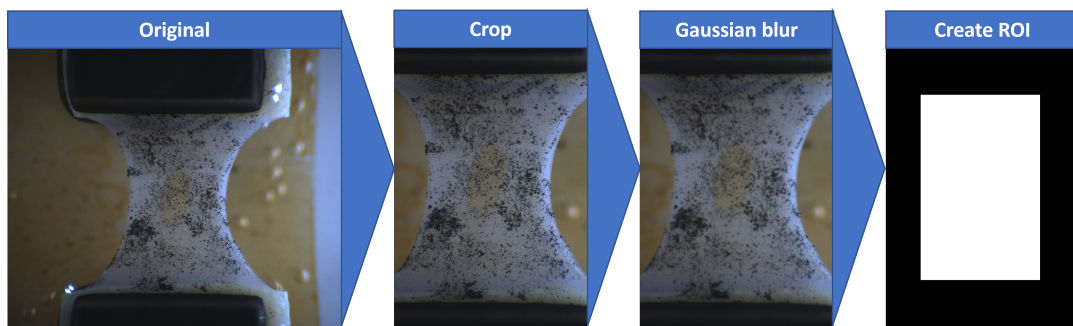


Figure 2.4: Pre-processing of images is defined by the following steps. After manual selection and isolation of the relevant images, they were cropped and processed by a blur. Based on the morphology of the tissue, a region of interest (ROI) is selected, that excludes tissue near the clamps (up and down)

2.3. Obtaining strain fields

Uniaxial tensile tests can disclose global tissue behaviour. This is depicted in figure 2.5, which relates the global strains to global stresses of all samples. The inclining lines rise at different rates and belong to different samples. The abrupt decline in global stresses indicates rupture. On a global scale, each sample behaves differently, where the onset of rupture corresponds to different ultimate stresses (e.g. sample 13 ruptures with a stress that is 30% greater than sample 36). The diversity in global material responses makes global predictions difficult.

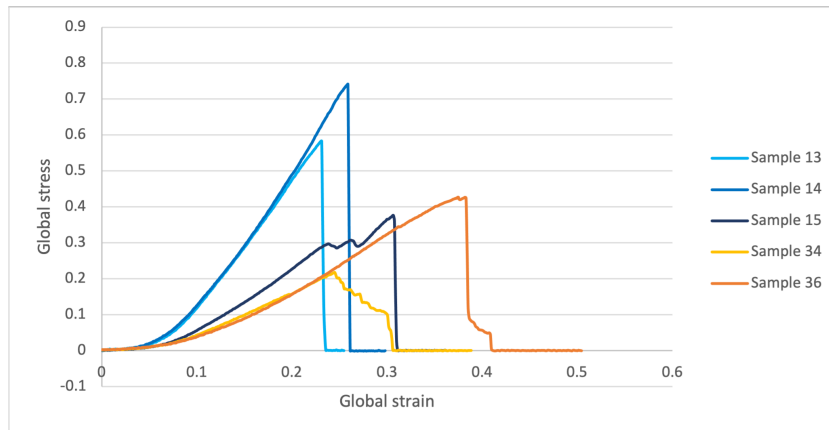


Figure 2.5: The global stress-strain relation between all preconditioned samples.

2.3.1. Theory of Digital Image Correlation

After pre-processing, the images from the mechanical test were fed into Ncorr, the mathematical DIC software used in this project. Its functionality, algorithm and parameters are described in detail by appendix D. Ncorr iteratively runs through every sequential image, referred to as the *current* frame, and performs a comparative analysis between the *reference* (the first image in the stack) and current frames. The relative displacements per subset are found by mapping each 'deformed' subset back to its undeformed state, guided by the speckle pattern. These are then collected into 2D displacement maps, which describe deformation as rigid body translations in the vertical (V) and horizontal (U) directions.

The Green-Lagrangian and the Eulerian-Almansi strains are two different descriptions of deformation, and use the U and V displacement maps to derive local strain fields. A simple schematic to highlight their difference is presented in figure 2.6. In 2D DIC, the Green-Lagrangian strain preserves the tissue dimensions of the reference frame because it considers cumulative deformation. Contrarily, the Eulerian-Almansi strain is based on instantaneous lengths, causing its ROI to grow after every iteration.

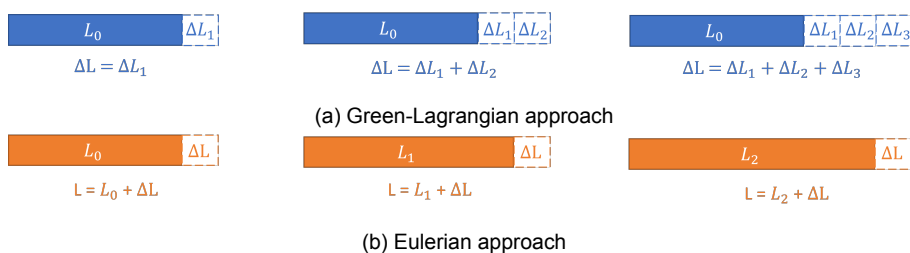


Figure 2.6: Two approaches of calculating strain ($\varepsilon = \delta L/L_0$)

This report has selected the Green-Lagrangian approach to calculate the strain maps because the ROI dimensions are unchanged throughout its calculation. The calculation of the local strains follows the following operations.

$$\varepsilon_{xx} = \frac{1}{2} \left(2 \frac{\partial u}{\partial x} + \left(\frac{\partial u}{\partial x} \right)^2 + \left(\frac{\partial v}{\partial x} \right)^2 \right) \quad (2.1)$$

$$\varepsilon_{xy} = \frac{1}{2} \left(\frac{\partial u}{\partial x} + \frac{\partial v}{\partial x} + \frac{\partial u}{\partial x} \frac{\partial u}{\partial y} + \frac{\partial v}{\partial x} \frac{\partial v}{\partial y} \right) \quad (2.2)$$

$$\varepsilon_{yy} = \frac{1}{2} \left(2 \frac{\partial v}{\partial y} + \left(\frac{\partial u}{\partial y} \right)^2 + \left(\frac{\partial v}{\partial y} \right)^2 \right) \quad (2.3)$$

These three strain entities describe three different phenomena. The ε_{xy} strain maps can capture local irregular deformation and allow the observation of rotational deformation. This is not visible in ε_{xx} and ε_{yy} strain maps, whose components are immediately related to rigid body translations in the x and y directions. This report extracts the ε_{xx} , ε_{xy} and ε_{yy} strain maps to conduct local strain analysis

2.4. Local strain analysis

This section summarises the analytical approaches and methodologies used to answer this projects main aims, introduced in chapter 1. This encompasses the consideration of the *ultimate* and *physiological* strain states during the tensile test. The *ultimate* state corresponds to the final image or frame where the tissue remains visually undamaged, while the *physiological* state corresponds to the frame that experiences a global strain of 10% [42, 49, 50]. Figure 2.7 summarises the points in the experiment to which these frames correspond. The interpretation of a physiological situation is important for clinical applications, as early detection of mechanical markers may be useful in vulnerable plaque detection.

The differences between these frames were assessed through qualitative visual interpretation and a quantitative metric based on the Structural Similarity Index (SSIM). This Matlab based function inspects the quality of the resemblance between images, scaled between 0 and 1. Its mathematical background is briefly described in appendix J.

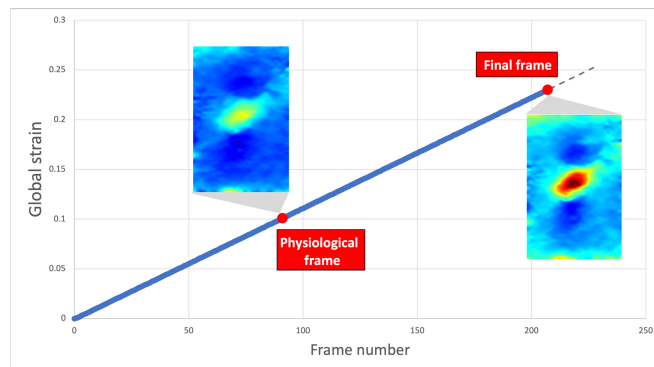


Figure 2.7: The global tissue response obtained during the uniaxial tensile test. The marked frames correspond to the analysed final and physiological frames.

2.4.1. Obtaining tissue coordinates of special features

Before starting the analysis, a visual distinction was made between the fibrous tissue of the cap and the SI to facilitate the interpretation of material heterogeneity. This was achieved with ImageJ (Fiji), a software that offers direct identification of pixel coordinates. The boundary coordinates of the SI were manually approximated with the ImageJ oval tool and then used to visually mark the outline of the SI in the strain plots. Next, the location of SI and fibrous tissue rupture were identified with the rectangular tool in ImageJ. *SI rupture* is the location where the separation of the SI initiated. Similarly, *fibrous tissue rupture* indicates the location where the separation of fibrous tissue is initiated. The coordinates of these rupture boxes were also marked in the strain plots. Appendix C describes these steps in more detail.

2.4.2. Strain patterns and rupture location

The steps taken to investigate the relationship between the local strain patterns and the rupture location are summarised in figure 2.8.

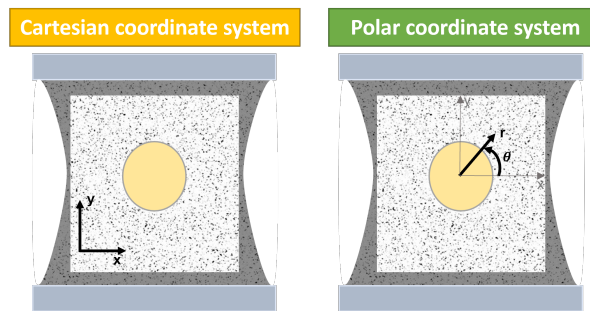


Figure 2.8: Physiological and ultimate time frames were analysed in a cartesian and polar coordinate system. This analysis includes the inspection of strains and their failure criteria.

First, strains adhering to the cartesian coordinate system ($\epsilon_{xx}, \epsilon_{xy}, \epsilon_{yy}$) were inspected through qualitative and quantitative means. This included finding strain magnitudes and seeking recurring patterns or unique visual features.

Next, the local strains were transformed to follow the polar coordinate system, defined in appendix G. Polar strains ($\epsilon_{\theta\theta}, \epsilon_{\theta r}, \epsilon_{rr}$) follow a circular orientation, where the origin lies at the centre of the SI. As was done for the cartesian coordinate system, all polar strain maps were analyzed qualitatively and quantitatively. Their results are described in appendix I.

Finally, the rupture likelihood was estimated by calculating two strain-based failure criteria for each coordinate system. These establish a united perspective of different strains and express their combined effect. Moreover, energy measures have shown a high accuracy in their approximation of rupture sites, showing a good colocalisation between the energy maxima and the location of rupture [15, 36, 37].

The first criteria is the *maximal nominal strain*, defined by:

$$F_{max\ nominal} = \max\left(\frac{\epsilon_{11}}{\epsilon_{11}^{max+}}, \frac{\epsilon_{12}}{\epsilon_{12}^{max+}}, \frac{\epsilon_{22}}{\epsilon_{22}^{max+}}\right) \quad (2.4)$$

which carries the largest normalised local strains to its output. The second failure criterion is the *quadratic strain criterion*:

$$F_{quadratic} = \max\left(\frac{\epsilon_{11}}{\epsilon_{11}^{max}}\right) + \max\left(\frac{\epsilon_{12}}{\epsilon_{12}^{max}}\right) + \max\left(\frac{\epsilon_{22}}{\epsilon_{22}^{max}}\right) \quad (2.5)$$

which is a summation of all normalized strains.

2.4.3. Local strain maxima and rupture location

As is summarised in figure 2.9, the relationship between local maxima and tissue rupture was investigated for four scenarios.

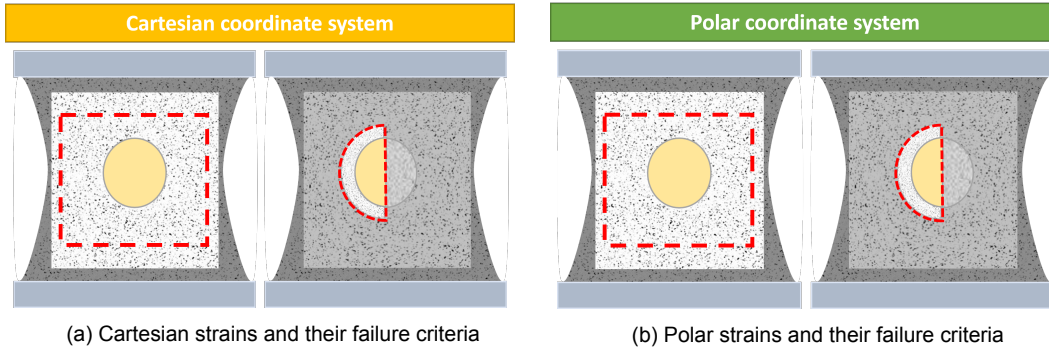


Figure 2.9: The steps taken to identify the relationship between local maxima and rupture in the final and physiological frames. The red dotted boundary indicate the region from where data is included for the evaluation of maxima.

Two regions were defined for the cartesian and polar coordinate systems; the tissue within the entire ROI and a zoomed perspective of the SI. While the inspection of the ROI allows for the evaluation of strains in the entire tissue, it does not explicitly focus on the location of rupture. Moreover, it may be tainted with artefacts that can bias the results. Their results are discussed in appendix F. The zoomed perspective isolates the SI and surrounding tissue better and focuses the analysis on the area of interest. Since the tissue is symmetric, it can be decomposed into two different plaque constituents. Only the tissue half where rupture ensues was selected to inspect the mechanics for a single cap.

Several measures were taken to improve the reliability of this analysis. The red boundary indicates the site from which ten local maxima were selected for qualitative and quantitative analysis. Their dimensions were chosen to minimize the effect of artefacts and outliers, as is further discussed in appendix E. Analyzing multiple maxima reduces the risk of bias from noise and outliers. The selection of the number of maxima was based on a trade-off between visual obstruction, reliability and selectivity. While a singular point may show extreme strains due to sensitivity to artefacts and outliers, excessively large group sizes compromise the visibility of the strain map and the distinction between different strain modes. When considering ten points, minimal clustering of points and blending of different strain modes was observed.

A Matlab script was employed to find the magnitudes of the maxima and derive their euclidean distance to the center of the SI rupture boxes. While the magnitude of the points was found by a simple *find* function, the derivation of distances followed a trigonometric formula in combination with a metric ratio.

$$Distance = d_{mm/element} \sqrt{\left(x_{SI \text{ rupture box}} - x_{point}\right)^2 + \left(y_{SI \text{ rupture box}} - y_{point}\right)^2} \quad (2.6)$$

2.4.4. Partitioned local strains

The down-sampling of data minimizes the effect of outliers and focuses data on the relevant features. Therefore, the strain maps were segmented into radial slices, following the *pizza-slice* approach described in appendix H. As is presented in figure 2.10, the slices, defined by lines intersecting at the centre of the SI, increment in powers of two. Hence, the segmentation of the SI and its surrounding tissue ring is symmetric. Another feature of this segmentation

approach is the tunability of the segmentation orientation. Different angular offsets may be applied to alter the data per slice. To remain detectable for clinical intravascular ultrasound (IVUS), with a reasonable resolution, the circumferential length of each segment was required to be bigger than 0.5 mm [40, 51, 41].

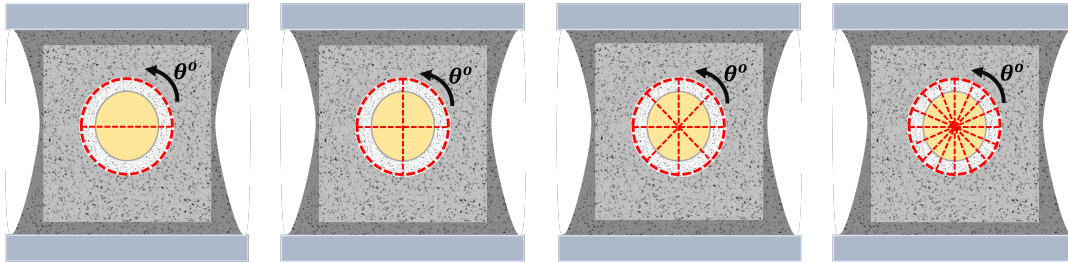


Figure 2.10: Segmentation of the central tissue area allows up to 16 partitions during segmentation. As is described by appendix H, the segmentation orientation is adaptable.

3

Results

This chapter addresses the results essential for shaping the goal of this report. Its framework follows the work timeline, from data acquisition to data interpretation. The first section qualitatively assesses the different patterns generated from the mechanical tests and relates them to the underlying biological constituents. The second section introduces the progression of mechanical failure and extends its occurrence onto the strain maps. Finally, the third section divulges the details of the local analysis of the strain maps, where the rupture location is related to the main aims of this report.

As can be inferred from the multitude of analytical approaches discussed in chapter 2, there is an abundance of data generated from the mechanical tests. However, to establish clarity within this chapter, only cartesian data from the final frame of a single sample undergoes deep qualitative and quantitative analysis. Information about other data sets and coordinate systems can be found in appendices I and E.

3.1. Pattern analysis

In the visual acquisition of tissue deformation, the relative movements of speckle patterns are translated into vector fields. These capture the relative distances travelled and strains experienced by each subset within the ROI. This section qualitatively interprets the patterns expressed by each field.

3.1.1. Displacement fields

The first step in DIC is measuring the relative deformation per subset. This is expressed by U and V displacement fields, which embody subset-based rigid body transformations in horizontal and vertical directions. They are inherently dependent on the material properties of the tissue. For instance, homogeneous tissues would show uniformity in their deformation, such that the U and V displacement fields are a sequence of regular-shape displacement modes whose magnitudes are symmetric about the central axis. However, the tissue engineered constructs show heterogeneity in their constituents, reflected in their derived displacement maps. These maps are shown in figure 3.1.

The magnitude of the V displacement field in figure 3.1a ranges between -0.8 to 0.8 from top to bottom. This indicates that the tissue moves with equal magnitude in opposing directions. Positive displacements infer movement along the positive y-direction (down), while negative displacements imply the opposite. The map is symmetric about the x-axis, where displacements are high in the shoulder regions and zero in the mid-cap. Notably, the middle region, where the tissue shows minimal displacement, is narrow in the centre of the figure,

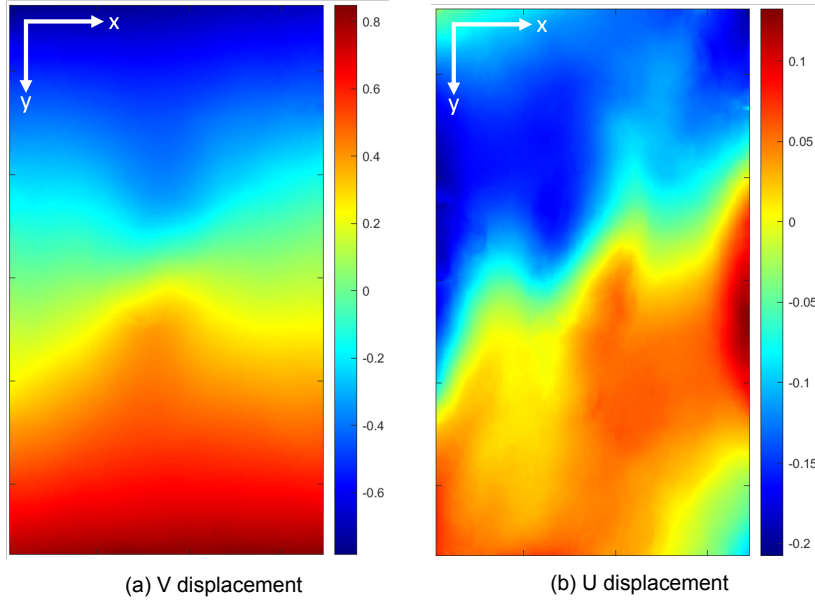


Figure 3.1: Displacement fields of the tissue engineered sample

establishing an hourglass shape. This location coincides with the position of the SI, thereby suggesting it has a mechanical role in the tissue response. For instance, lower mechanical rigidity of the SI could warrant the observed infiltration of large vertical displacements in the mid-cap.

The magnitude of the U displacement field ranges between -0.25 to 0.2 and represents tissue movement along the x-direction. However, its pattern diverges significantly from the expected response, which should be perpendicular to the V displacement field pattern. Instead of showing symmetry about the y-axis, its pattern appears rotated, following a diagonal to the global axis system. Consequently, large negative U displacements lie in the top left shoulder, while large positive U displacements lie at the bottom right shoulder of the tissue. This signifies that the top and bottom of the tissue move outward in opposite horizontal directions. Moreover, the arrangement of the displacement modes does not follow an orderly or systematic pattern. The distortion identifies wiggling shapes, indicating non-uniform tissue deformation.

The produced patterns are not unique for the presented sample. Most tissue inspected by this report share traits with the presented displacement fields in figure 3.1.

3.1.2. Strain fields

The strain patterns produced by DIC are presented in figure 3.2, where different strain regions can be identified based on colour. As was predicted from the displacement fields, local ε_{xx} , ε_{xy} and ε_{yy} strains develop inhomogeneously and progress towards accumulations of high and low strain. For this report, values corresponding to green-yellow are the allocated threshold for high strains, and those to navy are the threshold for low strains. These descriptions solely serve to facilitate the indiscriminate recognition of strain patterns.

The pattern of the ε_{xx} strain field is nearly biaxially symmetric. Figure 3.2a shows that regions with high (above 0.1) and low (below -0.05) ε_{xx} strain align themselves with the y-direction, in an alternating fashion. The three 'stripes' of high positive ε_{xx} strain lie along the edges and centre of the ROI. Here, the underlying tissue experiences extension along the x-direction. The greatest extension is measured at the left edge of the ROI, where the local strain magnitude is over 1.5 times larger than anywhere else in the tissue. The high strain

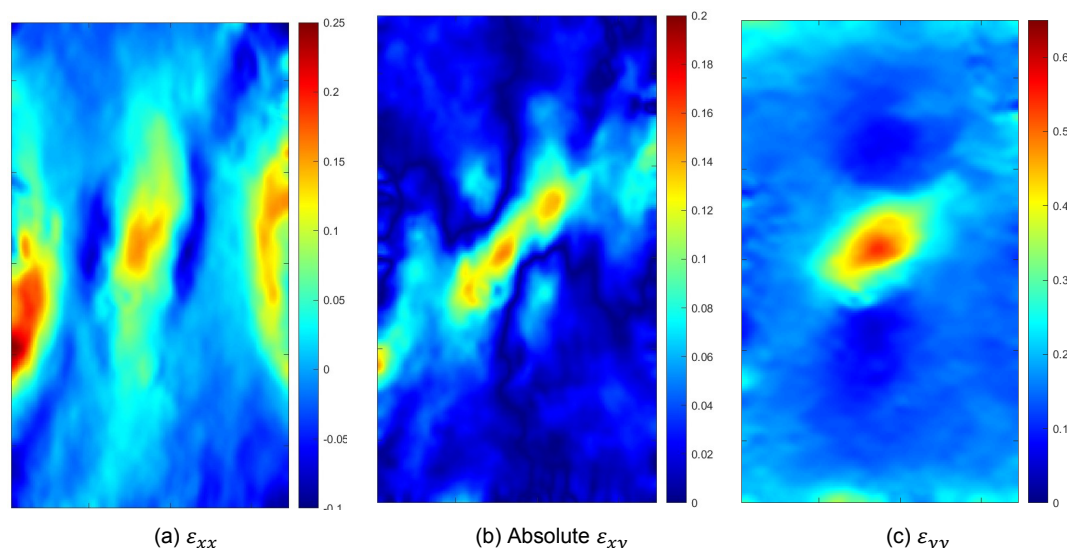


Figure 3.2: DIC produces ε_{xx} , ε_{xy} and ε_{yy} strains maps of the ROI in the experimental image. The color maps indicate regions of high (dark red) and low (dark blue) local strain. The shear strain is a symmetric entity [52], and is therefore presented in its absolute form. Note that experimental images underwent processing before being fed into Ncorr. The selected strain fields correspond to the final frame before tissue rupture, where the tissue engineered construct experiences a global strain of 0.23 in the y-direction.

regions are separated by two ‘stripes’ of low ε_{xx} strain, which manifest at the periphery of the SI. Their slightly negative nature indicates that the local tissue experiences compression along the x-direction.

The ε_{xy} strain is presented in figure 3.2b and expresses the absolute Lagrangian shear strains measured for the sample. A single region of high strain (greater than 0.12) passes through the centre of the tissue at a diagonal. High shear strains indicate that the underlying tissue experiences an incredible amount of geometrical deformation. Remarkably, the remainder of the field mainly consists of low strains, where those with the lowest magnitude manoeuvre through the tissue as thin wavering lines. Note that shear strains can be expressed as an absolute entity because of their symmetry. As a result, there are no negative ε_{xy} strains in the figure.

The ε_{yy} strain field captures strains with respect to the y-axis. In the distribution of figure 3.2c, high ε_{yy} strains (more than 0.4) lie concentrated at the centre of the tissue. In the shape of an oval, tilted about its axis, the ε_{yy} strain increases towards a single global maximum, which is over three times higher than those detected in the ε_{xx} and ε_{xy} strain fields. This orientation and location match that of the high ε_{xy} strain region. There are no other notable patterns found outside the centre of the tissue, demonstrating that most vertical extension occurs here.

The described patterns are not unique for the presented samples. Despite the discrepancy in their magnitudes, other samples find similar distributions (see Appendix E).

3.1.3. Failure criteria

The two strain-based failure criteria identified in chapter 2 produce the maps presented in figure 3.3. The values expressed by these maps correlate with the plausibility of tissue fracture.

The maximal nominal strain criterium map contains three regions with high failure magnitudes (greater than 0.6) located at the edges and centre of the ROI. This pattern diverges from that of the ε_{xx} map, as the central high strain region passes diagonally through the SI. This

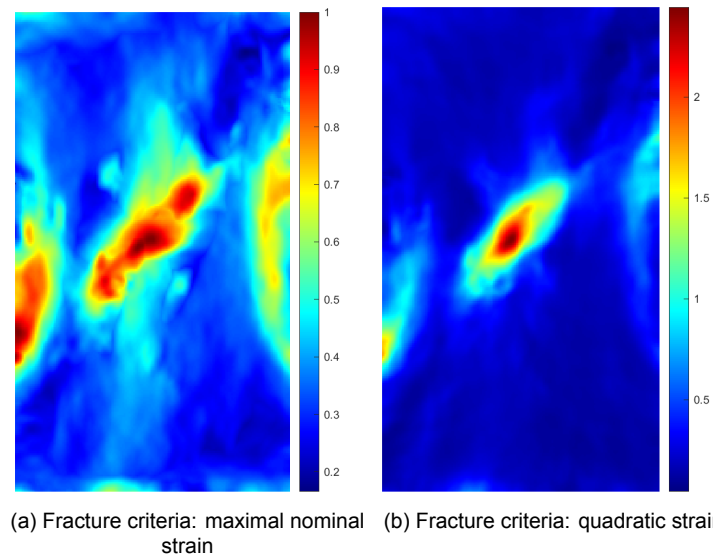


Figure 3.3: Strain-based failure criteria.

shape carries a resemblance to the ε_{xy} and ε_{yy} distributions. Therefore, it is evident that the pattern of the nominal strain criterium expresses the high strain regions of each strain map. Consequently, there are two regions with the highest nominal strain within the map: centre and left edges. According to the failure criterion, both sites poses the most risk to rupture.

The quadratic strain relation combines all normalised strains to produce figure 3.3b. Therefore, the map's scale is three times greater than that of the nominal strain criterium. A single high-valued region (greater than 1.5) lies at the centre of the map. Its morphology is similar to the high strain regions in the ε_{xy} and ε_{yy} maps. The quadratic strain is low in the rest of the tissue, and therefore unlikely to rupture. Note that this analysis ignores the high-valued region at the boundary of the ROI, as it lies outside the border defined by appendix J.

The patterns of the failure criteria show slight variation between other samples. While their exact magnitudes may differ, the shape and location of the identifiable high strain regions show great likeness to the fields described above.

3.2. Rupture mechanics

Rupture is the most common form of mechanical failure in atherosclerotic plaque caps [12, 13]. Understanding its basic progression is therefore essential in answering the objective of this report. The uniaxial tensile tests could successfully replicate rupture through persistent straining. This section discusses the observed tissue behaviour during rupture and associates its occurrence to strain field patterns.

3.2.1. Rupture phases

Figure 3.4 presents the observed response of the tissue engineered constructs during the mechanical failure. It shows that rupture is not instantaneous but rather a process of sequential events.

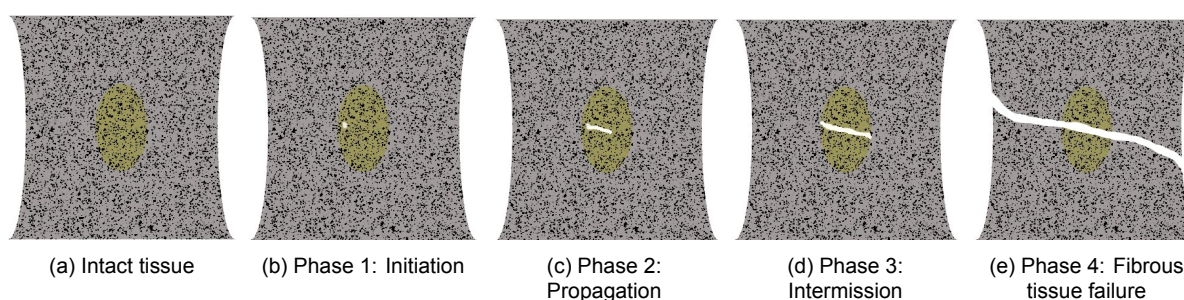


Figure 3.4: Four phases of rupture identified in the tissue engineered samples.

The general trend in which rupture occurred is summarised in figure 3.4. Each phase was assigned a descriptive title to distinguish between the phases. The first phase, **initiation**, occurs within the SI and can be recognised by the formation of a first ‘crack’ that separates local tissue (see figure 3.4b). Next, persisting stress pushes the crack to the periphery of the SI. For all five samples, the **propagation** direction was nearly horizontal (see figure 3.4c). It halts briefly once the crack reaches the interface between the SI and the fibrous tissue. During this **intermission**, the SI is completely separated, while the fibrous tissue remains intact (see figure 3.4d). The final phase in rupture occurs when the applied force exceeds the fibrous tissue strength. As is presented in figure 3.4e, the tissue splits diagonally. **Fibrous tissue rupture** happens almost instantaneously, going from a state of partial to complete rupture nearly within a single frame. Because of the low camera capture rate, it is unknown if more rupture phases exist. Fibrous tissue rupture is, therefore, regarded as an immediate event.

In this report, *rupture* is an umbrella term, which entails each of the above phases. Henceforth, any reference to this term will address the entire process (*initiation, propagation, intermission* and *fibrous tissue rupture*), unless explicitly stated otherwise.

3.2.2. Rupture location

While the exact location of rupture varies per sample, it always occurs in the mid-cap region. Figure 3.5 summarises the dynamic rupture process for all samples. The white ellipse at the middle of the tissue represents the outline of the SI, facilitating the visual interpretation of tissue heterogeneity. The black boxes inside the ellipse identify the locations of rupture initiation (the first phase of rupture). As this box signifies the initial position of SI separation, it is entitled the *SI rupture box*. The black boxes coincide with the vertical centre of the SI, lying at the SI and fibrous tissue interface for all samples. The two white boxes at the left and right sides of the SI draw attention to the location of fibrous tissue rupture. Additionally, they indicate the pathway

and orientation of the fracture line through the SI. These thereby acquire the title *fibrous tissue rupture boxes*.

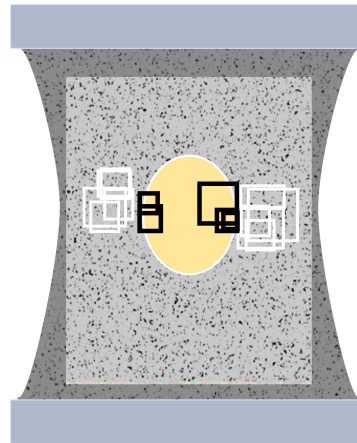


Figure 3.5: Rupture locations throughout all samples. The white ellipse represents the SI outline, the black box surrounds sites of rupture initiation, and the white boxes distinguish the areas of fibrous tissue rupture.

3.2.3. Rupture in strain fields

The marked ε_{xx} , ε_{xy} and ε_{yy} strain maps are presented in figure 3.6. They connect the sample-specific rupture event to its strain patterns.

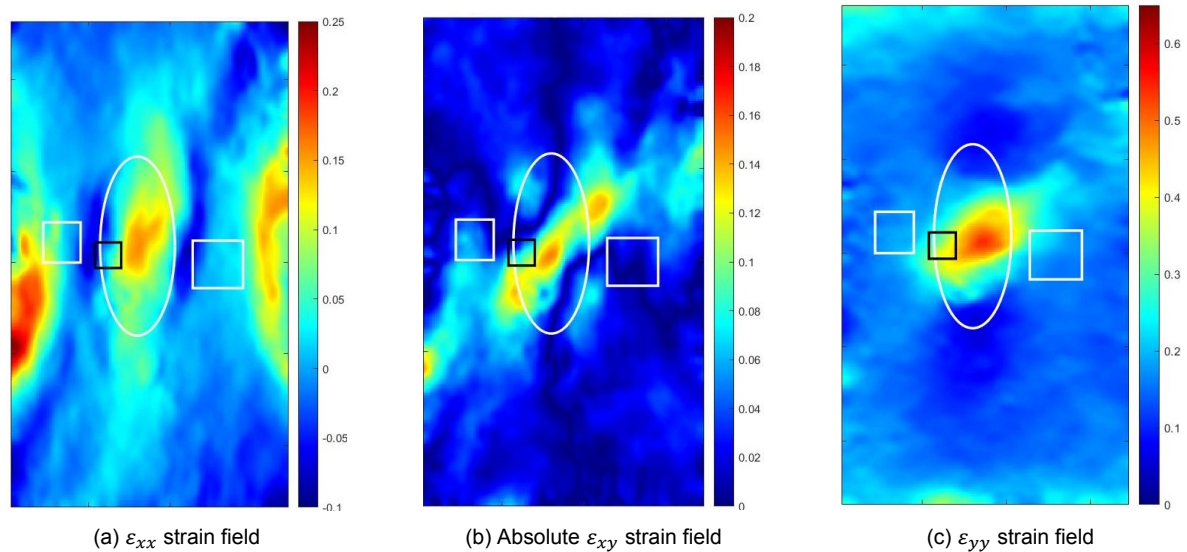


Figure 3.6: Marked strain field maps before SI rupture. Rupture of the SI and fibrous tissue initiate at the black and white rectangles respectively. The shape and boundary of the SI is indicated by the white oval at the center of the images.

In the ε_{xx} map, the SI rupture box lies between the high strain region and the edge of SI in the mid-cap. Consequently, the box overlays a transition between high (0.11) and low (-0.07) strains, which corresponds to nearly half of the total strain range measured for the entire tissue (-0.1 to 0.25). The fibrous tissue rupture boxes overlay areas adjacent to the SI, with comparable high and low strain values. Because the dimensions of these boxes are consistently larger than the SI rupture boxes, the shift in strains is more gradual,

The location of the SI rupture box also corresponds to a region that experiences a large transition in ε_{xy} strains. In figure 3.6b, the box encapsulates shear strains between between 0.01 and 0.1. Comparing this to the full spectrum of the strain map (0 to 0.15), the enormity of this gradient becomes evident (60%). On the other hand, the fibrous tissue rupture boxes associate with inhomogeneously distributed low shear strains (close to 0). These appear to lie away from the high shear region intersecting the SI.

In the ε_{yy} strain distribution, the SI rupture box again overlays a sharp transition between high and low strain modes. The strain within the black box ranges between 0.24 and 0.44, which is a significant portion of the entire strain spectrum (0.05 to 0.54). By inspecting all samples, a subtle trend emerges between the shape of the high strain area and the location of the SI rupture box. In all instances, its position overlays the edge of the high strain regions and correlates with its high curvature end. Contrastingly, the fibrous tissue rupture boxes overlay nearly homogeneously distributed low strains. These boxes do not appear to co-localise with distinct or unique strain field patterns, as was observed for the ε_{xy} map.

Although the exact underlying strain values vary (see appendix E), the inter-sample differences are minimal. Therefore, all observations mentioned above are consistent for all samples.

3.3. Local analysis

Rupture initiation is consistently observed within the boundary of the SI (see subsection 3.2.2). To isolate this area of interest, the ROI is adjusted to accommodate only the SI and its surrounding tissue. This modification additionally reduces bias from artefacts along the tissue border (see appendix J). Figure 3.7 summarises the framework of the local analysis. Cartesian strains and their failure criteria will be qualitatively and quantitatively analysed in-depth to address both research objectives of this report. First, the relationship between rupture initiation and the field patterns is investigated by segmenting the modified ROI into radial data ‘slices’. Second, ten local maxima for all fields are computed and related to the rupture location. Finally, a modest comparative study between the final and physiological frames achieves relevance to a clinical setting.

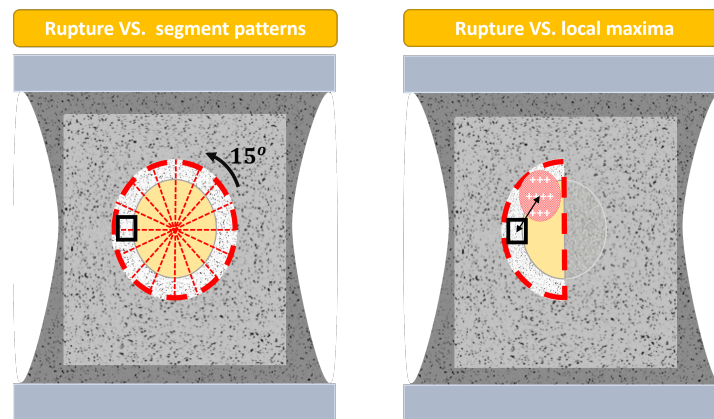


Figure 3.7: The local analysis of the cartesian strains and their failure criteria focuses on the SI and its surrounding tissue.

3.3.1. Rupture vs. segment patterns

The cartesian strain maps and failure criteria were segmented through the pizza-slice approach. In summary, the data within the modified ROI was cut into individual ‘slices’ according to a predetermined angle to produce sets of segmented data points. The data within each slice is presented as a boxplot to identify unique patterns indicative of rupture. For simplicity, the figures only exhibit data based on a 16-fold segmentation and an angular offset of 15° . Based on the work described in appendix H, these parameters isolate the rupture location with the best resolution. The segments that capture the SI rupture box are highlighted with a green circle around their segment number. Henceforth, these segments will be entitled the *rupture segments*. For all boxplots, the y-axis represents the magnitude of the strain or fracture criteria, while the x-axis enumerates the segment number. The bottom and top of the boxes correspond to the 25th- and 75th percentiles of the data sets, collectively defining the interquartile range. The red line through the middle of each box is the population-based median. Off-centred lines indicate the skewness in the population. Finally, the whiskers that extend above and below the boxes show the maximum and minimum data values that are not outliers.

Cartesian strains

The boxplots based on cartesian strains are presented in figure 3.8.

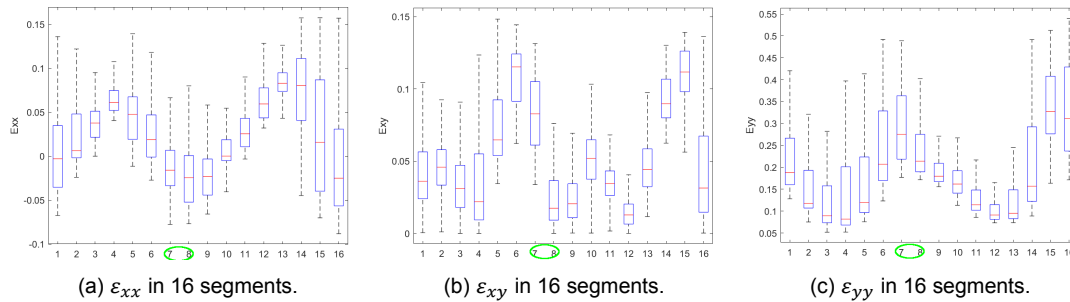


Figure 3.8: Boxplots of cartesian strains

The ε_{xx} boxplots follow a sinusoidal pattern, which originates from the alternating stripes of negative and positive strains. The peaks emerge at segments 4 and 12, their heights contrasting only a little. The rupture segments lie in a valley of the pattern where the strains are negative. In figure 3.8a, their medians correspond to a magnitude of approximately -0.02, which is indicative of nearly negligible compression.

The segmentation of the ε_{xy} strains produces figure 3.8b. The pattern shows that alternating small and big peaks emerge at segments 2, 6, 10 and 14. These correspond to the 'x' shaped high strain that passes through the SI. The rupture segments capture a relatively large shift in medial strain magnitude. In the figure, the median drops from 0.08 to 0.02, which is one of the greatest differences between sequential segments.

The segments of the ε_{yy} distribution also follows a sinusoidal pattern, as is presented in figure 3.8c. Two peaks of different heights emerge in segments 7 and 15. The rupture segments correspond to the second highest peak in the map, where the median strains are between 0.28 and 0.21.

Comparison of the responses within the entire sample group reveals that most of the samples agree with the above observation. Unfortunately, no distinctive features exist to motivate in which valley or peak rupture occurs for the ε_{xx} and ε_{yy} distributions. The relative peak height, skewness, interquartile range, and whisker length of the rupture segments are never constant across samples. Notable, samples with slippage and damage divert from the observations. Their local mechanical response appears distorted from the intact tissues with nearly monotonous distributions and irregular shear strain patterns in the rupture segments.

Failure criteria

The transformation of the cartesian strains into the failure criteria produce the following boxplots.

The nominal strains generate an oscillating pattern, much like a sinusoid. It peaks nascent at segments 6 and 15, mismatching in height. This nearly symmetric pattern likely originates from the diagonal high-value region through the centre of the tissue. In figure 3.9a the rupture segments contain medium nominal strains between 0.35 to 0.6. Although this transition is very steep, the boxplots overlap greatly, making it less noticeable. However, the strains within the rupture segments span the full amplitude of the pattern.

The quadratic strain criteria also produce oscillating patterns, climaxing at the same segments as the nominal strain boxplot. Similarly, the rupture segments in the figure 3.9b lie

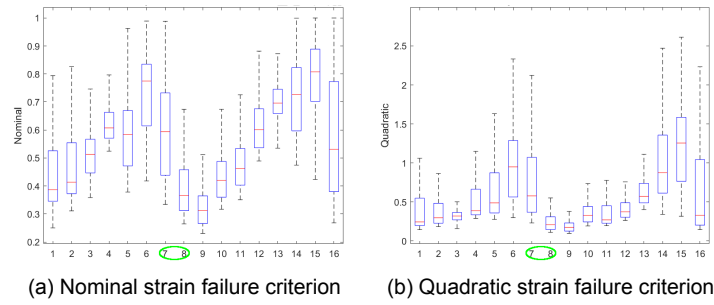


Figure 3.9: Boxplots of cartesian failure criteria

between a peak and valley, with medial values between 0.3 and 0.6. Notably, these magnitudes do not differ much from those measured for the nominal strains, although they are proportionally much smaller than the nominal strains.

Unfortunately, these observations cannot be extended to all other samples. While most showed similar results, the damaged tissues produced a flat boxplot pattern. Especially the nominal strain boxplots do not show a consistent relationship between the position of the ruptured segments and the pattern for damaged tissues. They can lie at a peak instead of the transition region, depending on the sample.

3.3.2. Rupture vs. local maxima

This subsection inspects the relationship between rupture and local maxima within the adjusted ROI (see figure 3.5). To ensure statistical significance, this analysis inspects the collective behaviour of the strain maps and failure criteria fields throughout all samples.

Cartesian strains

Figure 3.10 summarises the detected strain magnitudes and their respective distances from the rupture initiation site.

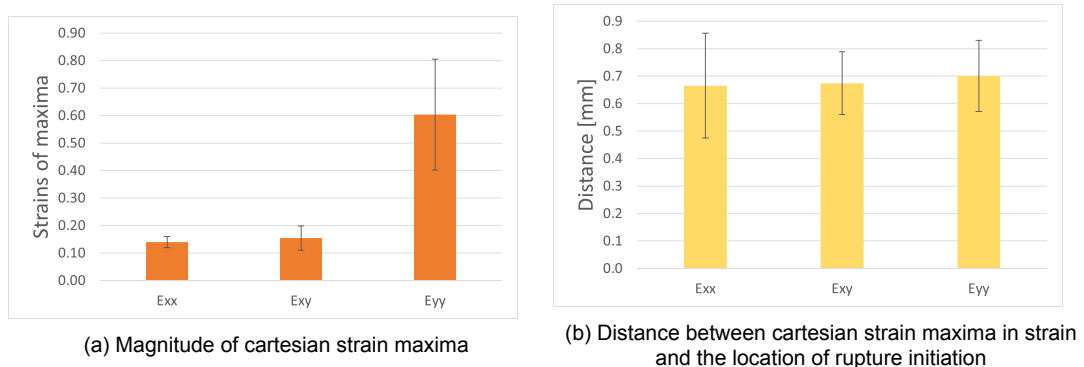


Figure 3.10: Local analysis of cartesian strain maxima

The ε_{xx} maxima reach an average magnitude of 0.14 ± 0.02 , which lie less than 1 mm from the rupture location. For the magnitude chart, these maxima show the smallest standard deviation, which suggests a good agreement between the strains measured of all samples. However, they show the greatest difference in distance to the centre of the SI rupture box. With a standard deviation of 0.2 mm, the maxima are therefore least consistent in their approximation to the rupture site.

The average magnitude and distances of the ε_{xy} maxima show a nearly insignificant difference from the ε_{xx} maxima. With strains and lengths of 0.15 ± 0.04 and 0.7 ± 0.1 mm, respectively, both maps deliver nearly identical information. While the standard deviation for strain magnitude and the accuracy of the location are both doubled, they do not manifest in novel observations.

Finally, the ε_{yy} maxima are represented by the final bar in both graphs of figure 3.10. As was recognised during pattern analysis, the average strains of the ε_{yy} maxima are threefold the magnitude in other directions. With strains of 0.6 ± 0.2 , these maxima also vary significantly across samples, with a standard nearly ten times greater than those presented for the ε_{xx} strain maxima. Despite this discrepancy, their performance in estimating the rupture location is highly comparable to the other strain directions. The distance reported by figure 3.10b identifies a distance of 0.7 ± 0.1 mm, which is nearly unchanged from the other maxima.

Failure criteria

The magnitudes of the failure criteria maxima and their corresponding distances to the rupture site are summarised in figure 3.11.

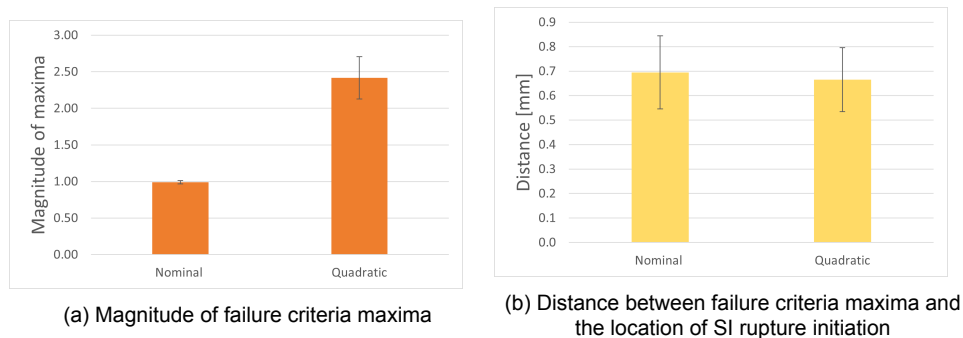


Figure 3.11: Local analysis of cartesian failure criteria. Note that the magnitudes of both criteria are scaled differently (0 to 1 for the nominal strain, and 0 to 3 for quadratic strain).

The nominal strain criterion has an average magnitude of 0.99 ± 0.02 , showing that the maxima correspond to this criterion's largest values. Once again, the slight standard deviation implies good agreement across all samples. Furthermore, the distance to these maxima (0.7 ± 0.2 mm) is comparable to the distances measured for individual strain maps.

While the nominal strains appear significantly smaller than those of the quadratic strain criterion (2.21 ± 0.29), they are scaled between 0 and 1. Therefore, the relative average magnitude of the quadratic strain maxima is smaller. Nevertheless, their precision is comparable. They perform equally at estimating the rupture site with a distance of 0.7 mm of identical accuracy.

3.3.3. Physiological frame

Strain distributions at 10% global strain are similar to those found at the final frame. Visual inspection of the fields of both frames shows that the patterns emerge early within the mechanical experiment. The figures presenting the physiological frames can be found in appendix E. The $\varepsilon_{xx}^1 0\%$ field is near-symmetric, with three high strains emerging at the exact locations as their final counterparts. Similarly, the $\varepsilon_{xy}^1 0\%$ and $\varepsilon_{yy}^1 0\%$ fields find elongated high strain regions at the centre of the tissue and follow the same morphology as in the final frames. The only notable differences are the increased effects of noise or clamping artefacts found around the borders. These become increasingly dominant under low global strains. The similarity

was also quantitatively measured with the 'Structural Similarity index', introduced in chapter 2. Table 3.1 summarises the data generated from the comparison of all fields between the two frames.

Table 3.1: The structural similarity between the final and physiological frame. Note that the SSIM is scaled between 0 and 1.

ε_{xx}	ε_{xy}	ε_{yy}	Maximum nominal strain	Quadratic strain
0.53	0.77	0.77	0.85	0.76

With all SSIM values above 0.5, it can be assumed that the morphology and organisation of the patterns show minimal variation between the frames.

The consistency is also reflected in the segment patterns following the partition of the SI and its surrounding tissue (see appendix H). For all samples, the boxplots patterns remain nearly unchanged. Hence, the previously mentioned observations concerning the relationship between strain and failure criteria patterns are detectable at physiological global strains.

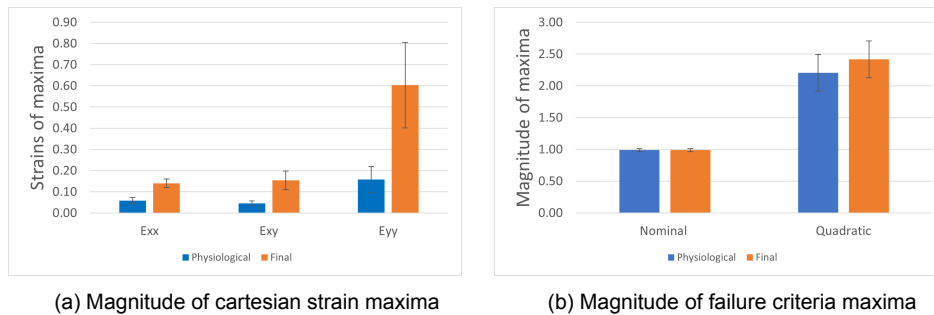


Figure 3.12: Comparison between final and physiological frames.

The magnitudes of the local strains in the physiological frame are significantly lower than at the final frame. As is presented in figure 3.12a, the difference is approximately equivalent to 60%-70% of the final local strains. Consequently, the highest local strain is approximately 0.15.

Notably, no significant change exists in the magnitudes of the failure criteria maps. Being products of the normalised strain maps, the nominal and quadratic strain fields appear insensitive to changes in global strains.

Figure 3.13 summarises the distances for all fields. The first discernable observation from this graph is the consistency in the location of all maxima. The collective estimative power of the average distances of the physiological frame lies between 0.6 to 0.7 mm, while the distances in the final frame are 0.7 mm. None of these distances changes significantly between the frames. However, the exact average distances show dissimilarity, the inter-sample variances obscure direct evidence for a single best metric to estimate the rupture site.

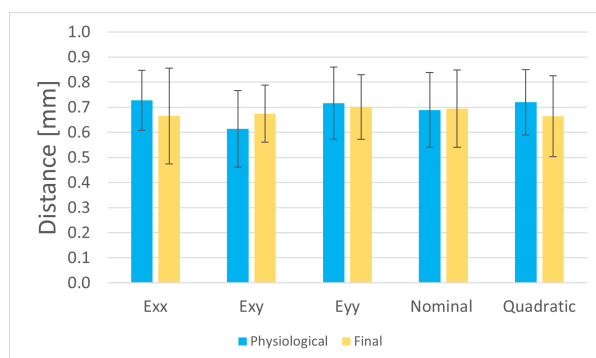
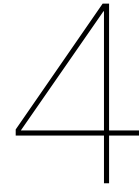


Figure 3.13: Distance between maxima of strain and failure criteria maps and the location of SI rupture initiation. Comparison between final and physiological frames.



Discussion

This report assembles a pipeline for fingerprinting the strain maps of mechanically tested tissue engineered plaques. By calculating the strain fields of the pre-processed raw images with digital image correlation (DIC), the onset of its rupture was correlated to local strains through different techniques. These included inspecting local strain patterns and local strain maxima in the final frame before rupture and the physiological (10% global strain) frame.

4.1. Image pre-processing

The performance of DIC was considerably enhanced by pre-processing the raw images obtained from the uniaxial tensile tests. After evaluating the effects of different approaches, the combination of appropriate cropping and a Gaussian filter with a 2.5 radius was deemed the most effective yet simplistic optimising technique. Unfortunately, this pre-processing filter was optimised to suit the circumstantial situation specific to the included samples. If these circumstances change, the optimisation process must be repeated to find the ideal filter for the images.

The pre-processing of images was an essential step in this report. The speckle pattern is the most crucial element for calculating the strain fields. As is explained in appendix D, they are used to measure the deformation of the object. Therefore, the reliability of the strain maps is directly influenced by the robustness of the pattern. An ideal pattern must have a unique distribution, 50% coverage, and equally sized speckles. In truth, however, the speckle pattern of tissue constructs was uniquely but unevenly distributed, with speckles of various sizes, which often clumped together to form large clusters. This inadequate pattern could therefore generate incorrect or unreliable strain maps. Moreover, the images were marred with other visual artefacts (i.e. shadows and reflections). These must be corrected to prevent bias in the strain maps.

4.2. Pattern analysis

Chapter 3 disclosed the patterns of the displacement, strain and failure criteria maps of the tissue engineered samples created by Wissing et al. (2021) [42]. These patterns were individually analysed and compared to the field patterns of other tissue engineered samples. This section sequentially reviews the maps, reasons the emergence of the patterns and evaluates their clinical significance. Note that reference to a *true* response corresponds to the results obtained by DIC.

The displacement maps express the relative vertical and horizontal translations of each subset. Accordingly, the V displacement maps were vertically symmetric in the top and bottom tissue halves, with thicker regions of high vertical displacement directly above and below the SI. This pattern indicates that the centre of the tissue underwent more vertical deformation than the edges. On the other hand, the patterns of the U displacement maps were symmetric about a diagonal, and its modes followed zigzagging shapes. This indicates that the diagonally opposite corners of the tissue moved in different directions along the horizontal axis (i.e. the left top corner experienced negative U displacement, while the right bottom corner experienced positive U displacement).

The expected response of the tissue construct has been modelled by Serra (2020) [44], who used a finite element analysis model to mimic the mechanical experiment. In her work, she established the simplistic geometry presented in figure 4.1, which features a rectangular shape interrupted by a semi-circular gap at the right edge. The two-dimensional model was assigned hyperelastic, non-linear, homogeneous, isotropic and incompressible material properties, which match properties often used by numerical publications that address the biomechanics of plaques in computational models [43, 53, 15, 54]. This simulation, therefore, ignores the mechanical contribution of the collagenous fibres and the stiffness of the SI.

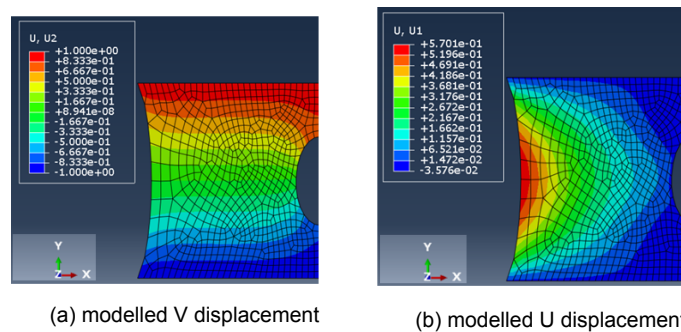


Figure 4.1: The predicted behavior of a finite element geometry that resembles the tissue engineered constructs. Note that the SI is modelled as a hole with zero stiffness. Images obtained from the master thesis of Serra (2020) [44].

Substantial similarity exists between the patterns of the *true* (figure 3.1a) and *modelled* (figure 4.1a) V-displacement maps. The discrepancies in the material properties of both tissues are not evident in their comparison. The absence of abstract patterns or inconsistencies between the V-displacement fields could suggest that the geometry of the fibrous tissue has a stronger effect on the vertical deformation than its biological composition.

Contrastingly, the modelled U displacement fields are dissimilar from the true tissue construct response. Aside from their distinct symmetry axis orientations, the predicted patterns do not follow a zigzagging path. These differences could be attributed to clamping artefacts or discrepancies in material properties, although the latter is unlikely for several reasons. First, the tissue engineered caps were carefully constructed to maintain a rigid biaxial symmetry, both in geometry and biological structure. Governed by fixed dimensions, the tissues con-

structs conform to a rectangular shape of 10 mm by 15 mm, whose exact centres were filled with a 2mm wide lipidic core. The distribution of the collagen fibres, the leading regulator of the mechanical strength, was also stringently controlled. Collagen staining, microscopy and histological assays by Wissing et al. (2021) [42] reported regularity and symmetry in the collagen fibre architecture, affirming the load-bearing symmetry between quadrants of the tissue construct (see figure 2.3). Secondly, the constructs were relatively homogeneous in structure, aside from their collagenous and lipidic constituents. Infiltrates often found in clinical plaques, such as calcifications and other cellular debris, were absent from the constructs and can thus not cause aberrations in the U displacement field.

Alternatively, clamping artefacts (e.g. slippage at the clamping site or misalignment between the tissue and the clamp) are a more probable cause of the observed differences between the U displacement patterns. They are products of poor interaction between the tissue construct and clamp surface. The diverse set of different U displacement patterns observed in appendix E show the poor reproducibility of the displacement patterns, thereby indicating its sensitivity to experimental circumstances. Hence, it is likely that the distortion of the displacement field is a consequence of the mechanical grip malfunction.

The high percentage of clamp-site failures in the entire sample group of Wissing et al. (2021) supports the viability of mechanical interference from the clamps. As is disclosed in appendix A, approximately 86% of all samples underwent mechanical failure at the clamp site during the mechanical tests [44, 42]. However, this is not uncommon for uniaxial tensile tests [15] Studies have found different percentages of failure at the clamp interface, which vary depending on the material and its shape. In Holzapfer et al. (2004), approximately 23% samples failed outside the region of interest, while in Sang et al. (2018) identified a failure amount of 86% or 6% for rectangular and dog-bone shaped tissues, respectively [15, 55].

The second set of patterns described by section 3.1 were those of the ε_{xx} , ε_{xy} and ε_{yy} strain maps, which relay the Green-Lagrangian local normal and local shear strains in the tissue (equations 2.1, 2.2 and 2.3). The fields were a mix of high and low strains, which indicate extension and compression along their respective axes (see figure 3.2).

In the ε_{xx} fields, three regions of high strains congregated to long vertical shapes at the tissue edges and centre, creating a near biaxial symmetric pattern. This pattern was unchanged throughout all samples. Contrastingly, the high strain regions in the ε_{xy} and ε_{yy} fields formed elongated or elliptical shapes, intersecting the SI diagonally. Their orientation changed per sample (see appendix E). Albeit the slight differences seen between the strain fields of each sample, the systematic recurrence of the patterns indicates a robust reproducibility in the main loading direction.

The true strain fields diverge from the modelled response by Serra (2020) [44] (see figure 4.2). For instance, the ε_{xx}^{FEA} fields expect the tissue edges to compress instead of undergoing extension. Similarly, the predicted 'x'-shaped intersection of high ε_{xy}^{FEA} strains was not observed in the true ε_{xy} fields. Only the ε_{yy}^{FEA} strains find a good agreement with the expected pattern, where the high strains accumulate at the in the SI. Nevertheless, the true ε_{yy} magnitudes below and above the SI never reach below zero, suggesting the compression does not occur in the actual tissue.

The difference between the true and modelled strain maps suggest that the geometry no longer dominates the mechanical tissue response. Other factors, such as clamping and collagen fibre distribution, could be the root of the different mechanical behaviour. The direct relationship between displacements and strains dictates that previously mentioned aberrations in the U and V displacements maps carried into the strain maps. Based on the images in appendix E, these artefacts were especially noticeable along the tissue edges, which were

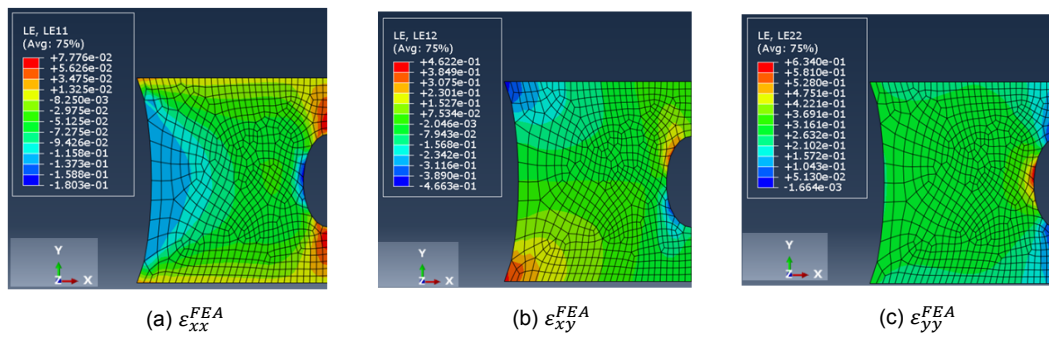


Figure 4.2: The predicted behavior of a finite element geometry that resembles the tissue engineered constructs. Images obtain from the master thesis of Serra [44].

scattered high and low strains regions.

Collagen fibres highly influence tissue strength and stiffness [42, 56], thereby playing a potential role in dispersing strains through the structure. Wissing et al. (2021) showed that the infiltration of collagen fibres in the SI did not match the densities found in the fibrous tissue and that fibres at its interface followed a range of different orientations. The master thesis of Swaab (2021) [57] investigated the local fibre organisation in the fibrous tissue of the same constructs analysed in this project. He identified improved alignment of the fibres with the y-axis towards the luminal edges of the tissue, which corroborates with increased stiffness along the same axis. Moreover, he performed extensive FEM simulations to simulate the mechanical response of a geometry that mimicked the fibre organisation in the fibrous tissue. Concurring with the results of DIC, the stiffer luminal tissue edges measured lower strains. Accordingly, it can be deduced that the SI has a lower resistance to deformation and should indeed experience higher strains.

If the observations hold in a clinical setting, the lipidic core (represented by the SI) will have the lowest stiffness and strength. Therefore, it should experience the highest strains in the plaque. This expectation is in line with clinical observations by De Korte et al. (2002), who consistently found fatty plaques to associate with higher strains than fibrous plaques [39].

Finally, the strains were combined into two different pure-strain failure criteria (equations 2.4 and 2.5) to grade the chance of failure. Their selection was motivated by the absence of local stress data and the local material parameters of the tissue construct.

The values in the two resulting maps correspond to the rupture likelihood. Once a failure criterion reaches the critical threshold of 1, the corresponding tissue is expected to rupture. Notably, the produced maps in figure 3.3 identified multiple regions that surpassed this criterion. The quadratic strain and the nominal strain maps had three such regions. These were located at the luminal edges of the construct and in its centre. This indicates that rupture could start at the centre or edges of the tissue. However, the magnitude of the high-valued region at the centre of the quadratic map far exceeds the magnitude of the other regions. Hence, it allocates a greater rupture likelihood to the centre of the tissue.

4.3. Rupture analysis

All samples included in this project underwent mechanical failure in the mid-cap region. As is indicated by the cross-sectional schematic in figure 2.3, the mid-cap is characterised by a wide SI encapsulated by a narrow fibrous cap. This description corroborates with attributes associated with vulnerable plaques (i.e. large necrotic cores and thin fibrous caps) [18, 27].

Mechanical testing showed that rupture in the mid-cap occurred in four phases: initiation,

propagation, intermission and fibrous tissue rupture. This process was regularly observed in all included samples, indicating that the experiments are highly reproducible. First, a small crack forms near the interface with the fibrous tissue and propagates to both ends of the SI. Then, after a brief intermission, the fibrous tissue separates instantaneously. This process is summarised in figure 3.4.

Distinct rupture phases are suggestive of discrete underlying strengths or mechanical properties. For instance, the fibrous tissue of the construct is hypothesised to have greater strength or stiffness as it remains intact longer than the SI. As previously discussed, collagen fibres are the likely root of these contrasting properties. The fibrous tissue is abundant in anisotropic load-bearing collagen fibres, whereas the SI showed a lack thereof.

The onset of rupture in the engineered constructs showed a likeness to the rupture mechanics in atherosclerotic plaques. Firstly, the global strains corresponding to the point of rupture initiation (see figure 2.5) matched the 15% to 60% strain range reported in literature [58]. These values correspond to the mechanical failure range for circumferentially tensed aortic intima plaques. Secondly, rupture occurs at the narrowest region of the fibrous tissue of the engineered construct, an event commonly observed in *ex vivo* atherosclerotic plaques [10, 14]. It concurs with the notion that cap thinning is associated with plaque vulnerability and increased likelihood of rupture [59, 23]. Finally, the maintained integrity of the fibrous tissue during the first rupture phase is not a novelty. A study by Daemen et al. (2016) on intraplaque haemorrhage identified rupture to initiate between two tissue planes without disrupting the continuity of the fibrous cap.

The sequential phases show that the rupture path has a consistent trajectory. Rupture of the tissue engineered plaques always initiates within the SI, representing the necrotic core, and propagates towards the luminal surface of the fibrous cap. This directionality differs from theories that propose rupture due to cap destabilisation. These are mainly collagenase-driven theories, built on the degenerative function of macrophage products. Macrophages in the cap produce matrix metalloproteinases (MMPs) which digest collagen fibres. Upon critical loading, local disturbances in the collagen fibre network (e.g. due to the activity of MMPs) cause the separation of the matrix in a chain reaction for rupture [60]. Hence, the fracture line propagates inward.

As the tissue engineered caps do not contain macrophages, their collagen fibres remain unaffected by MMPs. Therefore, a possible interpretation of their mechanical failure is that plaque types devoid of macrophage infiltration could undergo rupture according to the presented internal failure mechanism.

Further inspection of the rupture direction shows that the fracture line follows different propagation paths in different tissue sections. The SI separates in a gentle diagonal line, offset only slightly from the horizontal. This path increases its angular offset upon entering the fibrous tissue, as is presented in figure 3.4. The crooked rupture path could indicate that inhomogeneously distributed collagen fibres (inconsistent anisotropy and density) disperse the tensile force unevenly through the tissue, leading to the accumulation of different local stiffnesses and stress modes. Unfortunately, clinical observations of the rupture mechanics do not yet exist because *in vivo* imaging is challenging. Therefore we cannot refute or support the observations in true plaques.

Finally, the rupture locations were related to the strain and failure criteria patterns by estimating SI and fibrous tissue rupture initiation sites. Consequently, it was possible to identify the features commonly associated with rupture. This is summarised in table 4.1.

As was previously suggested, the SI has a lower load-bearing capacity, which would imply that it should undergo the greatest deformation. The first observation from each strain map

Table 4.1: Relation between strain patterns and rupture

	SI rupture initiation	Fibrous tissue rupture
Cartesian strains	In the all maps, the strains undergo a transition of high to low strains (relavite for each map).	In ε_{xx} maps, the strains undergo a transition of high to low strains. In the ε_{xy} and ε_{yy} maps, the strain is low.
Cartesian failure criteria	In both maps, the fracture criteria under go transition from high to low values.	Occur where the fracture criteria is low.

was the accumulation of high strains in the middle of the cap. According to the marked strain maps (figure 3.6), these regions lie within the boundary of SI, affirming the predicted behaviour.

Several numerical studies have suggested a link between high strains and plaque rupture [61, 39, 62, 54]. Although the thesis remains unconfirmed, they proposed that rupture occurs in the vicinity of a high strain region. Table 4.1 offers simple proof that for a minimalistic tissue-engineered plaque cap mimic, such a relationship indeed exists. The location of rupture initiation in the SI always lies at the edge of a high strain region.

Based on the topology of the strain maps, the relationship between rupture and high strain regions appears to follow the steepest-descent approach. This signifies that the rupture pah follows the sharpest gradient in strains. Accordingly, the orientation of the ε_{xy} and ε_{yy} high strain regions described before counters the diagonal path of the fracture line. For instance, when the fracture line is tilted to the right, the ε_{xy} and ε_{yy} high strain regions are tilted to the left, and vice versa.

4.4. Local strain analysis

The local analysis of the strain maps was restricted to the SI and its surrounding tissue. As was mentioned in chapters 2 and 3, this allows for a better inspection of the strain patterns close to the onset of rupture.

4.4.1. Segmented patterns and rupture

In the first approach of local analysis, the zoomed region was divided into individual data sets, following the pizza-slice segmentation approach described in appendix H. A single revolution about the SI revealed a repetitive pattern between the segments, indicating that the opposite sides of the SI showed similar mechanical behaviour. This stems from the high strain regions that intersect the SI and are consequently captured by opposite segments.

The association between the segment patterns and rupture was achieved by identifying which segments geometrically overlapped with the location of rupture initiation. The main results of this investigation are summarised in table 4.2. These results hold for most samples, which is another admonition to the experiment's reproducibility. Importantly, the mechanical tests elicit similar responses regardless of the different loading protocols that samples were subjected to during culturing.

The descriptions of the results are reasonably generic. For instance, while rupture associates the ε_{yy} strain peak, there is no criterium for its height, width, or other unique features

Table 4.2: Relationship between boxplot patterns and rupture

Location of rupture	
ε_{xx}	At a valley (low medial strains)
ε_{xy}	Transition between high and low medial strains
ε_{yy}	At a peak (high medial strains)
$F_{Nominal}$	Transition between high and low medial strains
$F_{Quadratic}$	Transition between high and low medial strains

that help distinguish the rupture segments from its symmetric counterpart (e.g. the side on which rupture occurs). Moreover, the exact local strain values differ per sample. For instance, the medial segment strain at the rupture location can be around 0.21 for one sample and 0.34 for another. This indicates that strain magnitude is not the only determining factor for rupture. Several studies have repeatedly suggested that disturbances in the local biological composition may stimulate rupture [15, 35, 43]. Therefore, these results from segmentation motivate the integration for structural analysis of the tissues.

The repetition of the boxplot patterns stems from the mechanical symmetry of the geometry. Therefore, each iteration of the pattern belongs to half the geometry, which resembles a single plaque. When considering the patterns in half of the geometry only, the valleys and peaks of the segmented ε_{xx} and ε_{yy} strain maps are unique. In such a situation, the rupture location colocalises with the maximal ε_{yy} and minimal ε_{xx} boxplot strains. The peaks and valleys in the boxplot patterns can therefore serve as markers for the rupture location. The uncertainty of this estimate corresponds to the width of the segments, which lies within a 45° range from the centre of the SI.

4.4.2. Local maxima and rupture

In the second approach of local analysis, the geometrical symmetry of the construct was broken by eliminating the unruptured half of the samples. Then, the tissue half of interest was analysed by inspecting the local maxima of the strain and failure criteria fields.

As was already evident from the displacement fields, the V fields measured the largest displacements, suggesting that the vertical axis should experience the greatest deformation and strain. This expectation held true, as the ε_{yy} strain fields measured the highest strains. The maximal strains reach around 0.5, which is easily detectable in vivo. Several studies reported strains as small as 0.01 to be measurable with intravascular ultrasound (IVUS) [39, 23]. Even the ε_{xx} and ε_{xy} maxima, at half this magnitude, are therefore also measurable.

Combining the individual strain fields through the different failure criteria realised two maps with different ranges, whose maxima are summarised in figure 3.11a. The nominal strain criterion ($F_{nominal}$), which is scaled between 0 to 1, reaches the ultimate magnitude for their range in all samples. However, the quadratic strain criterion ($F_{quadratic}$) consistently fails to satisfy its ultimate 0 to 3 range. The significance of this observation is that the maxima of the individual strain maps (ε_{xx} , ε_{xy} and ε_{yy}) do not overlap (see equation 2.5). Instead, their high strain regions accumulate at different positions within the SI such that the quadratic addition of their normalised strains fails to reach 3. This suggests that the mechanical properties of the tissue construct are different in each direction, where any local disturbances to the tissue structure may have different effects on the strain components.

High strains are typically associated with the infiltration of biological material (macrophages), lower collagen content, and thinner plaque caps [23]. Therefore, IVUS studies from Schaar

et al. (2003) and others have proposed using high strain peaks as indicators for vulnerability [23, 62, 61]. This report attempted to validate this hypothesis by calculating the average length between the local maxima of the strain and failure criteria fields and the sites of rupture initiation. The average distances measured for every map lay around 0.7 mm, showing that all perform similarly at approximating the location of rupture initiation. However, since the radius of the SI itself is only 1 mm, the precision of this approximation is relatively poor. Therefore, employing high strains of failure as markers of rupture leaves room for uncertainty.

The standard deviation measured for the magnitudes and distances across the sample group is substantial. This was unexpected as the culturing conditions of the constructs and the execution of mechanical tests were strictly controlled. The histological analyses by Wissing et al. (2021) found negligible variances in the arrangement of collagenous tissue [42]. Circumstantial data (e.g. dynamic culturing protocols, tissue integrity and clamping artefacts) could elucidate the observed differences between the samples. Due to the minimal availability of samples fulfilling the criteria mentioned in section 2.1, constructs belonging to different mechanical protocols were mixed in this report. The continuous and intermittent straining protocols (see section 2.1) follow different dynamic loading cycles, leading to the development of materials with different inherent strengths.

Moreover, two of the five samples had minor damages in their structure. These pre-existing cracks in SI could distort strain patterns, leading to the accumulation of atypically high strains. The greatest source of distortion, however, follows from clamping malfunctions. Insufficient friction at the uniaxial clamps can result in contractile tissue movement, known as *slippage*, allowing the measured strains to drop significantly. These causes (different dynamic protocols, clamping malfunction, and damage to tissue integrity) can lie at the root of the high standard deviation detected.

4.4.3. Physiological frame

Current diagnostics lack biomarkers that accurately measure plaque vulnerability within clinical settings. This report aims to bridge this gap by analysing intraplaque strain fields that are attainable through imaging techniques like IVUS [23, 39, 62]. A physiological state was selected to represent tensile forces measured *in vivo* and establish clinical relevance. The physiological state corresponds to the frame at which the global strain is 10%. This value was based on reported circumferential strains measured for atherosclerotic caps [42, 49, 50]. Moreover, it corresponds to the threshold beyond which endothelial cells are assumed to be more sensitive towards shear stresses [59].

The physiological frames were compared with the final frame by inspecting the visual similarity of all field patterns, the segment patterns, and the local maxima. All three approaches identified an uncanny resemblance between the two frames. This suggests that most conclusions from the final frame can be extended to a physiological setting. Therefore, this report encourages further experimentation with tissue-engineered constructs following their clinical potential.

The first endeavour proved the consistency between the frames through elementary visual observations and quantitative evaluation, where the calculated structural similarity (SSIM) index (scaled between 0 and 1) always reached above 0.5. The second approach identified nearly identical segment patterns in the boxplots of both frames, whose relationship with the rupture location was unchanged. Albeit the halved magnitude, the segmentation of the circular selection proved to be another admonition to the previously found similarity.

Finally, the magnitudes and distances of the maxima in both frames were compared. As was expected, the magnitudes of the maxima were highly different. The local strain values reflected the 2.3 fold reduction in global tension experienced by the tissue. Nevertheless, the

corresponding local strain magnitudes remained above the measurable threshold of IVUS [39, 23]. The maxima locations showed a minimal difference between the frames, which concurs with the previously mentioned consistency in field patterns. The average distances ranged between 0.6 and 0.7 mm for both frames. Similarly, the standard deviations measured for the final frame remained nearly unchanged, indicating that inter-sample variance is already evident early in the mechanical test. Therefore, the unique biomechanical behaviours of different samples could be detectable at the physiological frame.

4.5. Limitations

The study encountered several setbacks, which limited the results of the study. This section discusses the most significant limitations of this report.

Firstly, a low camera capture rate deterred the investigation of rupture mechanics. At 15 Hz, it was impossible to identify the exact rupture initiation point. This uncertainty directly affected the strains and patterns associated with rupture. This entails the identified strain magnitudes and the distances between the approximated rupture site and the strain feature of interest. Moreover, the low capture rate prevented the acquisition of the exact dynamics of fibrous tissue rupture. While current evaluations consider fibrous tissue rupture instantaneous, this could not be validated. Therefore, improving the capture rate improves the reliability of future results and may also discover new failure mechanics.

Clamping artefacts have also been proven to influence the results. The suboptimal fixation of the tissues to the uniaxial ledger was reflected in the results. Aside from distorting the U displacement fields, they caused artefacts at the tissue edges and often instigated rupture at the clamp site (see appendix A). This effect highly compromised the availability of samples for this report, leading to the inclusion of samples from different dynamic loading protocols that carried minor damages. The most unfortunate effect of suboptimal clamping was slippage, which distorted all fields. Although some strain patterns could still be retrieved, their magnitudes differed from the rest of the group.

Another limitation to the study is its two-dimensional perspective. As a three dimensional object, the tissue construct also shows changes in its thickness. However, by utilising 2D DIC and treating the data fields as 2D planes with no changes in thickness, the third dimension is entirely ignored. Although the thickness is much smaller than the tissue height and width, following the laws of volume conservation, the tissue must also adjust its size in the z-axis to accommodate for the tensile forces. Moreover, the local thickness of the tissue construct may also affect the location of rupture. For example, thinner tissue areas can endure lower tensile forces than locations with thicker tissue of identical composition. Because of its smaller cross-sectional area, lower collagen content, and lower stiffness will experience higher stresses, making it more susceptible to rupture.

Continuing on the notion of stresses, the final limitation discussed in this section concerns the lack of information about local stresses. By ignoring this entity, the mechanical response of the constructs is not fully represented. While strains quantify deformation, stresses measure an object's internal forces. Therefore stress and strain maps can vary greatly. For instance, while the SI measures high local strain, the edges of the tissue should experience high local stress due to the local anisotropic collagen fibre arrangement. Thus the tissue edges will endure a significant proportion of the global tensile stress to compensate for the weaker centre of the tissue.

5

Concluding remarks

5.1. Conclusions

The analysis of strain maps may offer a new window into diagnosing atherosclerotic plaques. The main findings identified by this study in achieving this objective are summarised below.

- Rupture analysis:
The mechanical failure of the tissue constructs did not occur instantaneously but followed a series of phases instead. In all samples, rupture initiates near the edge of the SI and propagates to its lateral boundaries. After a brief intermission of no more than 0.2 seconds, the fibrous tissue ruptures.
- Relationship between rupture and strain map patterns:
The position of rupture initiation always colocalises with the edge of a high strain or failure criteria region. Consequently, rupture overlies a gradient between high and low strains.
- Relationship between rupture and patterns from segmented data:
The radial division of strains in the zoomed SI region produces highly reproducible box-plot patterns. The segments that geometrically encompass the rupture locations repeatedly lie within identical pattern positions. For the ε_{xx} , ε_{xy} and ε_{yy} strains, these correspond to a valley, a transition between low and high medial strains, and a peak in the pattern, respectively. Similarly, the nominal and quadratic strain failure criteria overlie a transition between low and high medial strains.
- Relationship between rupture and local maxima:
The maxima of the strain- and failure criteria maps showed minimal standard deviation across the sample group, indicating that all samples had similar strain magnitudes. Additionally, the euclidean distance between the maxima and the rupture location varied minimally between the strain maps and failure criteria. Accordingly, each strain map performed similarly in estimating the location of rupture initiation. Therefore, the rupture locations were identified to lie near local strain maxima and failure criteria maxima.
- Comparing the patterns in final and physiological frames:
Despite the significantly lower magnitude of local strains in the physiological frames (10% global strain), the patterns of the strain- and failure criteria maps were highly similar to those identified in the final frame before rupture. Moreover, the boxplot patterns of

the zoomed SI perspective showed no changes in the patterns nor the relationship with rupture.

- Comparing the maxima in final and physiological frames:
The maxima of the individual physiological strain maps are more than two-fold lower than at the final frame. Only the magnitudes of the failure criteria maxima remain nearly unchanged. Additionally, the average Euclidean distances vary negligibly between the frames. Therefore, it is concluded that all maxima at the physiological frame lie at nearly identical locations in the final frames. Therefore, the relationship between the maxima and rupture location is identical for both frames.

5.2. Future prospective

In light of continued research on analogous topics, this section presents recommendations for future experiments and studies.

- Improve the mechanical experiments:
This project recommends a higher camera capture rate, improved lighting and speckle patterns, and a better clamping methodology to overcome the shortcomings of the extracted data. The current capture rate of 15 Hz proved inadequate at discerning rupture phases clearly. Increasing its acquisitive power should eliminate this limitation by a significant degree. Moreover, the surface features of the tissue did not show a 50% coverage of equally sized speckles in a unique architecture. Interference by poor lighting and an aberrant speckle distribution can significantly distort the derived strain maps and compromise their reliability. Finally, as was shown during pattern analysis in chapters 3 and 4, clamping effects were apparent in the produced patterns. Rotation, slippage and mechanical failure at the clamps should be minimised in future experiments. As has been recommended by the master thesis of Serra [44], employing a re-designed clamp may effectively improve the DIC output.
- Inspecting the topology of transition in the strain- and failure criteria maps:
The experiments showed a repeated association between the rupture location and a gradient in local strains. Quantifying these transitions may provide better insights into the relationship between material behaviour and strain maps.
- Inspecting tissue response at lower global strains:
The selected 10% global strain benchmark corresponds to the maximal circumferential strains measured in arteries [42, 49, 63]. The comparative analysis performed in this report between the physiological and final frames can be extended to inspect frames subjected to even lower strains.
- Integrate the mechanical observations with the underlying biological composition:
A hybrid perspective that evaluates the mechanical response of the tissue construct (i.e. strains, failure criteria and rupture behaviour) and the biological composition (i.e. the arrangement of the collagen architecture, continuity or fibre dispersion, and eventual other constituents) at the same time to improve the understanding of the mechanical events. By incorporating both mechanical and biological facets, a prospective study can link the previously stated observation with the local integrity of the tissue construct. This could elucidate the exact motivation for, for example, the exact location of rupture or the directionality in which it progresses.

- Inspecting strain rates:
The current approach evaluates single frames as discrete data sets. Hence, a prospective study can look at the continuity of the local strains by inspecting the local strain rates. The local evolution of strains and their developmental patterns may provide better insight into the behaviour of local tissue. As was demonstrated by lino et al. (2018), the *in vivo* local strain rates are different for healthy and diseased tissues. Accordingly, they reflect important local stiffnesses in a clinical setting [64]. Inspecting the role of strain rates in the constructs may improve the current understanding of rupture mechanisms and improve its predictability.
- Include a three-dimensional perspective:
As was indicated in section 4.5, this study encaptures two-dimensional data only. Future work could build on this limitation by including information about this third dimension of the tissue. Such options are, for example, acquiring the tissue thickness at specific locations during the experimental test or performing 3D DIC to include the effects of surface deformations. The tissue construct accommodates global stresses in all three dimensions to conserve its volume. The current approach fails to notice decreases in tissue thickness, which may restrict the interpretation of the mechanical responses. Therefore, further analysis of the strain maps could inspect the thicknesses of different tissue regions.
- Inspect local stress distribution:
When obtaining the local tissue thicknesses, it becomes possible to calculate the local stresses. The stresses can be collected and assembled into a coarse stress field. Future studies could enhance their mechanical analysis by evaluating strain maps and stress fields.
- Perform the same study with more complex tissue constructs:
Finally, the last suggestion is to increase the complexity of the tissue constructs. The current structure constitutes a remarkable basis for testing the mechanical responses of minimalistic plaque. However, *in vivo* plaques are highly complex, and the exact dynamics and mechanical roles of their constituents are still unconfirmed. The tissue engineered constructs offer a unique opportunity to introduce different plaque species (e.g. calcifications and cells) in a controlled manner and evaluate their mechanical consequences. Moreover, the results from this report can serve as a control against their effects can be determined.

Acknowledgements

I could have never gotten to where I am today without a few special people. First, I want to thank Frank Gijsen, who guided me through my literature study and thesis. He has continuously been there to support me in our many meetings. I have learned a lot from his analytical insight and problem approaching attitude. I also want to thank Hanneke Crielaard, my daily supervisor. She has constantly motivated me and encouraged me at every step in this thesis. I very much appreciate our brainstorming sessions, patience, random chats and all the time she spent helping me.

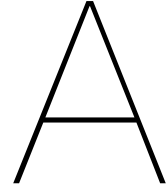
Moreover, I want to thank Sheila Serra, who helped me get started on my project and has been endlessly generous in sharing her work and expertise. I also would like to thank Ali Akyildiz and Kim van der Heiden for our numerous meetings and insight into this project. I really appreciate their input and patience during our brainstorming sessions.

My gratitude goes out to Mathias Peirlinck for being part of my examination committee.

I also thank everybody at the Cardiovascular Biomechanics department at the Erasmus MC for their feedback and encouragement. I have never been in a lab that feels so much like family.

Finally, I want to thank my family, friends and Erik for their continuous faith in me. Your support has helped me to successfully complete my thesis project.

Ranmadusha Hengst
December, 2021
Delft, The Netherlands



Sample database

The following table summarises the names, dynamic loading protocols and attributes of all samples created prior to this project. Based on the sample criteria mentioned in chapter 2, only five samples qualify for processing in this report. The corresponding samples are numbers 13, 14, 15, 34 and 36.

Table A.1: Database of all samples

Sample number	Experiment code	Loading protocol	Fracture at center	SI
1	STAT.P1.LC.W1	Static	no	yes
2	STAT.P1.LC.W2	Static	no	yes
3	STAT.P2.LC.W1	Static	no	yes
4	STAT.P2.LC.W2	Static	no	no
5	IS.P5.W2	Intermittent	no	no
6	IS.P5.W3	Intermittent	no	no
7	IS.P6.LC.W2	Intermittent	no	yes
8	IS.P8.LC.W1	Intermittent	no	yes
9	IS.P8.LC.W2	Intermittent	no	yes
10	CS.P7.W2	Continuous	no	no
11	CS.P7.W3	Continuous	no	no
12	CS.P7.W4	Continuous	no	no
13	CS.P2.LC.W2	Continuous	yes	yes
14	CS.P2.LC.W4	Continuous	yes	yes
15	CS.P2.LC.W5	Continuous	yes	yes
16	STAT.P3.W1	Intermittent	no	no
17	STAT.P3.W2	Intermittent	no	no
18	STAT.P4.W1	Intermittent	no	no
19	STAT.P1.W1	Intermittent	no	no
20	STAT.P1.W2	Intermittent	no	no
21	CS.P2.W1	Continuous	no	no
22	CS.P2.W2	Continuous	no	no
23	CS.P2.W3	Continuous	no	no
24	CS.P3.LC.W1	Continuous	no	yes
25	CS.P3.LC.W2	Continuous	no	yes
26	CS.P3.LC.W3	Continuous	no	yes
27	CS.P5.LC.W6	Continuous	no	yes
28	STAT.P5.W2	Static	no	no
29	STAT.P9.LC.W2	Static	no	yes
30	IS.P2.W1	Intermittent	no	no

31	IS.P4.W1	Intermittent	no	no
32	IS.P4.W2	Intermittent	no	no
33	IS.P1.LC.W5	Intermittent	no	yes
34	IS.P1.LC.W6	Intermittent	yes	yes
35	IS.P3.LC.W5	Intermittent	no	yes
36	IS.P3.LC.W6	Intermittent	yes	yes

B

Image pre-processing in ImageJ

This report requires a simplistic pre-processing technique that results in low-noise images, with good contrast between the background and speckle-pattern [65, 66]. This effect is summarized by figure B.1. The following criteria best define the basic and essential requirements of a technique:

1. **Distinguish noise from essential speckles.** If the filter removes essential speckles, no surface features remain to indicate local displacements. Moderation and selectivity are essential features of the filter to preserve DIC quality and reliability.
2. **Minimize the effect of outliers** that originate from reflections and shadows. Outliers are pixels whose values lie outside the expected range. For example, reflections result in brightly lit areas with exceedingly high pixel values. Removing outliers is equivalent to removing unwanted surface features that may hinder the image recognition algorithm of DIC.
3. **Improve the contrast between background and speckles.** Sharp colour contrasts between objects facilitate DIC image recognition.
4. **Should not consume a high processing time and computational power.**

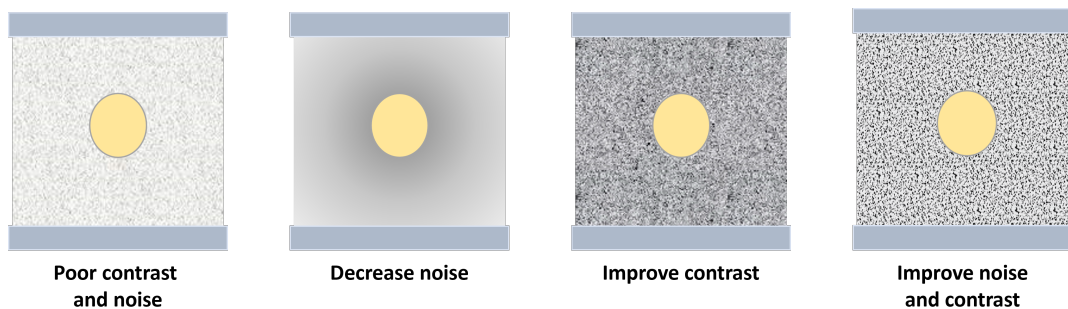


Figure B.1: The effect of improving the speckle patterns digitally. The image on the left has poor contrast and high noise. Too much noise reduction will produce the second image, where no speckles are anymore visible. This results in the loss of essential data used during tracking. The third image has much better contrast but is tainted by noise which might interfere with speckle identification. Optimization of both noise and contrast results in the right-most image, allowing the reliable DIC.

A set of different filters have been tested in this project to identify a simplistic image pre-processing:

- Cropping only
- Improving contrast
- Greyscale contrast
- Enhance local contrast function
- Gaussian filtering (blur)
- Background subtraction
- Intensity thresholding

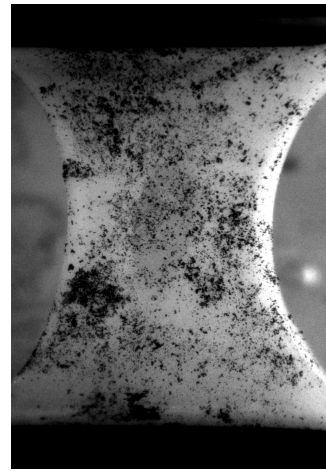
To avoid arbitrary and partial definitions of an 'optimal' processing approach, the comparison of these filters was based on two quantitative DIC metrics: the correlation coefficients of the subsets and the number of Gaussian iterations (described in appendix D). The smaller their values are, the better the performance of the given filter is. By comparing the final two images of the mechanical experiment, the most significant deformation from the state of the reference frame is captured. Coincidentally, these images also show the least agreement with the reference frame, so that they will reveal slight improvements to the image quality. For the purpose of reliability, several measures were taken to maintain maximal consistency within this comparison. This includes employing the same sample, seed placement and system parameters.



(a) Cropping



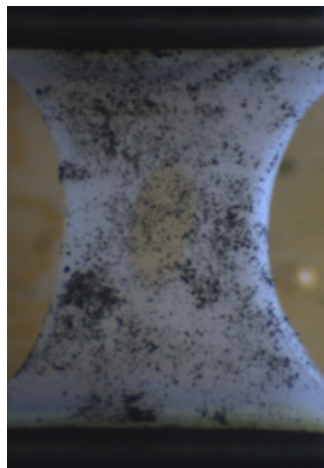
(b) Improve contrast



(c) Grayscale contrast



(d) Enhance local contrast function (ELCF)



(e) Gaussian filtering (blur)



(f) Background subtraction



(g) Intensity thresholding

B.1. Summary of the different filters

The techniques employed for image processing are described below. Note that for DIC, all images must terminate with a numerical value to indicate the sequence of the stack. This is achieved by looping through the entire file that contains the images and adding the iterative value to its end.

```
image_name = 'MyExample_';
inputFolder = 'getDirectory("choose input folder");
outputFolder = 'getDirectory("choose output folder");
list = getFiles(inputFolder);
setBatchMode(true);
for (i=0; i<list.length; i++){
...
saveAs("tiff", outputFolder+image_name+i);}
```

B.1.1. Cropping

All images were cropped with the below code. Images that did not receive any further processing than described in this subsection were identified as the threshold for performance improvement.

```
roix = ...;
roiy = ...;
roiwidth = ...;
roiheight = ...;
makeRectangle(roix, roiy, roiwidth, roiheight);
run("crop");
```

B.1.2. Improving contrast

```
setMinAndMax(55, 197);
run("Apply LUT");
```

B.1.3. Greyscale contrast

```
run("8-bit");
run("Brightness/Contrast...");
setMinAndMax("36.80", "163.45");
```

B.1.4. Enhance local contrast function

```
run("Enhance Local Contrast (CLAHE)", "blocksize=127 histogram=256 maximum=3 mas
```

B.1.5. Gaussian filtering (blur)

```
run("Gaussian Blur...", "sigma=4");
```

B.1.6. Background subtraction

This is also commonly known as 'top hat filtering'. It works as follows:

1. Convert to grey-scaled image
2. Take the dilated version

3. Take the eroded version.
4. Subtract the original image from the eroded version.

The code I used to perform this is as following:

```
run("Duplicate...", "title=Original");
run("8-bit");
makeRectangle(318, 174, 1947, 1464);
run("Crop");
run("Duplicate...", "title=C");
run("Gray Morphology", "radius=10 type=circle operator=dilate");
run("Gray Morphology", "radius=10 type=circle operator=erode");
imageCalculator("Subtract create 32-bit", "Original","C");
rename("R=10")
saveAs("Jpeg", "C:/Users/ranma/Documents/University/MEP/MEP docs/Expt_Images/Gen
```

B.1.7. Intensity thresholding

This should get rid of very bright images. This might work best through grey-scale images.

```
run("8-bit");
setAutoThreshold("Default");
setThreshold(108, 153);
run("Convert to Mask");
```

B.2. Evaluation of filters

The only filter that improved both metrics was the Gaussian blur. As a low pass filter, it attenuates high-frequency signals. Depending on the radius size, it can reduce the amount of noise in the image. However, this comes at the cost of loss of details and computational power. The larger the radius, the more pixels processed (e.g. for a radius of 9, 81 pixels are processed). Selecting the right radius was a trade-off between the two metrics, data loss and computational power during processing. Based on the extracted data, the author deemed a Gaussian radius of 2.5 suitable for the current speckle pattern and imaging technique. Its average correlation coefficient lay at 0.0179 and showed almost minimal variance. This is a five-fold improvement to the baseline. The mean number of Gaussian-Newton iterations lies around 11, which indicates that the computational efficiency of DIC has increased by two-fold.

The application of the filter has been automatized by means of a macro written for ImageJ. This code collectively crops, applies the filter and renames the images as required. Contact R.M. Hengst or H.Crielaard for this information.

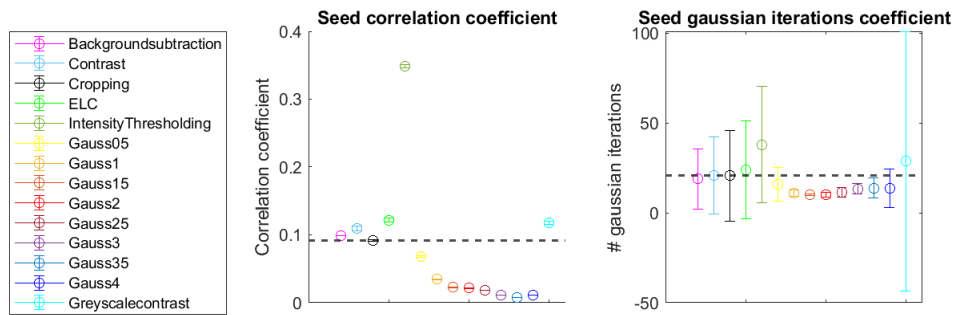
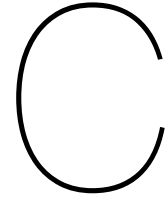


Figure B.3: Metric comparison of all image filters. The legend (on the right) relates each filter to a colour. The sixth filter has eight different versions, where the radius is changed to 0.5, 1, 1.5, 2, 2.5, 3, 3.5 and 4 pixels. The left graph indicates the least square correlation coefficient, while the right graph presents the number of iterations of each filter. To improve image quality, the value of the metric must lie below the baseline, which corresponds to the neutral effect of 'cropping'. The error bars correspond to the data variance.



Selecting tissue features

To facilitate the investigation regarding the relationship between local ε_{xx} , ε_{xy} and ε_{yy} strain modes, and SI and fibrous tissue rupture events, the established rupture site coordinates highlight the location of tissue failure in the local strain maps. Thus, they can be used to identify and analyse unique strain modes and patterns. Furthermore, attributing the strain maps with the SI boundaries may aid in the segmented interpretation of the two tissue materials and the consequence of heterogeneity on mechanical failure.

To complete the dictionary we need 7 ingredients.

- Image canvas size: X and Y dimensions
- Left Tissue rupture box: X coordinate, Y coordinate, Width, Height
- Right Tissue rupture box: X coordinate, Y coordinate, Width, Height
- SI rupture box: X coordinate, Y coordinate, Width, Height
- Frame that corresponds to the final rupture image
- Frame that corresponds to the physiological rupture image.
- SI bounding rectangle: X coordinate, Y coordinate, Width, Height

These coordinates must be corrected for movement from the original (reference) image. If the analyst fails to do so, the selected region does not match the actual rupture location.

This appendix provides the protocol for the whole process of completing the dictionary function by using sample 13 as an example.

The easiest method of selecting the right batch of images is by referring to the uniaxial log excel file. This entails the type of loading set, with their relevant time, force, displacement and length.

After finding the correct time when the protocols begin and end, all the corresponding images are imported into a separate file. Let us call it **Sample_13Original**.

The global strains per time can be calculated for each image by following formula:

$$[h]\varepsilon = \frac{\delta length}{length_0} \quad (C.1)$$

The physiological frame is selected by identifying at which frame the global strain is 10%.

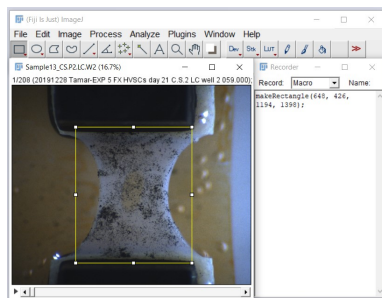
T	SetName	Cycle	Time_S	XSize_um	YSize_um	XDisplacement_um	YDisplacement_um	XForce_mN	YForce_mN
902	Y precondition 10%	10-Recover	59,72	5001	12731	0	126	4	7
903	Y precondition 10%	10-Recover	59,78	5001	12724	0	119	4	9
904	Y precondition 10%	10-Recover	59,85	5001	12689	0	84	4	7
905	Y precondition 10%	10-Recover	59,92	5001	12654	0	49	0	0
906	Y precondition 10%	10-Recover	59,98	5001	12624	0	19	-2	7
907	Y precondition 10%	10-Recover	60,05	5001	12605	0	0	0	7
908	Stretch until failure	1-Stretch	60,13	5006	12605	5	8	11	3
909	Stretch until failure	1-Stretch	60,19	5011	12625	10	20	4	7
910	Stretch until failure	1-Stretch	60,26	5017	12640	16	35	8	7
912	Stretch until failure	1-Stretch	60,33	5023	12655	22	50	6	5
913	Stretch until failure	1-Stretch	60,39	5028	12667	27	62	11	3
914	Stretch until failure	1-Stretch	60,46	5034	12682	33	77	8	9
915	Stretch until failure	1-Stretch	60,53	5040	12697	39	92	6	7
916	Stretch until failure	1-Stretch	60,59	5045	12709	44	104	4	13
917	Stretch until failure	1-Stretch	60,66	5051	12724	50	119	6	7
918	Stretch until failure	1-Stretch	60,73	5057	12739	56	134	11	3
919	Stretch until failure	1-Stretch	60,79	5062	12752	61	147	6	5
920	Stretch until failure	1-Stretch	60,86	5067	12766	66	161	4	9
921	Stretch until failure	1-Stretch	60,93	5073	12781	72	176	0	13
922	Stretch until failure	1-Stretch	60,99	5078	12794	77	189	2	13
923	Stretch until failure	1-Stretch	61,06	5084	12808	83	203	11	9
924	Stretch until failure	1-Stretch	61,13	5090	12823	89	218	8	7
925	Stretch until failure	1-Stretch	61,19	5095	12836	94	231	6	9

Figure C.1: Identify time of starting frame

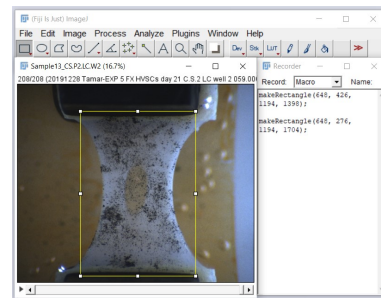
T	SetName	Cycle	Time_S	XSize_um	YSize_um	XDisplacement_um	YDisplacement_um	XForce_mN	YForce_mN	YStrain
994	Stretch until failure	1-Stretch	65,79	5479	13804	478	1199	4	352	0,09
995	Stretch until failure	1-Stretch	65,86	5485	13819	484	1214	11	362	0,09
996	Stretch until failure	1-Stretch	65,93	5491	13834	490	1229	11	375	0,09
997	Stretch until failure	1-Stretch	65,99	5496	13846	495	1241	11	385	0,09
998	Stretch until failure	1-Stretch	66,06	5502	13861	501	1256	6	396	0,09
999	Stretch until failure	1-Stretch	66,13	5508	13876	507	1271	4	410	0,09
1000	Stretch until failure	1-Stretch	66,19	5512	13889	511	1284	6	421	0,09
1001	Stretch until failure	1-Stretch	66,26	5518	13903	517	1298	4	435	0,09
1002	Stretch until failure	1-Stretch	66,33	5524	13918	523	1313	8	450	0,09
1003	Stretch until failure	1-Stretch	66,40	5529	13931	528	1326	13	458	0,10
1004	Stretch until failure	1-Stretch	66,46	5535	13945	534	1340	13	473	0,10
1005	Stretch until failure	1-Stretch	66,53	5541	13960	540	1355	11	485	0,10
1006	Stretch until failure	1-Stretch	66,59	5546	13973	545	1368	6	496	0,10
1007	Stretch until failure	1-Stretch	66,66	5552	13988	551	1383	8	506	0,10
1008	Stretch until failure	1-Stretch	66,73	5558	14002	557	1397	11	525	0,10
1009	Stretch until failure	1-Stretch	66,79	5563	14015	562	1410	6	535	0,10
1010	Stretch until failure	1-Stretch	66,86	5568	14030	567	1425	8	548	0,10
1011	Stretch until failure	1-Stretch	66,93	5574	14044	573	1439	6	558	0,10
1012	Stretch until failure	1-Stretch	66,99	5579	14057	578	1452	6	571	0,10
1013	Stretch until failure	1-Stretch	67,06	5585	14072	584	1467	11	583	0,10
1014	Stretch until failure	1-Stretch	67,13	5591	14087	590	1482	13	598	0,11
1015	Stretch until failure	1-Stretch	67,19	5596	14099	595	1494	11	608	0,11
1016	Stretch until failure	1-Stretch	67,26	5602	14114	601	1509	8	625	0,11
1017	Stretch until failure	1-Stretch	67,33	5608	14129	607	1524	2	641	0,11

Figure C.2: Identify time of physiological frame

Before applying the image filter, a cropping dimension must be selected. Because the tissue and clamp dimensions varied in this study, this had to be selected manually. Automation becomes possible for samples with identical tissue dimensions and image coordinates. The primary qualification for this selection process is the visibility of the entire tissue. Therefore we import a stack of images in ImageJ and open the macro recorder. Draw a box around the entire tissue for the first frame and transport it through the stack until the final frame. Here, the boundaries are extended to include any tissue excluded from the current selection.



(a) Selection in first image



(b) Adjust selection in rupture image

Enter these coordinates into the macro and run it on the file **Sample_13Original**. This will produce a new file with all gaussian images.

Once these are established, the rupture sites and SI boundaries must be identified with respect to the first frame. This can be achieved in two steps. First, the coordinates of the rupture sites are obtained from the end of the stack. Second, the relative deformation between images and the movement of tissue coordinates must be corrected. The easiest way to do this is visually correcting selections by referring to deformations in the speckle pattern. Outline

the point of rupture in the stack and then use the speckle patterns as a guide to correct this back onto the original image. Once this is complete, the SI boundary is also outlined from the reference image.

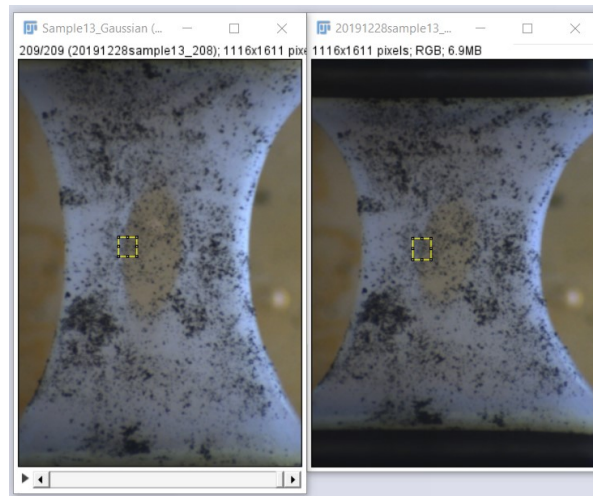
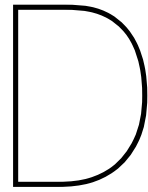


Figure C.4: Select the coordinates and correct their positions by following the speckle patterns.

Finally, remove the images that capture tissue rupture from the image stack and enter all the identified details (dimensions, coordinates, name, etc.) in the Matlab dictionary. After completion of this step, the images are ready to be pre-processed, as is described by appendix B



Ncorr Algorithm

Ncorr [65] is an open-source subset-based DIC program that calculates local 2D strain fields for deforming materials. It employs image registration to process optically visible surface features and uses tracking to monitor their deformation. The relative local deformations are obtained by geometrically relating the material points on the reference (undeformed) image to those in the current (deformed) image. The resulting output are grids that contain local displacement and strain information.

D.1. Working principle

The algorithm of Ncorr is based on the Reliability-Guided DIC (RG-DIC) technique established by Pan et al. (2009) [67]. This technique resolves the errors that propagate from bad points by selecting a seed point, which is used to determine the middle of the reference subset. The reference image is partitioned into groups of neighbouring pixels, called subsets, which collectively form a grid. An example of this is presented in figure D.1. In truth, subsets are a group of circular points at integer pixel locations, whose internal deformation are assumed to be homogeneous. A grid of subsets in the reference frame serves as a template from which the correlation between images is derived.

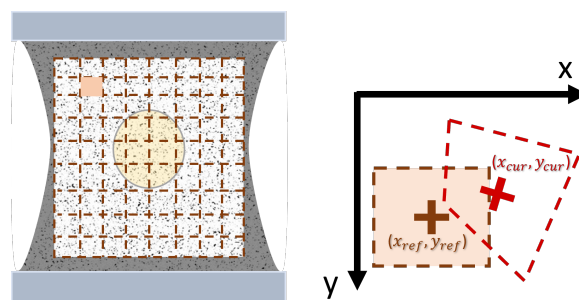


Figure D.1: The Region Of Interest (ROI) is divided into subsets. The relative movements of these subsets are used to obtain the local strains

Following the example, an initial point (x_{ref_i}, y_{ref_j}) in the reference frame is deformed to a new coordinate in the current frame (x_{cur_i}, y_{cur_j}) . The center of the reference subset is denoted by the coordinates x_{ref_c}, y_{ref_c} , while the annotation rc indicates the transformation of the reference to current subset. The indices (i,j) have a dual purpose, establishing a correspondence between the current and reference subsets points and indicating the relative location

of all points with respect to the centre of the subset. The following equation describes the deformation of the coordinates:

$$\begin{aligned} x_{cur_i} &= x_{ref_i} + u_{rc} + \frac{\partial u}{\partial x_{rc}} \Delta x_{ref} + \frac{\partial u}{\partial y_{rc}} \Delta y_{ref} \\ y_{cur_j} &= y_{ref_j} + u_{rc} + \frac{\partial v}{\partial x_{rc}} \Delta x_{ref} + \frac{\partial v}{\partial y_{rc}} \Delta y_{ref} \end{aligned} \quad (D.1)$$

Here, the distance between the initial reference subset points and the coordinates of the initial reference subset center is indicated by δx_{ref} and δy_{ref} .

$$\begin{aligned} \Delta x_{ref} &= x_{ref_i} - x_{ref_c} \\ \Delta y_{ref} &= y_{ref_i} - y_{ref_c} \end{aligned} \quad (D.2)$$

A new position is estimated by finding an initial guess at integer locations and determining the agreement with a cost function. The *seed* point is the first point selected by the user and is the only one to use a normalised cross-correlation function (NCC) to obtain an initial guess. This metric indicates a good match between the subset points when the C_{NCC} is close to 1. The term S represents the set that contains all subset points.

$$C_{NCC} = \frac{\sum_{(i,j) \in S} (f(\tilde{x}_{ref_i}, \tilde{y}_{ref_j}) - f_m)(g(\tilde{x}_{cur_i}, \tilde{y}_{cur_j}) - g_m)}{\sqrt{\sum_{(i,j) \in S} [f(\tilde{x}_{ref_i}, \tilde{y}_{ref_j}) - f_m]^2 \sum_{(i,j) \in S} [g(\tilde{x}_{cur_i}, \tilde{y}_{cur_j}) - g_m]^2}} \quad (D.3)$$

The grayscale values at the reference and deformed subset points are indicated by f and g . The corresponding averages are denoted by f_m and g_m , while $n(S)$ is number of points in S .

$$\begin{aligned} f_m &= \frac{\sum_{(i,j) \in S} f(\tilde{x}_{ref_i}, \tilde{y}_{ref_j})}{n(S)} \\ g_m &= \frac{\sum_{(i,j) \in S} g(\tilde{x}_{cur_i}, \tilde{y}_{cur_j})}{n(S)} \end{aligned} \quad (D.4)$$

The displacement matrix, P_g , corresponds to this first guess follows the structure in equation D.4, and undergoes iterative optimisation of P_r to refine its solution.

$$\begin{aligned} \Delta P_g &= u^{(g)}, v^{(g)}, 0, 0, 0, 0 \\ \Delta P_r &= u, v, \frac{\partial u}{\partial x'}, \frac{\partial u}{\partial y'}, \frac{\partial v}{\partial x'}, \frac{\partial v}{\partial y'} \end{aligned} \quad (D.5)$$

A non linear optimiser, which is defined by either the Inverse Compositional Gauss-Newton (IC-GN) method, seeks the roots of the Least Square correlation coefficient (C_{LS}). It uses its neighbors to minimize C_{LS} and allows for the calculation of subset rotations and strains. This function indicates a good agreement subsets when close to 0.

$$C_{LS} = \frac{\sum_{(i,j) \in S} (f(\tilde{x}_{ref_i}, \tilde{y}_{ref_j}) - f_m)}{\sqrt{\sum_{(i,j) \in S} [f(\tilde{x}_{ref_i}, \tilde{y}_{ref_j}) - f_m]^2}} - \frac{\sum_{(i,j) \in S} (g(\tilde{x}_{cur_i}, \tilde{y}_{cur_j}) - g_m)}{\sqrt{\sum_{(i,j) \in S} [g(\tilde{x}_{cur_i}, \tilde{y}_{cur_j}) - g_m]^2}} \quad (D.6)$$

D.2. Program execution

The execution of Ncorr is described in detail on the website , but its key steps are summarised below. Ensure that the 'OpenMP multithreading' is checked during the installation and the maximal number of cores available to the system for computation. Because the calculation of the strain fields is very complex, the analysis of a single sample can take from several hours to days, depending on the device's computational power.

D.2.1. Uploading relevant files on Ncorr

The program is initiated through the function '`handles_ncorr = ncorr`', following which a pop-up appears requiring the setup of a path.

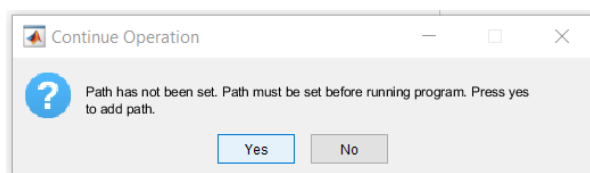


Figure D.2: Setting up a path for the Ncorr GUI

The Ncorr interface appears as is presented in figure D.3, with on the left-hand side a working tree indicating the program state. If a step has not been fulfilled, it is followed by **NOT SET**. To complete the steps, the user must follow the workflow from top to bottom and change the status of each state to **SET**.

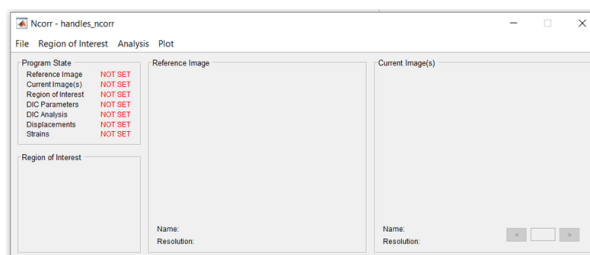


Figure D.3: Overview of startup Ncorr GUI

First, the images (.jpg, .tif, .png, .bmp) must be fed into the program. The file name must terminate in the number corresponding to its position in the image stack. The reference image corresponds to the single first image in the stack. It can be uploaded through *File > Load > Reference image*. The current image(s) refers to the remaining images in the stack, which may be uploaded through the memory-friendly *Load lazy* method. As is shown in the figure, this is achieved by *File > Load Current Image(s) > Load Lazy (slower but less memory)*.

As mentioned in this report's main body, a binary image is required to isolate the region of interest in the tissue. As this project uses a forward analysis, a single ROI is required for this step. By following *Region of Interest > Set Reference ROI* The ROI can be either drawn in real-time or uploaded from a preexisting file.

Once all the images are uploaded, three of the seven steps will be completed.

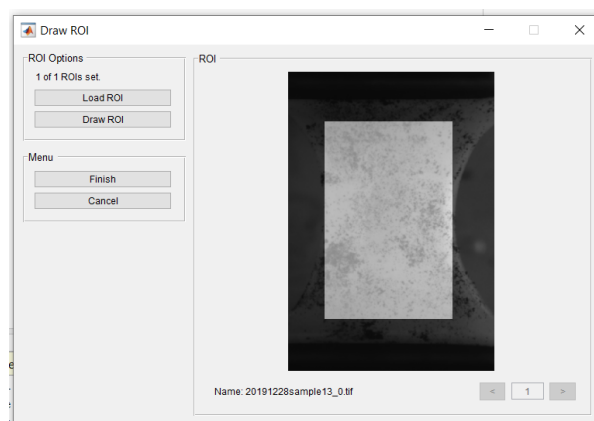


Figure D.4: To select the current images, use the Load Lazy approach to call images to the program. This important for large image stacks.

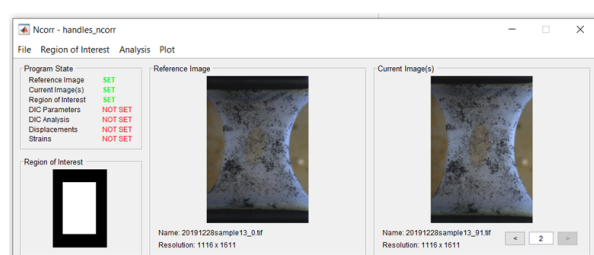


Figure D.5: First three steps are completed, and their data is visible in the GUI

D.2.2. Parameters

The first set of parameters required are relevant for DIC itself (*Analysis > Set DIC Parameters*). The ROI will be diced into a grid of circular subsets whose size should be small enough to provide good spatial resolution without introducing noise into the system. Furthermore, a spacing parameter is decided to reduce computational costs. This is influenced by the image resolution, as it defines the number of points used in a subset. All required parameters are presented in figure D.6.

Next, the step 'DIC Analysis' is addressed by selecting *analysis > Perform DIC analysis* and selecting the seeds. The amount is equivalent to the number of cores entered during the previous multithreading option. The points are selected as symmetric as possible, adhering to the rules identified in the Ncorr Instruction Manual.

A preview window appears after confirming the seed points, communicating the identified correlation between the different images. Aside from the visual presentation of the selected points, several variables summarise the quality of seed placement. The *Number of Gaussian iterations* and the *Correlation Coefficient* are familiar entities, as they were described in the selection of an image processing technique. Respectively, they describe the computational power and quality of agreement to identify relatable subsets.

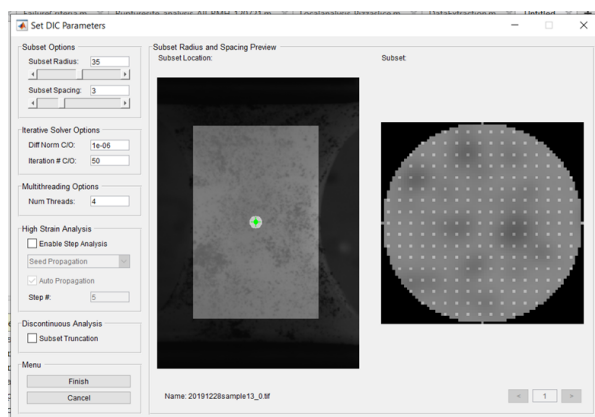


Figure D.6: The optimal parameters for DIC on the tissue constructs are a subset radius of 35 and a spacing of 3

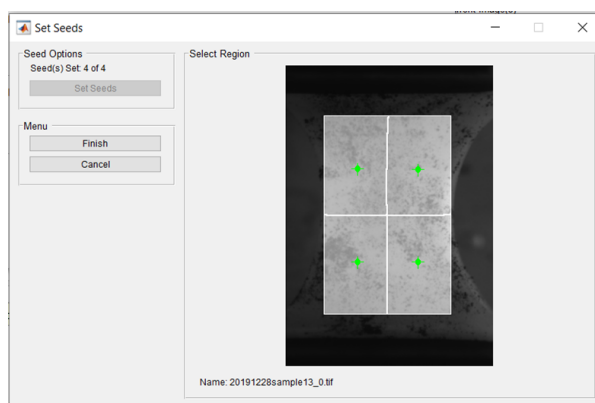


Figure D.7: Selecting seed points. They should be equally spaced, to divide the region up into equal portions. Most importantly, they must not move out of ROI.

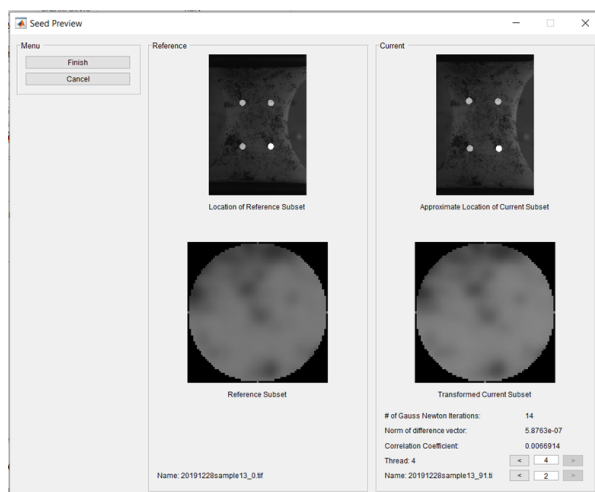


Figure D.8: Seed preview. Here the user can validate the performance of the program. The seed must not move outside the ROI and must converge, as is indicated by the iterations (max of 50) and correlation coefficient.

D.2.3. Obtaining data fields

Once DIC analysis has come to completion, it is possible to format the displacement points based on the subset C_{LS} value. This step is initiated by selecting *Analysis > Format Displacements*. After entering the scale (0.0093 mm/pixel) and selecting a cutoff for the correlation coefficient (0.7), the displacements were calculated.

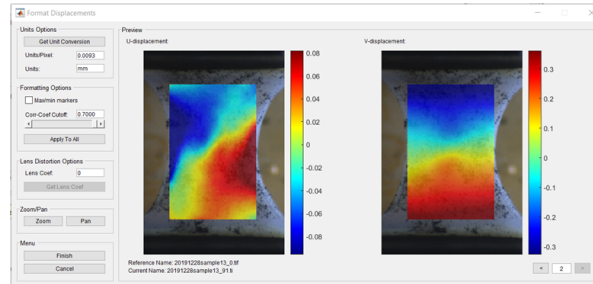


Figure D.9: The displacements are formatted by scaling the image to 0.0093 mm/pixel with a cutoff of 0.7 for the correlation coefficient.

Finally, the strain maps were calculated for the formatted displacements. By selecting *Analysis > Calculate Strains*, a window similar to figure D.10 appears. The strain radius was selected to be 5, allowing for minimal smoothing and maximal expression of local features. Smaller radii produce artefacts from unreliable calculations, while larger radii result in over-smoothing and a loss of resolution. Because we want a maximal consistency between the images, it is important to include a maximal amount of elements in the calculations of the strains- a condition that is appeased by a strain radius of 5.

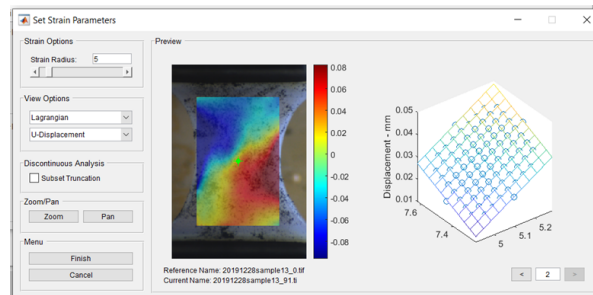


Figure D.10: The Lagrangian strains are calculated with a radius of 5. These points fit the plane in the Least Squares fit.

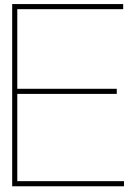
D.3. Optimising DIC

Correct speckle application can already largely improve the image quality. This is dictated by three constraints: non-repetitiveness, isotropic and high contrast. The speckle density should be approximately 50%, where half of the tissue is covered by speckles and the other half is not. This is achieved by applying a random but uniformly distributed pattern of equally sized speckles. The speckles should lie between 3 x 3 to 7 x 7 pixels to prevent aliasing and overly dense speckle populations. According to the dimensions of the tissue engineered samples included in the report, this corresponds to 15 to 34 microns per speckle.

$$\text{Size per speckle} = \frac{\text{tissue length}}{2048 \text{ px}} * [3 \text{ to } 7 \text{ px per speckle}]$$

The equipment used to capture the images and their cleaning protocol also play a determining role in image quality. The most suitable cameras for this application have a black and white lens, with low noise, high quantum efficiency and a high dynamic range (maximal signal-to-noise ratio). Colour capture is unnecessary for DIC images and may give rise to artefacts [68]. Lens distortion may also be a source of inaccuracies and should therefore be minimal, despite any compensation strategies offered by the DIC program. Another criteria that must be carefully controlled is lighting. Correct lighting must perpendicularly illuminate the sample without oversaturating pixels or heating tissue. Finally, camera dust may hinder experimentation, motivating the need for camera maintenance. Poor cleaning regimes can be directly responsible for incorrect DIC.

This study has identified two metrics that define image quality. These are calculated by the DIC program during *seed preview*. *Seeds* are the initial guess point of DIC, used to detect local deformation parameters, independent from its neighbours. After setting the seeds, the DIC program outputs values for the image quality metrics. The first metric is the correlation coefficient, which quantitatively indicates the similarity between the reference and current images. It follows a least-squares criterion and indicates a good match when the value is close to zero. Therefore, it is beneficial to make this metric as small as possible. The second metric is the number of Gaussian-Newton iterations needed for seed convergence. The faster the seed converges, the quicker the program works. Hence, a high amount of iterations indicates that the operation is computationally expensive or that seed placement is incorrect. This metric must also stay as small as possible and has a cut off at 50 iterations.



All strain fields

The strain fields of all samples are summarised in this chapter. Two time points of main interest are looked at: the physiological time point and the final time point. As has been mentioned in the report, the physiological time point corresponds to 10% of the global strain. This selection is not specific to localised strain, but the tissue as a whole. Therefore, in this frame we would observe tissue responses that would be expected in vivo. The final frame is the last frame before rupture ensues. This frame corresponds to the ultimate tension that can be withstood by the sample.

E.1. Cartesian coordinate system

E.1.1. Marked local strain fields in final frame

Table E.1: Strain fields before SI rupture.

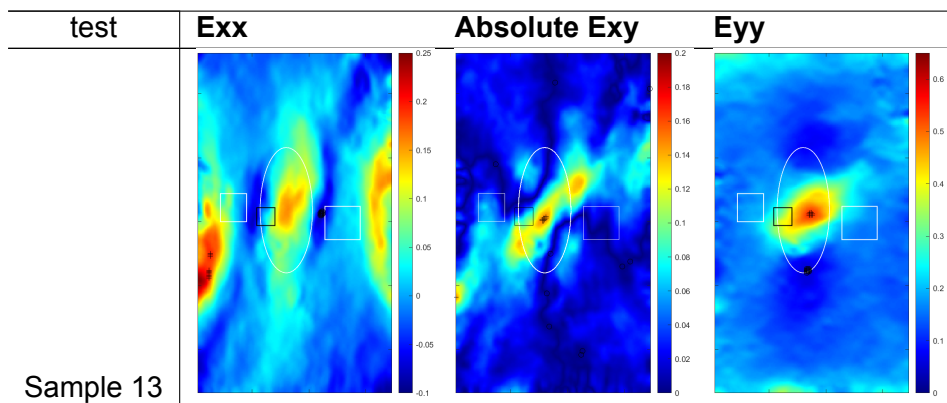
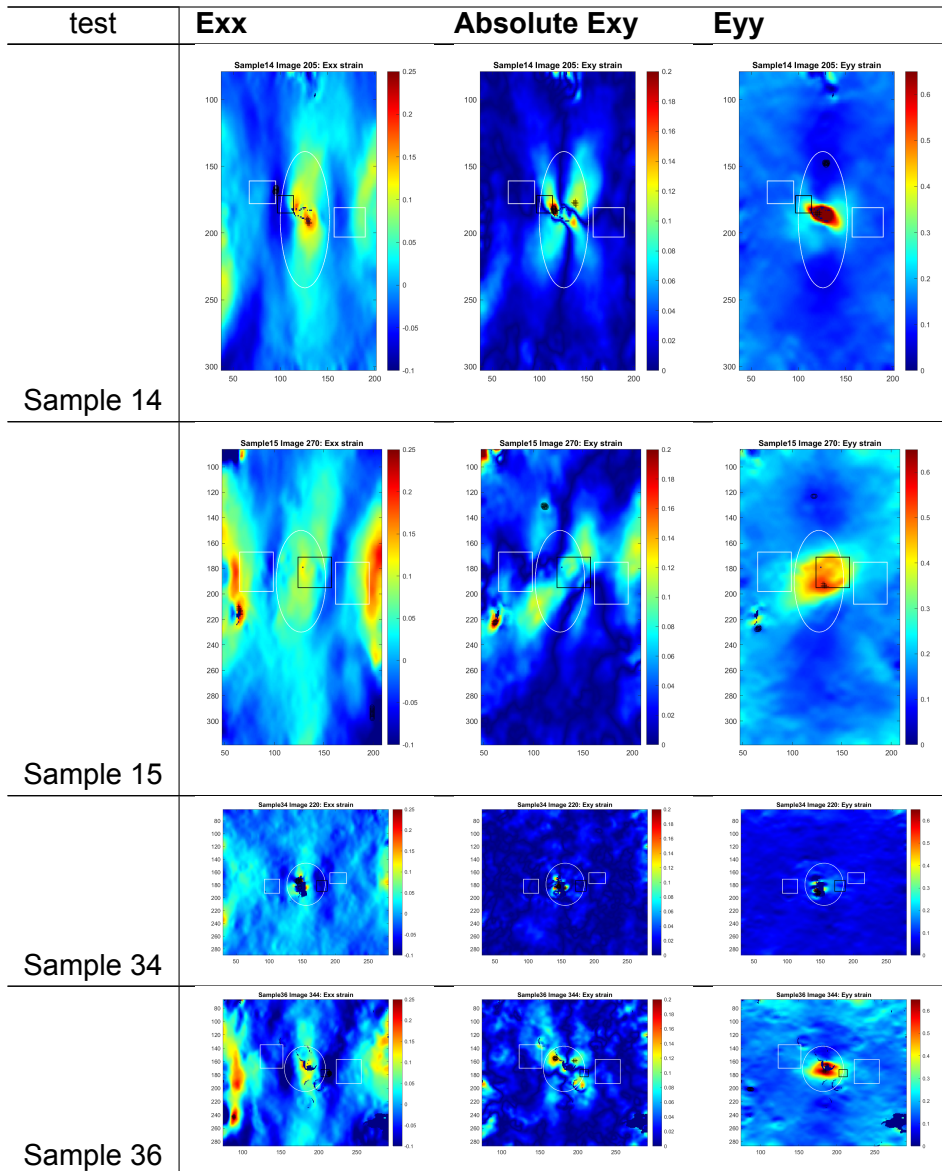
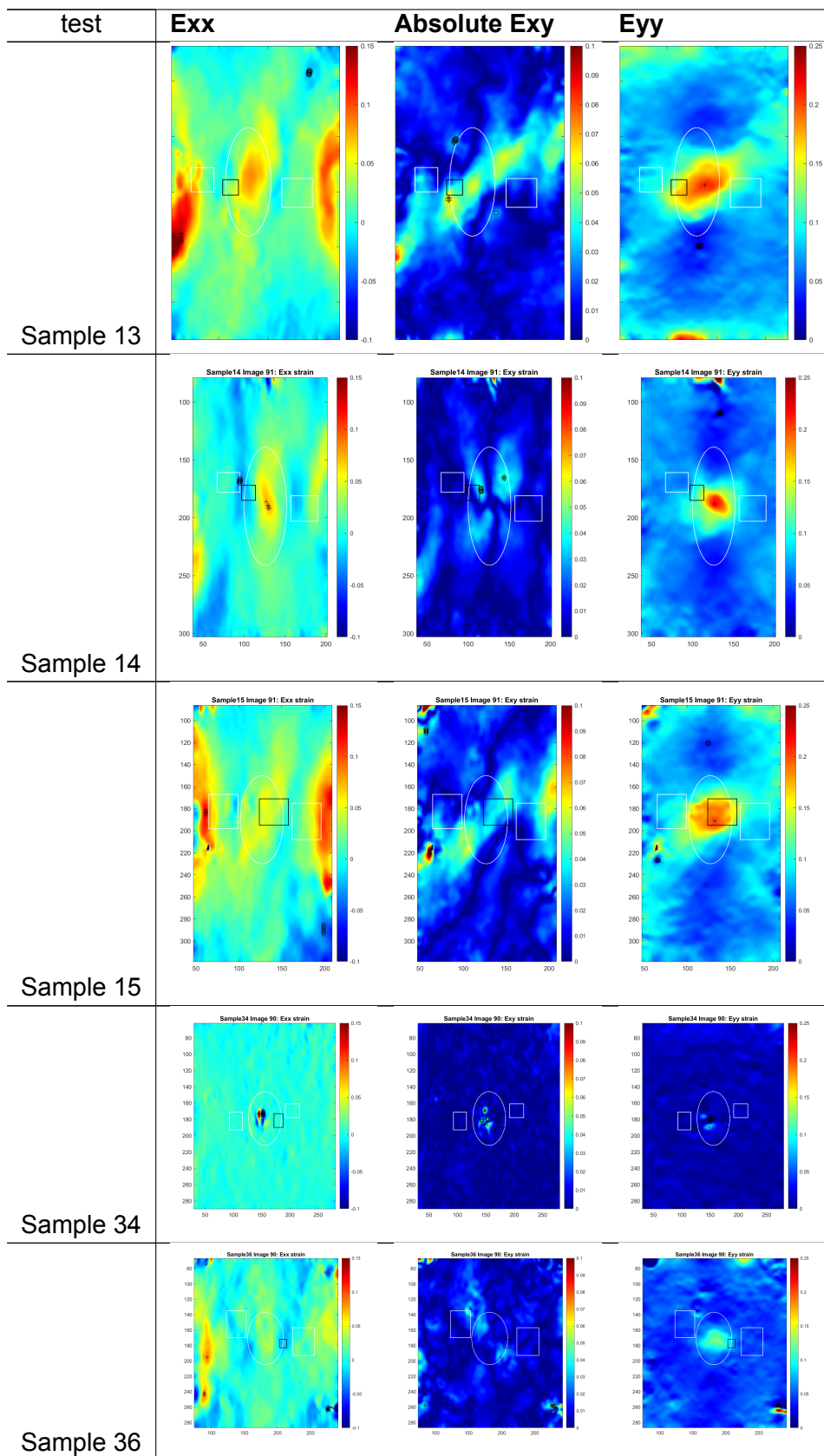


Table E.1: Strain fields before SI rupture.



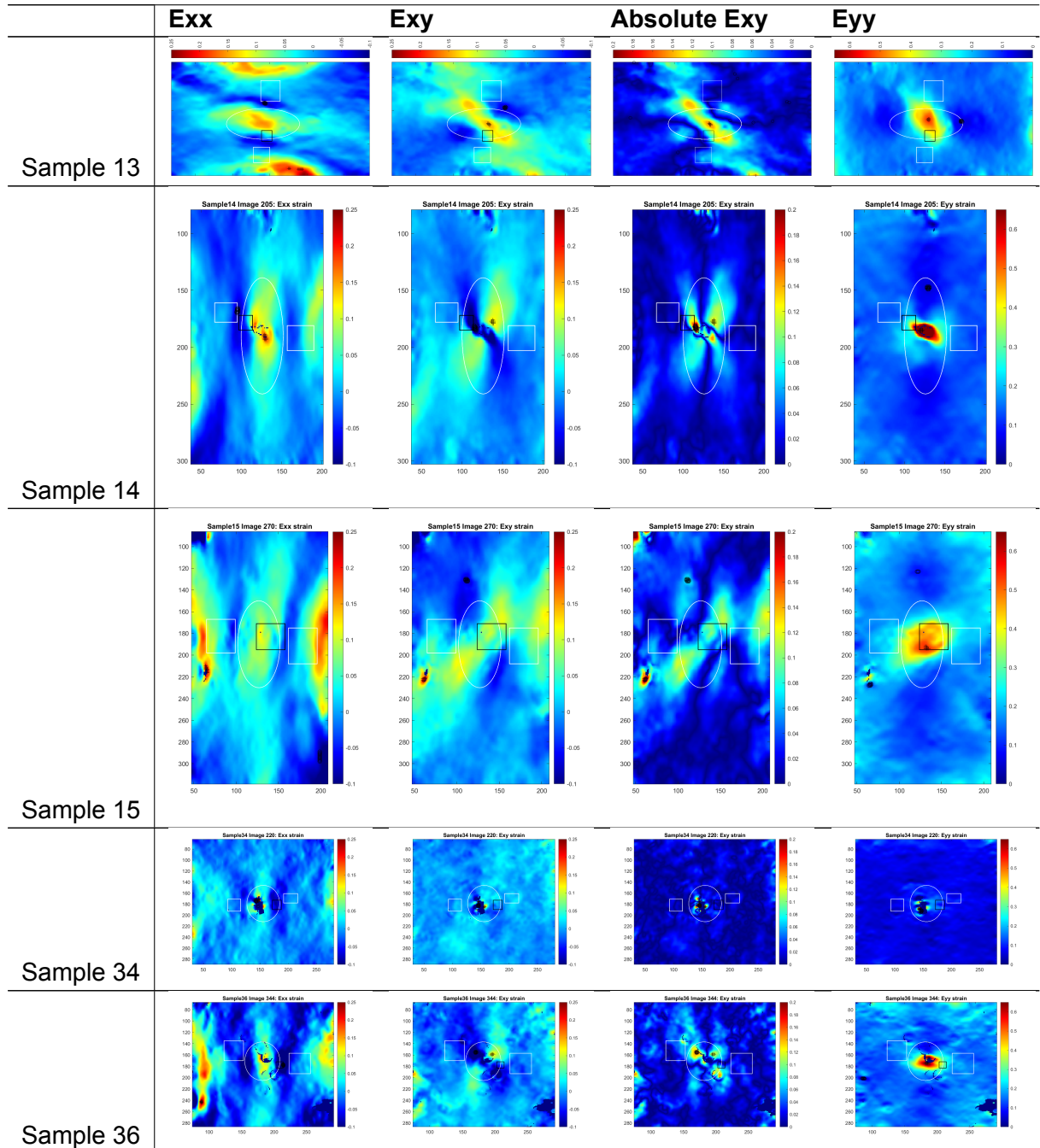
E.1.2. Marked local strain fields in the physiological frame

Table E.2: Strain fields at physiological frame.



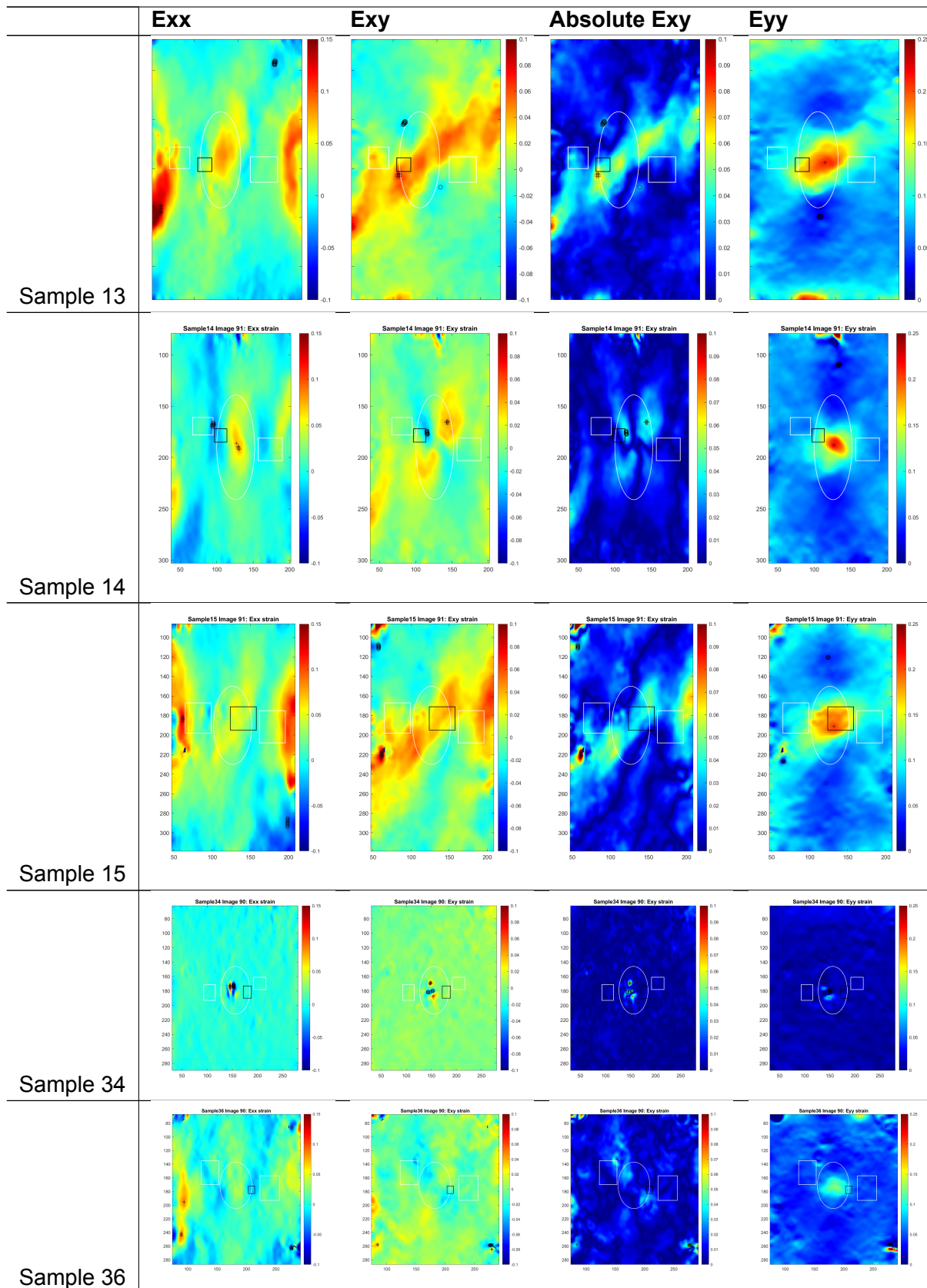
E.1.3. Maxima of local strain fields in final frame

Table E.3: Strain fields before SI rupture.



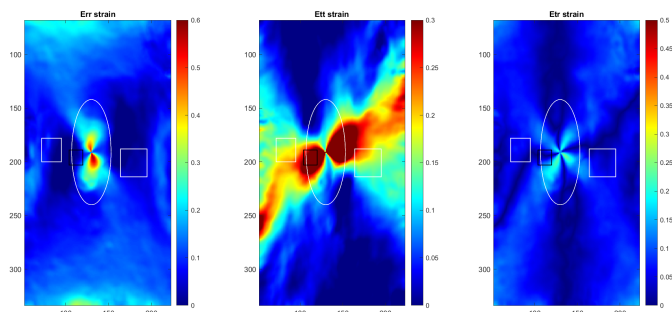
E.1.4. Maxima of local strain fields in physiological frame

Table E.4: Strain fields before SI rupture.

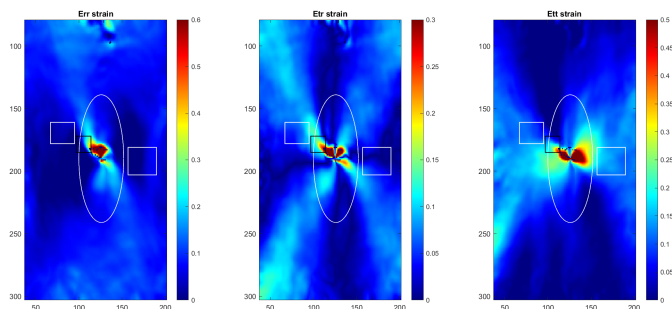


E.2. Polar coordinate system

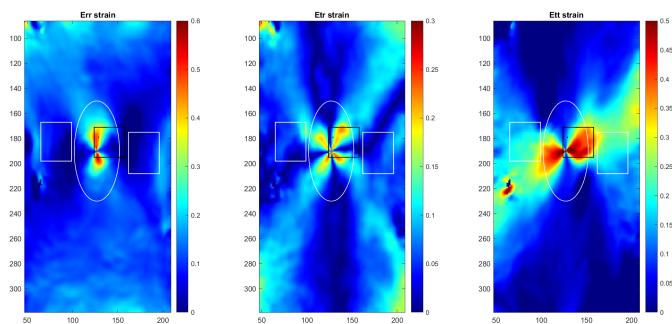
E.2.1. Marked local strain fields in the final frame



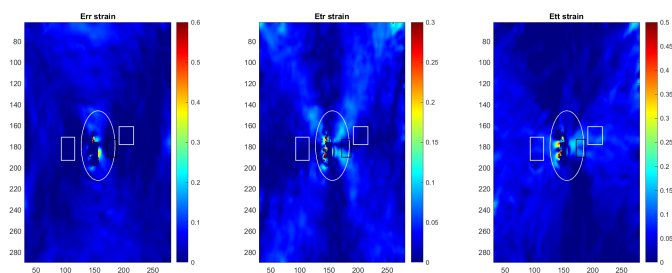
(a) Sample 13



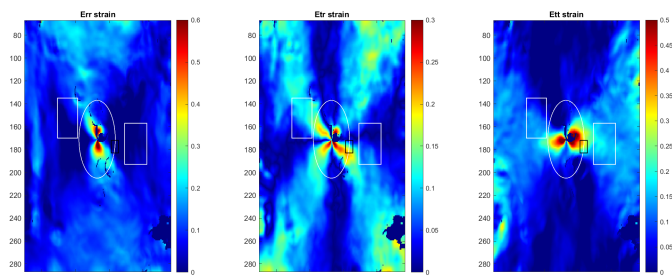
(b) Sample 14



(c) Sample 15



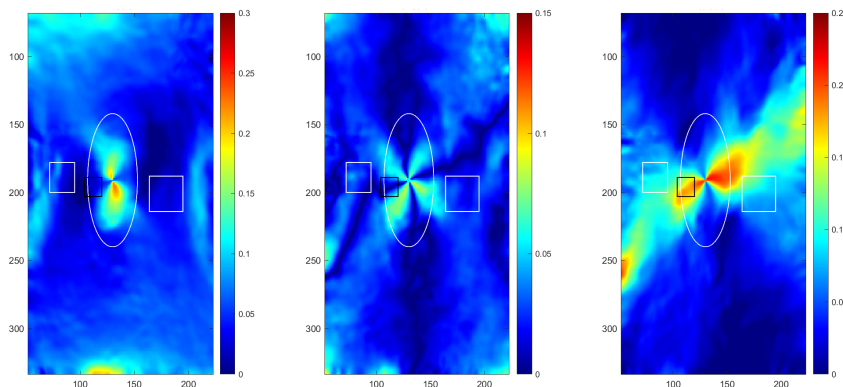
(d) Sample 34



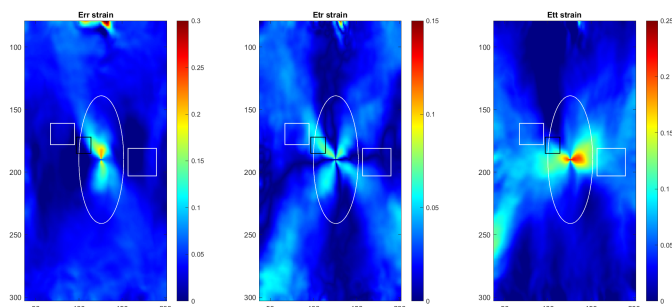
(e) Sample 36

Figure E.1: Exx, Exy and Eyy strains converted into circular polar strains.

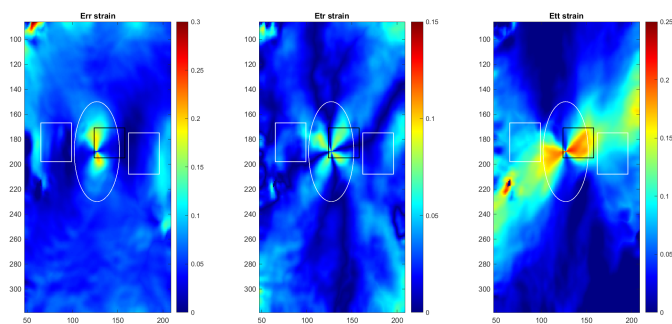
E.2.2. Marked local strain field at a physiological frame



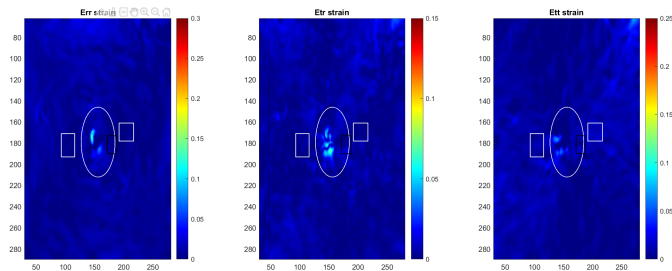
(a) Sample 13



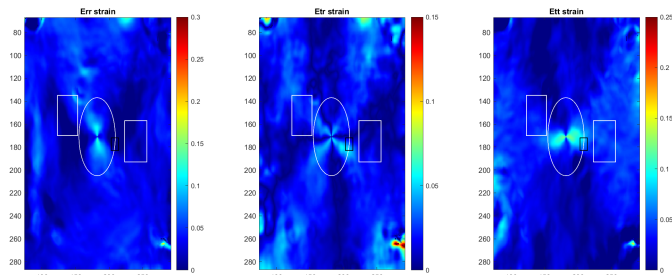
(b) Sample 14



(c) Sample 15



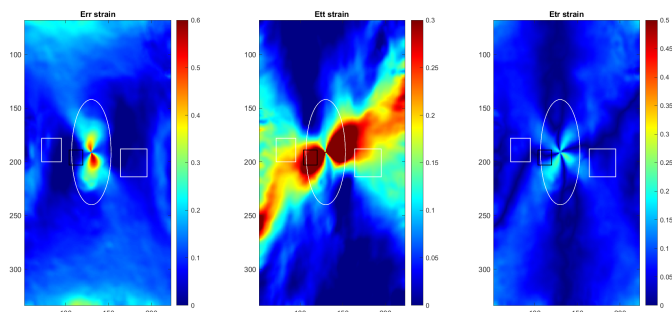
(d) Sample 34



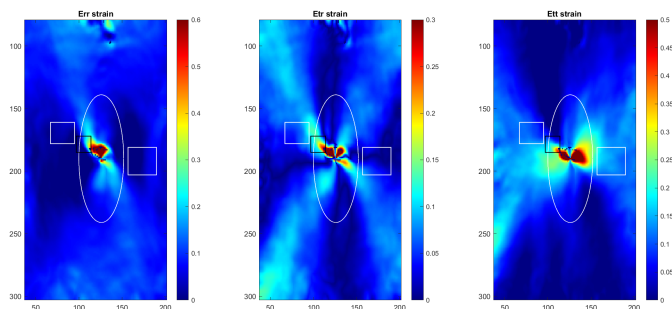
(e) Sample 36

Figure E.2: Exx, Exy and Eyy strains converted into circular polar strains.

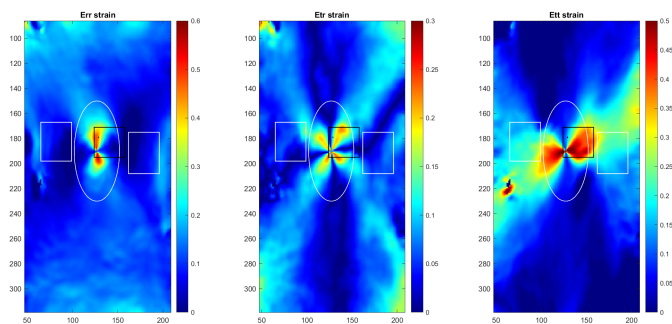
E.2.3. Maxima of local strain fields in final frame



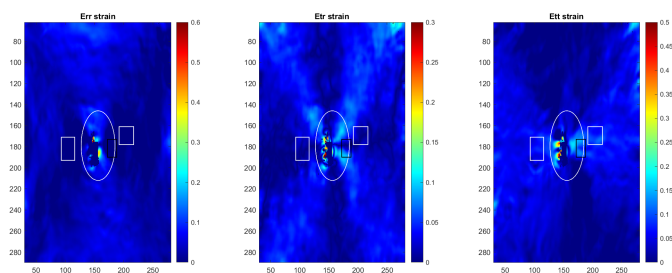
(a) Sample 13



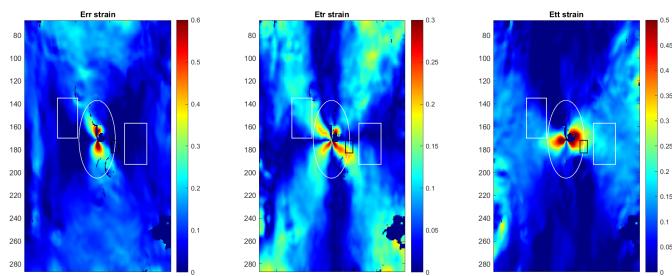
(b) Sample 14



(c) Sample 15



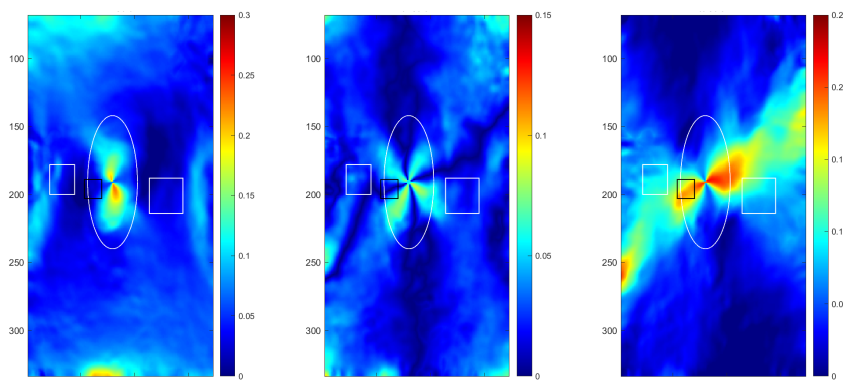
(d) Sample 34



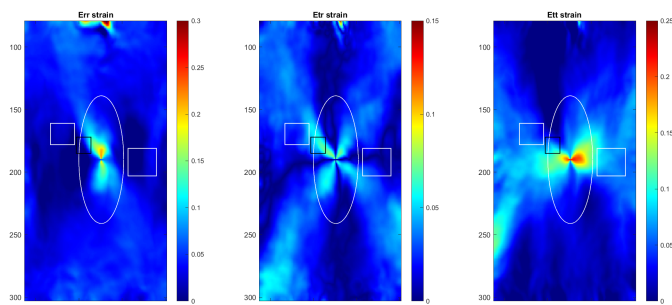
(e) Sample 36

Figure E.3: Exx, Exy and Eyy strains converted into circular polar strains.

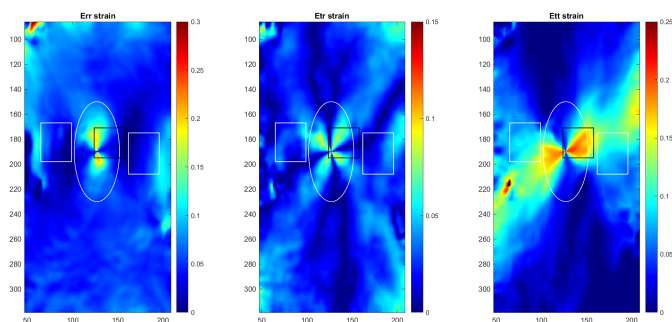
E.2.4. Maxima of local strain rates in the physiological frame.



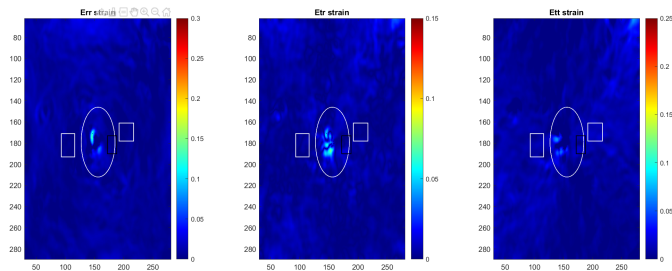
(a) Sample 13



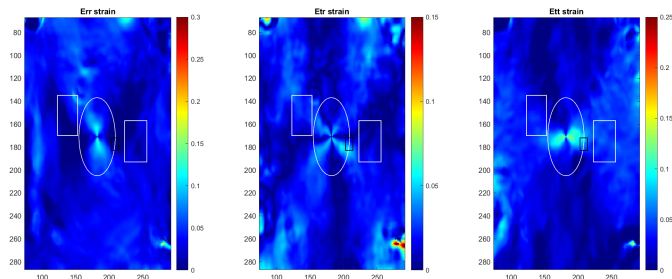
(b) Sample 14



(c) Sample 15



(d) Sample 34



(e) Sample 36

Figure E.4: Exx, Exy and Eyy strains converted into circular polar strains.

Local strain maxima in the full tissue construct

This appendix discusses data extracted from tissue regions identified by figure F.1.

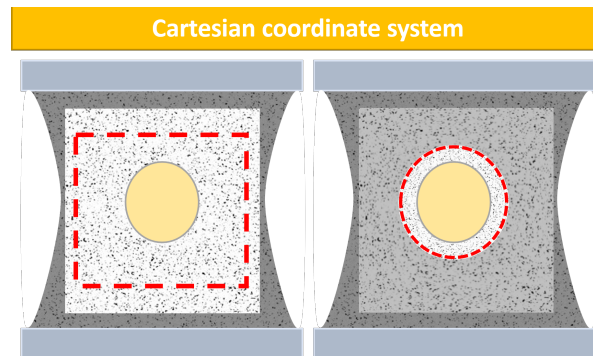


Figure F.1: Full and zoomed tissue perspectives. The red boundaries highlight from where the local maxima are considered.

The ten maxima and minima are highlighted in each strain map of figure F.2 by the symbols '+' and 'o', respectively. The approximate dimensions of the ROI are 8.1 mm by 8.2 mm. No points are identified along the edges of the maps because of the restrictive boundary condition used in the extraction of ultimate strain points (see appendix E).

The local ε_{xx} maxima are concentrated at the left tissue edge while the local minima lie right of the SI. The maxima (average magnitude of 0.3) lie 2.3 mm from the SI rupture box. The minima (average magnitude of -0.1) lie closer to this box, with less than 2 mm separating them. The comparison with other samples shows that these distances vary significantly, with a standard deviation of ± 1.5 mm.

The ε_{xy} maxima lie in the centre of the SI, less than a millimetre away from the centre of the black rupture box. It reaches a magnitude of 0.15, which is slightly lower than the maximal ε_{xx} strain. Because the map shows absolute strains, there are no minima. The location of these maxima differs per sample, where three of the five samples find them inside the SI. Figure F.3 shows that these maxima perform second best at approaching the rupture site. However, the corresponding standard deviation of 1 mm shows that this performance is sample dependent.

The maximal ε_{yy} strain in the figure F.2c reaches 0.54, which is more than twice the magnitudes found in the ε_{xx} and ε_{xy} distributions. These maxima show the most consistency in

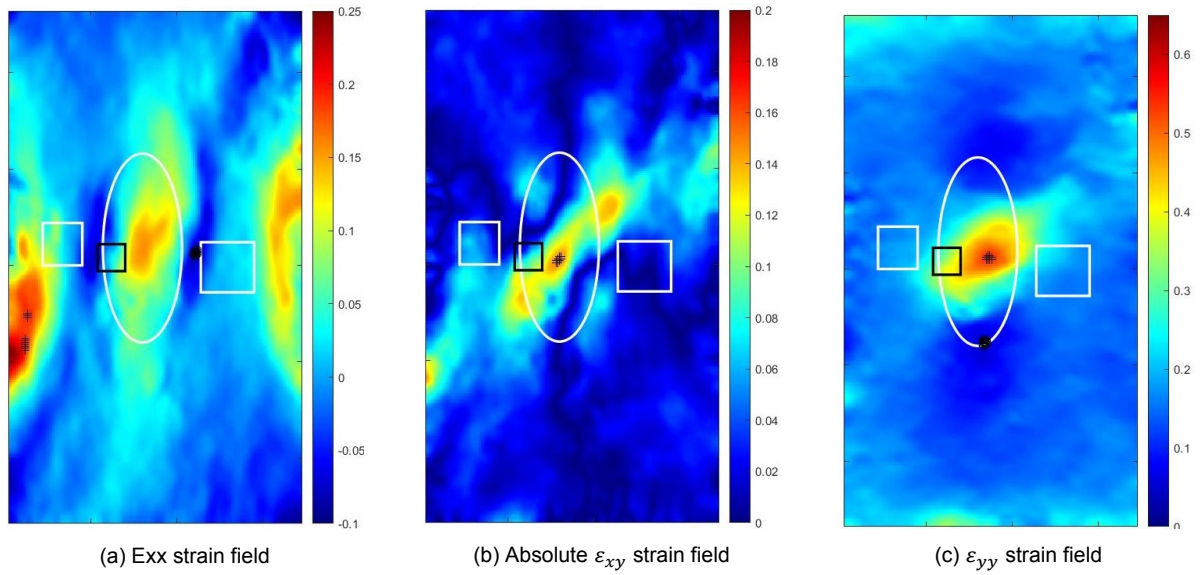


Figure F.2: Strain field maps before SI rupture, with maximal strain points highlighted by '+' and minimal strain points by 'o'. The black and white rectangles correspond to the SI and fibrous tissue rupture sites, while the white ellipse represents the location and shape of the SI.

their approximation of the SI rupture box. This is because, throughout all samples, the maxima lie in the centre of the SI. This consistency is reflected by figure F.3, where the ε_{yy} maxima show the least variation (± 0.3 mm) of all strains. The minima consistently lie at the periphery of the SI, which is on average 1.8 mm from the SI rupture box.

Figure F.4a summarises the distances described for all samples.

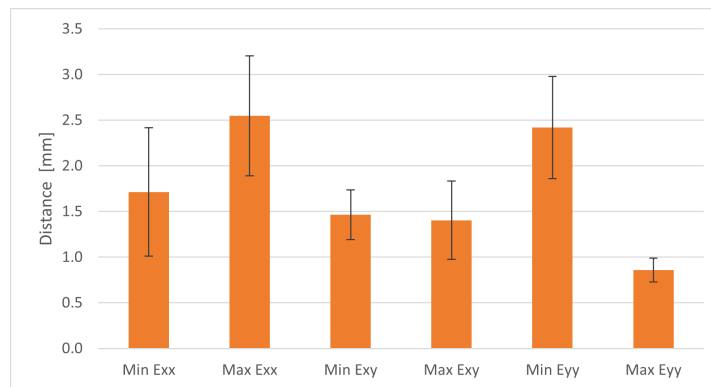
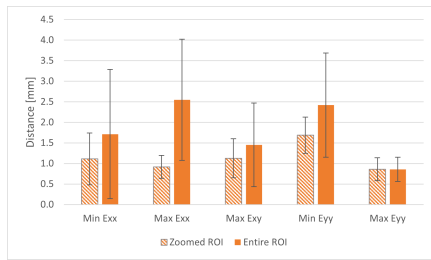


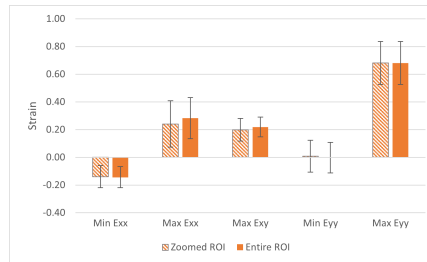
Figure F.3: Average distance (in mm) between SI rupture box and maxima and minima. The error bars indicate the standard deviation between all samples.

The locations of ε_{xy} and ε_{yy} minima and maxima are unchanged from the zoomed perspective of the entire tissue construct, which implies that the distances and magnitudes are the same. Therefore, the observations made for the entire ROI hold for the given sample.

The effect of ROI size reduction is most prominent when looking at the distances of all samples collectively. This is presented in figure F.4a, where the average distances to the minima and maxima of all strains are significantly different. The ε_{xx} maxima show the greatest average change in their positions. Reducing by 64%, they estimate an average distance of 0.9 ± 0.3 mm to the centre of the SI rupture box. A minor change between the two perspectives is found at the position of the ε_{yy} maxima, which are separated from the box by the same



(a) Comparison of distances between SI rupture box and local maxima and minima, in the entire ROI and Zoomed SI. The error bars indicate the standard deviation across all five samples.



(b) Comparison of the local strain maxima and minima found in the entire ROI and Zoomed SI. The error bars indicate the standard deviation across all five samples.

distance as the ε_{xx} maxima.

Interestingly, the magnitudes of all minima and maxima are highly similar in both perspectives. For the ε_{yy} maxima, this indicates that the entire ROI identifies the same maxima as the zoomed ROI. However, changes in displacement found for other minima and maxima are a consequence of multiple strain modes of similar calibre. Hence, the estimation of distances is highly susceptible to strain heterogeneity Figure F.4b summarises the average strains magnitudes found throughout all samples.



Different coordinate systems

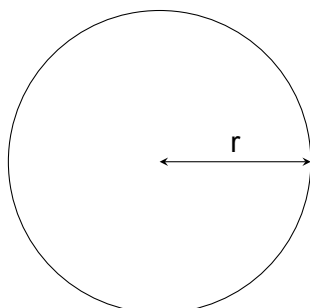
The local strain patterns were analysed with respect to two coordinate systems: the global and the polar coordinate systems.

Global coordinate system

The global coordinate system corresponds to the previously defined two-dimensional system in figure 2.3. The y-direction lies along the tensile direction, which is depicted here as the vertical axis. The x-direction lies perpendicular to the y-direction, observed along the horizontal axis.

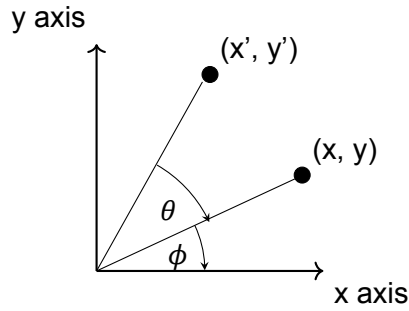
G.0.1. Polar coordinates

The polar coordinate system is a circular orientation of the global coordinate system. These perpendicularly intersect a circular SI. The first step requires the transformation of the global cartesian coordinates to polar coordinates. The formulas that describe the relationship are as follows:



$$\begin{aligned}x &= r \cos \phi \\y &= r \sin \phi \\r &= \sqrt{x^2 + y^2} \\ \phi &= \arctan \frac{y}{x}\end{aligned} \quad (\text{G.1})$$

Here, x and y are the Cartesian axes, r is the radius of the circle, and ϕ is the angular orientation. Rotation of the object about the origin by θ degrees results in the shown x' and y' , whose Cartesian equation is as following:



$$\begin{aligned}
 x' &= r \cos \theta + \phi \\
 &= r \cos \theta \cos \phi - r \sin \theta \sin \phi \\
 &= x \cos \theta - y \sin \theta \\
 y' &= r \sin \theta + \phi \\
 &= r \sin \theta \cos \phi + r \sin \phi \cos \theta \\
 &= x \sin \theta + y \cos \theta
 \end{aligned} \tag{G.2}$$

The transformation of the Cartesian coordinates into the rotated coordinates is governed by the following rotational matrix.

$$\begin{bmatrix} x' \\ y' \end{bmatrix} = \begin{bmatrix} \cos \theta & -\sin \theta \\ \sin \theta & \cos \theta \end{bmatrix} \begin{bmatrix} x \\ y \end{bmatrix} \tag{G.3}$$

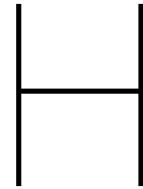
Accordingly, the tensors of the strain maps in the cartesian coordinates may be transformed towards a circular polar coordinate by the following rule:

$$\varepsilon_{polar} = R^T(\theta) \cdot \varepsilon_{Cartesian} \cdot R(\theta) \tag{G.4}$$

A correct origin must be selected prior to the matrix transformation described by equation G.4. All rotations occur about this point, and therefore the desired location must be carefully selected. For the given tissues, the coordinate system is translated such that the point of origin lies at the centre of the SI. Here the distance to the fibrous tissue is symmetric along the global x and y-axis, which is reflected in much of the tissue behaviour. Although the rotational matrix assumes circularity, which does not agree with the elliptical shape of the SI, an approximation of the polar strain field is regarded as a good product for observational conclusions. The rotated strains are extracted by the following equation, which combine the results of equations G.3 and G.4.

$$\begin{bmatrix} \varepsilon_{rr} & \varepsilon_{r\theta} \\ \varepsilon_{\theta r} & \varepsilon_{\theta\theta} \end{bmatrix} = \begin{bmatrix} \cos \theta & \sin \theta \\ -\sin \theta & \cos \theta \end{bmatrix} \begin{bmatrix} \varepsilon_{xx} & \varepsilon_{xy} \\ \varepsilon_{yx} & \varepsilon_{yy} \end{bmatrix} \begin{bmatrix} \cos \theta & -\sin \theta \\ \sin \theta & \cos \theta \end{bmatrix} \tag{G.5}$$

Because ε_{yx} is an empty entity, only ε_{rr} , $\varepsilon_{r\theta}$ and $\varepsilon_{\theta\theta}$ matrixes are produced.



Segmentation

The circumferential length of an ellipse can be calculated by the following equations, where R_x and R_y are the radii in the x and y directions.

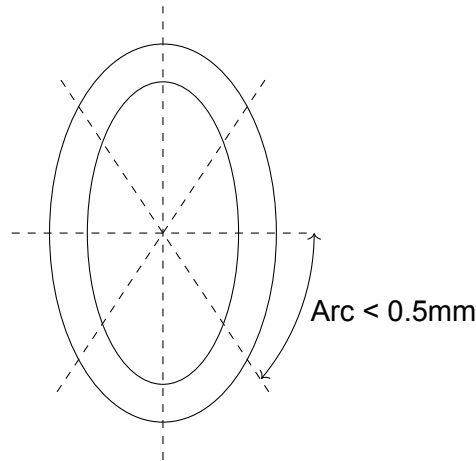
$$h = \frac{(R_x - R_y)^2}{(R_x + R_y)^2} \quad (\text{H.1})$$
$$Perimeter \approx \pi(R_x + R_y) \left(1 + \frac{3h}{10 + \sqrt{4 - 3h}} \right)$$

Following the guideline of ultrasound resolution, a criterion was set for the minimal allowed arc length. The criterion that corresponded to each slice was 0.5 mm. This was decided based on the values reported in literature, including IVUS, which have a radial resolution of 0.2 mm [23]. Division of the ellipse occurs by powers of two, where the amount of new segments are constantly doubled. By calculating the arc length following each division, the maximal amount of segments can be deduced.

The given distances are calculated by dividing the circumferential length by the number of sections. Adhering to the 0.5 mm threshold, four versions of segmentation can be conducted for all the data.

Table H.1: The arc lengths corresponding to different amounts of segmentation

	Amount of segments	Arc length
2^1	2	6.40 mm
2^2	4	3.20 mm
2^3	8	1.60 mm
2^4	16	0.80 mm



An additional level in the segmentation process is the angle at which the sections are derived. By encoding a rotational variable, partitioning the samples at different angles is possible. This result is that the segmentation can be oriented to isolate the point of rupture perfectly. Following this definition of partitioning, the written Matlab code allows for rotation relative to the global axis system. This objective is achieved by the following plastic definition of angular boundaries. Noting that a full revolution about the origin requires 2π , symmetric adjustments to the ultimate angles create different starting points.

$$\theta_i = (i - 1) \frac{2\pi}{\#segments} + \phi_{rotation}, i \frac{2\pi}{\#segments} + \phi_{rotation} \quad (\text{H.2})$$

Here, i is the segment number, θ_i is the starting angle of the corresponding segment number, and $\phi_{rotation}$ is the angular offset. To find the new boundaries of the segments, the angular offset can be entered into the final formula.

$$X_{segment} = R_x \cos(\theta_i) + X_{center}; Y_{segment} = R_y \sin(\theta_i) + Y_{center}; \quad (\text{H.3})$$

Polar Strains

I.1. Patterns analysis and rupture

I.1.1. Polar strains

The ε_{rr} , $\varepsilon_{\theta r}$ and $\varepsilon_{\theta\theta}$ strain maps are presented in figure I.1. As is mathematically described in appendix G, the ε_{rr} and $\varepsilon_{\theta\theta}$ match their Cartesian counterpart where θ is a multiple of π . Moreover, these distributions match the predicted response. For example, the highest radial strains occur when the polar orientation of the subsets is aligned to the vertical direction.

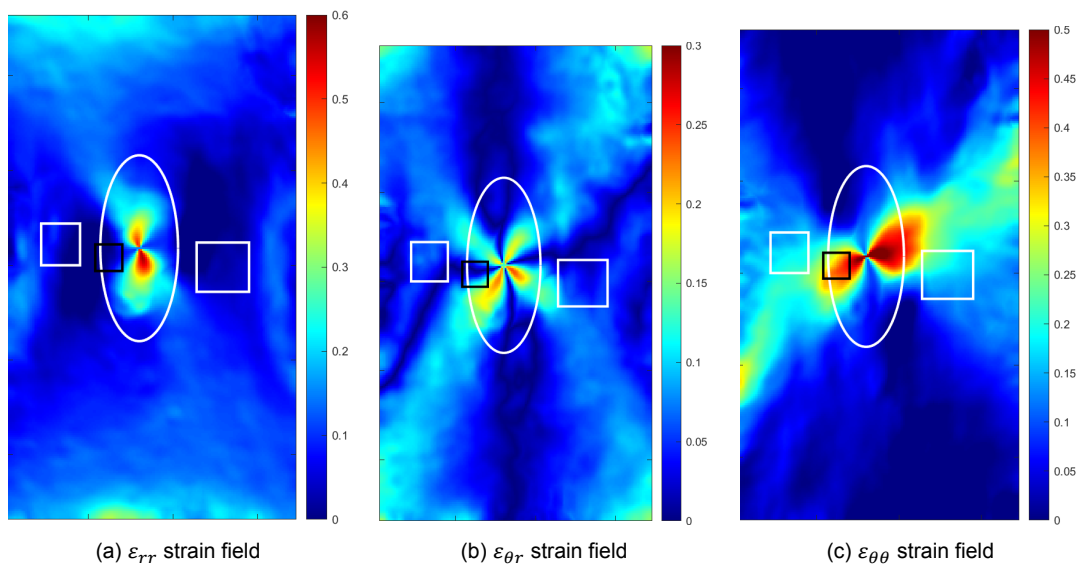


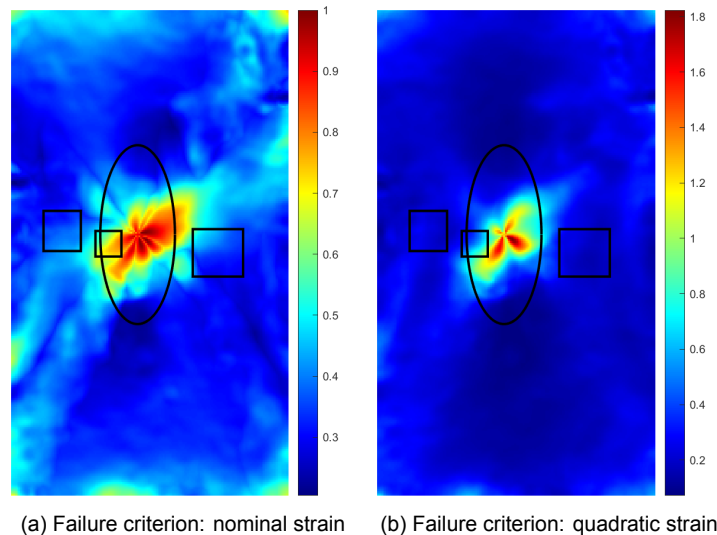
Figure I.1: Marked strain field maps before SI rupture. Rupture of the SI and fibrous tissue initiate at the black and white rectangles respectively. The shape and boundary of the SI is indicated by the white oval at the center of the images.

The ε_{rr} strain distribution has an '8'-shaped high strain region (greater than 0.3) at the centre of the SI, aligned to the y-direction. This indicates that from top to bottom, the SI experiences extension in the r-direction. The SI rupture box is nestled between the two loops, where the median strain is nearly 0. The fibrous tissue rupture boxes also enclose areas with low and negative radial strains found on the right and left of the SI. Looking at appendix E, the '8' shape can be distinguished in four of the five samples, where the rupture boxes associate with similar strain modes in the same way.

The $\varepsilon_{\theta r}$ strain distribution shows the contribution of both angular and radial strains. The SI contains a distinct 'x'-shaped region produced by intersecting high strains (greater than 0.1). The strains measured along the diagonals of the 'x' shape are consistently higher than off-diagonal strains. The SI and fibrous tissue rupture boxes lie between these diagonals, overlaying low strains (0.05 or lower). The other samples considered in this report show consistency with these observations.

The $\varepsilon_{\theta\theta}$ in the figure I.1c bears likeness to the ε_{yy} distribution. A high strain region in the shape of an '8' spans through the SI from left to right, indicating that the underlying tissue experiences the highest circular extension. This phenomenon can be related to the alignment of the circular direction with the tensile straining direction. Where the SI rupture box overlays a single loop in the high strain region, the fibrous tissue rupture boxes are situated on the edge of the region. Here they capture a transition in strain modes. The observations from other samples concur with the above description.

I.1.2. Failure criteria



High nominal strains in the polar coordinate system accumulate in the SI, producing a flower-like shape (see figure I.2a). The SI rupture box lies on the high curvature edge of the region and captures various failure values, ranging between 0.5 and 0.8. These magnitudes are notably smaller than those observed in the cartesian coordinate system. The fibrous tissue rupture boxes lie outside this region, overlying lower strains. While the 'flower'-shape pattern is only prominent in three of the five samples, the association between the rupture boxes and strain modes are alike.

The polar quadratic strain criterion presented in figure I.2b shows that its high failure values lie within the SI. This 'x'-shaped region has a magnitude larger than 1.5, while the surrounding tissue never exceeds 0.5. The SI rupture box overlays the intersection between the shape and the SI boundary, once again overlapping a gradient between high and low failure values. The fibrous tissue rupture sites lie in the sea of low strains. Here, no unique patterns suggest vulnerability. All other samples find a nearly identical situation.

I.2. Local analysis

The following section is structured to analyse the results from data segmentation and the relationship between the local maxima and the rupture site.

I.2.1. Segmentation

The segmentation of the polar ε_{rr} distribution is summarised in figure I.3a. It does not follow a regular sinusoidal pattern, as two peaks of different heights emerge from the plot, accompanied by a small elevation in strains in segment 10. The rupture segments lie in the second highest peak, with a medium strain between 0.12 and 0.18. The boxplots from other samples resemble the presented pattern, where the respective rupture segments also correspond to a peak in strains. However, as was seen in the cartesian coordinate system, the location appears insensitive to the peak width, medium strain magnitude, or other features.

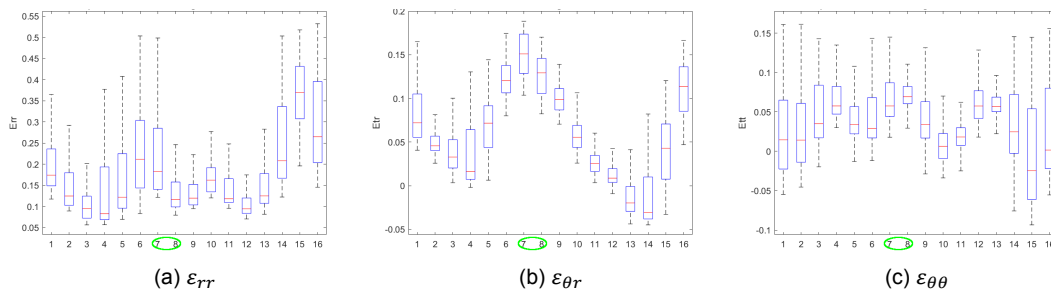


Figure I.3: Boxplots based on 16-fold segmentation

The boxplot of the $\varepsilon_{\theta r}$ segments show that the medians oscillate similar to segmented ε_{xx} strain. As is presented in figure I.3b, two peaks lie at segments 7 and 16. The ruptured segments occupy the highest peak, where the median strains lie between 0.13 and 0.15. Inspecting the strains in other samples affirms that the rupture segments consistently associate with peaks in median strain but that they are not required to occur at a global maximum.

The segmentation map of the $\varepsilon_{\theta\theta}$ strain also lacks a regular pattern. In figure I.3c, strains oscillate to form three nearly indistinguishable peaks corresponding to segments 4, 8 and 13. In this plot, rupture finds itself in the segment with the highest median strain. Comparing this to other samples reveals that rupture segments are always associated with a peak but wavers between different relative peak heights.

I.2.2. Local maxima

The maxima and minima found in the polar strain maps are described below. The figures that visualise their positions can be found in appendix E.

Inspecting the entire ROI

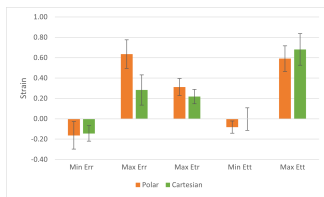
The polar maxima and minima strains reach similar or greater heights than those measured for the cartesian coordinate system. This is presented in figure I.4a. Except for the ε_{tt} maxima, the strain magnitudes for the polar strains are consistently greater. The ε_{tt} strains capture the greatest range, where strains lie between -0.16 ± 0.13 and 0.64 ± 0.14 .

Comparing the measured average distances in the polar coordinate system to those in the cartesian system shows that the polar maxima and minima collectively perform better at estimating the distance to the SI rupture box. This is evident from figure I.4b, which expresses the ultimate strains for both coordinate systems. Both the distances and the standard deviation

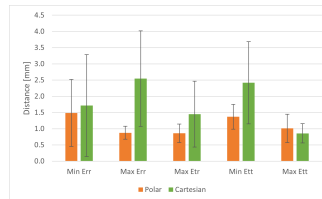
between samples are smaller for the polar strains. Together with the ε_{yy} maxima, the ε_{tr} maxima ε_{rr} maxima lie the closest to the SI rupture site.

Inspecting the SI and surrounding tissue

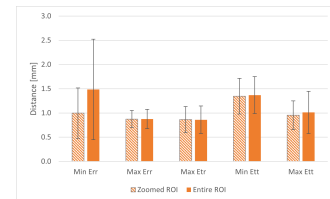
The maxima and minima in the SI and surrounding tissue reach nearly identical magnitudes as those found for the entire ROI in figure I.4a. Similarly, their standard deviations remain unchanged. Therefore, the zoomed perspective of the polar strains offers no novel observations with regard to the strain magnitudes. The average distances between both perspectives are also nearly identical. The zoomed perspective only alters the average distance to the ε_{xx} minima. This is visualised in figure I.4c.



(a) Comparing the minima and maxima found in the polar and cartesian strain maps. The error bars show the standard deviation across all samples.



(b) Comparing the distances to the polar and cartesian strain minim and maxima. The error bars indicate the standard deviation across all samples.



(c) Comparing the distances between polar strain maxima and minima to the SI rupture site for all samples. The error bars indicate the standard deviation.



Script necessities

This report established several basic scripts which accommodated for the strategies discussed in this appendix. Although the details of these scripts are not elaborated, their motivation and execution are briefly discussed. The scripts can be obtained from R.M.Hengst or H. Crielaard.

J.0.1. Elimination of boundary elements

It is noticeable that artefacts always manifest around the periphery of the ROI. This observation is especially strong at the superior and inferior edges connected to the clamps. DIC analysis can not successfully complete the calculations around these surfaces and generate artefacts.

Aberrations at the tissue periphery are undesired in strain analysis. Different offsets from the ROI edge have been considered to exclude these artefacts with a minimal loss. A threshold of 10 matrix elements most effectively excludes the pathological variation along the lateral tissue edges. The superior and inferior edges of the tissue construct are marred with artefacts of larger sizes. An exclusion border size of 20 matrix elements along the vertical edges significantly reduced the effects of these artefacts. Consequently, the boundary elements were eliminated by an asymmetric threshold (10 elements from lateral edges, 20 elements from the top and bottom edges).

J.1. Zoomed perspective of the SI

The isolation of the SI during local analysis was achieved by selecting the SI and its surrounding tissue. This report found that the ring of fibrous tissue around the SI should be 20 elements to capture the local strain regions in the SI fully. The dimension of this ring is approximately equivalent to 0.77 mm.

J.2. Structural similarity index

The structural similarity index is a mathematical approach for measuring the quality for grayscale images [69]. The closer this value is to 1, the higher the uniformity between the regions. Its computation follows the equation:

$$SSIM(x, y) = f \left([l(x, y)]^\alpha \cdot [c(x, y)]^\beta \cdot [l(x, y)]^\gamma \right) \quad (J.1)$$

where l , c and s are the luminance, contrast and structure of the image constituents. These components are relatively independent and serve to unbiased and normalise the signals from the

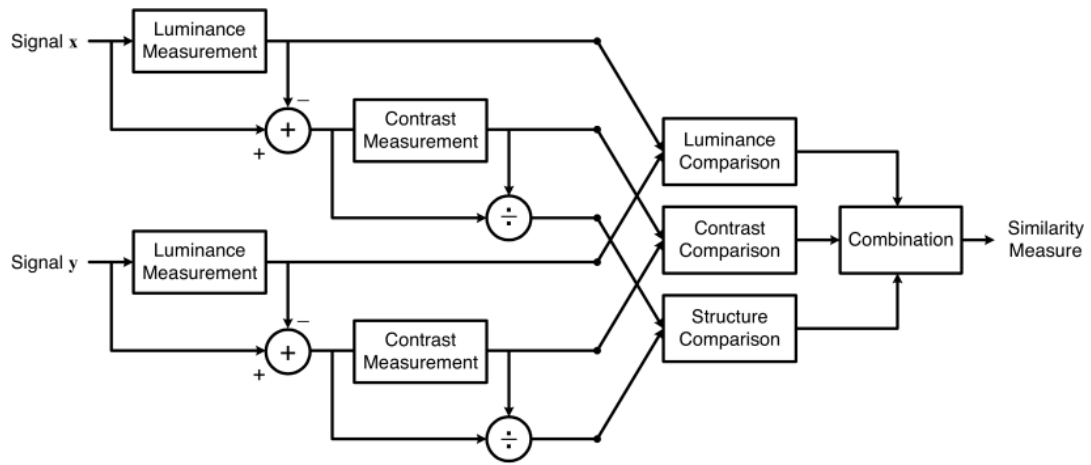


Figure J.1: Summary of SSIM measurement. Image taken from Wang, et al. [69]

images. Together they allocate a quantitative value between 0 and 1 to indicate the similarity between the images.

$$\begin{aligned}
 l(x, y) &= \frac{2\mu_x\mu_y + C_1}{\mu_x^2 + \mu_y^2 + C_1} \\
 c(x, y) &= \frac{2\sigma_x\sigma_y + C_2}{\sigma_x^2 + \sigma_y^2 + C_2} \\
 s(x, y) &= \frac{2\sigma_{xy} + C_3}{\sigma_x\sigma_y + C_3}
 \end{aligned}
 \tag{J.2}$$

Figure J.1 summarises the workings of this function

Bibliography

- [1] Jacob Fog Bentzon et al. “Mechanisms of plaque formation and rupture”. In: *Circulation research* 114.12 (2014), pp. 1852–1866.
- [2] Allen P Burke et al. “Coronary risk factors and plaque morphology in men with coronary disease who died suddenly”. In: *New England Journal of Medicine* 336.18 (1997), pp. 1276–1282.
- [3] Ramzi S. Cotran et al. “Blood vessels”. In: *Pathologic basis of disease*. Saunders Elsevier, 2015, pp. 483–522.
- [4] William Insull Jr. “The pathology of atherosclerosis: plaque development and plaque responses to medical treatment”. In: *The American journal of medicine* 122.1 (2009), S3–S14.
- [5] WHO. *The top 10 causes of death*. 2020. URL: <https://www.who.int/news-room/fact-sheets/detail/the-top-10-causes-of-death>.
- [6] EN Marieb and Katja Hoehn. “Human Anatomy & Physiology (10th, Global ed.)”. In: *Harlow: Pearson Education Limited* (2016).
- [7] Kara Rogers. *Atherosclerosis | pathology*. 2021. URL: <https://www.britannica.com/science/atherosclerosis>.
- [8] Steven Daniel Funk, Arif Yurdagul, and A Wayne Orr. “Hyperglycemia and endothelial dysfunction in atherosclerosis: lessons from type 1 diabetes”. In: *International journal of vascular medicine* 2012 (2012).
- [9] Ira Tabas, Kevin Jon Williams, and Jan Borén. “Subendothelial lipoprotein retention as the initiating process in atherosclerosis: update and therapeutic implications”. In: *Circulation* 116.16 (2007), pp. 1832–1844.
- [10] Peter D Richardson, MJ Davies, and GVR Born. “Influence of plaque configuration and stress distribution on fissuring of coronary atherosclerotic plaques”. In: *The Lancet* 334.8669 (1989), pp. 941–944.
- [11] Anusha Seneviratne et al. “Biomechanical factors and macrophages in plaque stability”. In: *Cardiovascular research* 99.2 (2013), pp. 284–293.
- [12] Osamu Kurihara et al. “Seasonal variations in the pathogenesis of acute coronary syndromes”. In: *Journal of the American Heart Association* 9.13 (2020), e015579.
- [13] Makoto Araki et al. “Circadian variations in pathogenesis of ST-segment elevation myocardial infarction: An optical coherence tomography study”. In: *Journal of Thrombosis and Thrombolysis* 51.2 (2021), pp. 379–387.
- [14] George C Cheng et al. “Distribution of circumferential stress in ruptured and stable atherosclerotic lesions. A structural analysis with histopathological correlation.” In: *Circulation* 87.4 (1993), pp. 1179–1187.

- [15] Gerhard A Holzapfel, Gerhard Sommer, and Peter Regitnig. "Anisotropic mechanical properties of tissue components in human atherosclerotic plaques". In: *J. Biomech. Eng.* 126.5 (2004), pp. 657–665.
- [16] Robert L Ohsfeldt et al. "Medical and cost burden of atherosclerosis among patients treated in routine clinical practice". In: *Journal of medical economics* 13.3 (2010), pp. 500–507.
- [17] Frank D Kolodgie et al. "The thin-cap fibroatheroma: a type of vulnerable plaque: the major precursor lesion to acute coronary syndromes". In: *Current opinion in cardiology* 16.5 (2001), pp. 285–292.
- [18] Renu Virmani et al. "Pathology of the thin-cap fibroatheroma: A type of vulnerable plaque". In: *Journal of interventional cardiology* 16.3 (2003), pp. 267–272.
- [19] Jessica N Redgrave et al. "Critical cap thickness and rupture in symptomatic carotid plaques: the oxford plaque study". In: *Stroke* 39.6 (2008), pp. 1722–1729.
- [20] Ying Wang et al. "Imaging cardiovascular calcification". In: *Journal of the American Heart Association* 7.13 (2018), e008564.
- [21] Ik-Kyung Jang et al. "In vivo characterization of coronary atherosclerotic plaque by use of optical coherence tomography". In: *Circulation* 111.12 (2005), pp. 1551–1555.
- [22] Sunny Goel et al. "Imaging modalities to identify inflammation in an atherosclerotic plaque". In: *Radiology research and practice* 2015 (2015).
- [23] Johannes A Schaar et al. "Characterizing vulnerable plaque features with intravascular elastography". In: *Circulation* 108.21 (2003), pp. 2636–2641.
- [24] Michelle C Williams et al. "Coronary artery plaque characteristics associated with adverse outcomes in the SCOT-HEART study". In: *Journal of the American College of Cardiology* 73.3 (2019), pp. 291–301.
- [25] SCOT-Heart Investigators. "Coronary CT angiography and 5-year risk of myocardial infarction". In: *New England Journal of Medicine* 379.10 (2018), pp. 924–933.
- [26] Gregg W Stone et al. "A prospective natural-history study of coronary atherosclerosis". In: *New England journal of medicine* 364.3 (2011), pp. 226–235.
- [27] Pavan K Cheruvu et al. "Frequency and distribution of thin-cap fibroatheroma and ruptured plaques in human coronary arteries: a pathologic study". In: *Journal of the American College of Cardiology* 50.10 (2007), pp. 940–949.
- [28] Gérard Finet, Jacques Ohayon, and Gilles Rioufol. "Biomechanical interaction between cap thickness, lipid core composition and blood pressure in vulnerable coronary plaque: impact on stability or instability". In: *Coronary artery disease* 15.1 (2004), pp. 13–20.
- [29] Renu Virmani et al. "Lessons from sudden coronary death: a comprehensive morphological classification scheme for atherosclerotic lesions". In: *Arteriosclerosis, thrombosis, and vascular biology* 20.5 (2000), pp. 1262–1275.

- [30] Saeko Takahashi et al. "The effect of statins on high-risk atherosclerotic plaque associated with low endothelial shear stress". In: *Current opinion in lipidology* 22.5 (2011), pp. 358–364.
- [31] Ward Casscells, Morteza Naghavi, and James T Willerson. "Vulnerable atherosclerotic plaque: a multifocal disease". In: *Circulation* 107.16 (2003), pp. 2072–2075.
- [32] Natalia Maldonado et al. "A mechanistic analysis of the role of microcalcifications in atherosclerotic plaque stability: potential implications for plaque rupture". In: *American Journal of Physiology-Heart and Circulatory Physiology* 303.5 (2012), H619–H628.
- [33] Joshua D Hutcheson, Natalia Maldonado, and Elena Aikawa. "Small entities with large impact: microcalcifications and atherosclerotic plaque vulnerability". In: *Current opinion in lipidology* 25.5 (2014), p. 327.
- [34] Luis Cardoso et al. "Effect of tissue properties, shape and orientation of microcalcifications on vulnerable cap stability using different hyperelastic constitutive models". In: *Journal of biomechanics* 47.4 (2014), pp. 870–877.
- [35] Yuliya Vengrenyuk et al. "A hypothesis for vulnerable plaque rupture due to stress-induced debonding around cellular microcalcifications in thin fibrous caps". In: *Proceedings of the National Academy of Sciences* 103.40 (2006), pp. 14678–14683.
- [36] Yuanming Luo et al. "Characteristics of thoracic aortic aneurysm rupture in vitro". In: *Acta biomaterialia* 42 (2016), pp. 286–295.
- [37] KY Volokh. "Modeling failure of soft anisotropic materials with application to arteries". In: *Journal of the Mechanical Behavior of Biomedical Materials* 4.8 (2011), pp. 1582–1594.
- [38] CJ Cyron and JD Humphrey. "Growth and remodeling of load-bearing biological soft tissues". In: *Meccanica* 52.3 (2017), pp. 645–664.
- [39] Chris L de Korte et al. "Identification of atherosclerotic plaque components with intravascular ultrasound elastography in vivo: a Yucatan pig study". In: *Circulation* 105.14 (2002), pp. 1627–1630.
- [40] Mathias Kaspar et al. "Non-invasive ultrasound-based imaging of atherosclerosis". In: *Vasa* (2018).
- [41] Surya C Gnyawali et al. "High-resolution harmonics ultrasound imaging for non-invasive characterization of wound healing in a pre-clinical swine model". In: *PloS one* 10.3 (2015), e0122327.
- [42] Tamar B Wissing et al. "Tissue-engineered collagenous fibrous cap models to systematically elucidate atherosclerotic plaque rupture." In: *bioRxiv* (2021).
- [43] Ali C Akyildiz, Lambert Speelman, and Frank JH Gijzen. "Mechanical properties of human atherosclerotic intima tissue". In: *Journal of biomechanics* 47.4 (2014), pp. 773–783.
- [44] Sheila Serra. "Mechanical Characterization of Tissue Engineered Fibrous Cap Constructs". MA thesis. the Netherlands: Delft University of Technology, 2020.

- [45] Mirjam P Rubbens et al. "Intermittent straining accelerates the development of tissue properties in engineered heart valve tissue". In: *Tissue Engineering Part A* 15.5 (2009), pp. 999–1008.
- [46] Mirjam P Rubbens et al. "Straining Mode–Dependent Collagen Remodeling in Engineered Cardiovascular Tissue". In: *Tissue Engineering Part A* 15.4 (2009), pp. 841–849.
- [47] Ali C Akyildiz et al. "3D fiber orientation in atherosclerotic carotid plaques". In: *Journal of structural biology* 200.1 (2017), pp. 28–35.
- [48] Robert D Johnston, Robert T Gaul, and Caitriona Lally. "An investigation into the critical role of fibre orientation in the ultimate tensile strength and stiffness of human carotid plaque caps". In: *Acta Biomaterialia* 124 (2021), pp. 291–300.
- [49] Jason Lee et al. "A novel system for studying mechanical strain waveform-dependent responses in vascular smooth muscle cells". In: *Lab on a chip* 13.23 (2013), pp. 4573–4582.
- [50] MT Walsh et al. "Uniaxial tensile testing approaches for characterisation of atherosclerotic plaques". In: *Journal of biomechanics* 47.4 (2014), pp. 793–804.
- [51] Hector M García-García et al. "IVUS-based imaging modalities for tissue characterization: similarities and differences". In: *The international journal of cardiovascular imaging* 27.2 (2011), pp. 215–224.
- [52] Bob McGinty. *Strain*. 2021. URL: <http://www.continuummechanics.org/strain.html>.
- [53] Gerhard A Holzapfel, Thomas C Gasser, and Ray W Ogden. "A new constitutive framework for arterial wall mechanics and a comparative study of material models". In: *Journal of elasticity and the physical science of solids* 61.1 (2000), pp. 1–48.
- [54] Gerhard A Holzapfel et al. "Computational approaches for analyzing the mechanics of atherosclerotic plaques: a review". In: *Journal of biomechanics* 47.4 (2014), pp. 859–869.
- [55] Chao Sang et al. "A uniaxial testing approach for consistent failure in vascular tissues". In: *Journal of biomechanical engineering* 140.6 (2018), p. 061010.
- [56] Graeham R Douglas et al. "Impact of fiber structure on the material stability and rupture mechanisms of coronary atherosclerotic plaques". In: *Annals of biomedical engineering* 45.6 (2017), pp. 1462–1474.
- [57] Maarten J Swaab. "Modeling Atherosclerotic Plaque Fracture using Tendon Rupture Models". MA thesis. the Netherlands: Delft University of Technology, 2021.
- [58] Howard M Loree et al. "Static circumferential tangential modulus of human atherosclerotic tissue". In: *Journal of biomechanics* 27.2 (1994), pp. 195–204.
- [59] Jacques Ohayon et al. "Biomechanics of atherosclerotic coronary plaque: site, stability and in vivo elasticity modeling". In: *Annals of biomedical engineering* 42.2 (2014), pp. 269–279.
- [60] Peter Libby et al. "Collagenases and cracks in the plaque". In: *The Journal of clinical investigation* 123.8 (2013), pp. 3201–3203.

- [61] Jin-Hwan Kim et al. "Experimental characterization of rupture in human aortic aneurysms using a full-field measurement technique". In: *Biomechanics and modeling in mechanobiology* 11.6 (2012), pp. 841–853.
- [62] Johannes A Schaar et al. "Intravascular palpography for vulnerable plaque assessment". In: *Journal of the American College of Cardiology* 47.8S (2006), pp. C86–C91.
- [63] Lysle H Peterson, Roderick E Jensen, and John Parnell. "Mechanical properties of arteries in vivo". In: *Circulation Research* 8.3 (1960), pp. 622–639.
- [64] Hiroko Iino et al. "Usefulness of carotid arterial strain values for evaluating the arteriosclerosis". In: *Journal of atherosclerosis and thrombosis* 26.5 (2019), pp. 476–487.
- [65] J Blaber, B Adair, and A Antoniou. "Ncorr: open-source 2D digital image correlation matlab software". In: *Experimental Mechanics* 55.6 (2015), pp. 1105–1122.
- [66] David Lecompte et al. "Quality assessment of speckle patterns for digital image correlation". In: *Optics and lasers in Engineering* 44.11 (2006), pp. 1132–1145.
- [67] Bing Pan. "Reliability-guided digital image correlation for image deformation measurement". In: *Applied optics* 48.8 (2009), pp. 1535–1542.
- [68] Will LePage. *A practical guide to DIC*. URL: digitalimagecorrelation.org.
- [69] Zhou Wang et al. "Image quality assessment: from error visibility to structural similarity". In: *IEEE transactions on image processing* 13.4 (2004), pp. 600–612.